Democratic and Popular Republic of Algeria

العلمي والبحث العالي وزارة التعليم

Ministry of Higher Education and Scientific Research

University of Mohamed
Khider – Biskra
Faculty of Exact Sciences
and Science of Nature and life.
Materials Science Department

جامعة محمد خيضر - بسكرة
كلية العلوم الدقيقة و علوم الطبيعة
و الحياة
قسم علوم المادة

Thesis presented to obtain the degree:

Doctorat LMD

Option**:**

Physics

Entitled:

Multi-thin layers as electrodes for organic solar cell: Elaboration and numerical modeling.

Presented by:

Maroua ABDALLAOUI

In front of the jury composed of:

Meftah Afak	Professor	U.M.K. Biskra	President
Nouredine Sengouga	Professor	U.M.K. Biskra	Supervisor
Abdelouahed Chala	Professor	Khenchela University	Co-Supervisor
Meftah Amjad	Professor	U.M.K. Biskra	Examiner
Baaziz Hakim	Professor	U.M.B. M'sila	Examiner

Acknowledgements

Thank first and foremost to God; without his grace this thesis would never have been finished on time.

I would like to express my sincere gratitude to my supervisor **Prof. SENGOUGA Noureddine** for the continuous support of my research, for his patience, motivation, enthusiasm, and immense knowledge. His guidance helped me in all the time of research and writing of this dissertation. I could not have imagined having a better advisor and mentor for my Doctorate study.

Besides my advisor, I would like to thank my Co-Supervisor **Prof. ABDELOUAHED Chala** and the rest of my dissertation jury: **Prof. MEFTAH Afak, Prof. MEFTAH Amjad and Prof BAAZIZ Hakim** for their comments and their questions.

Of course, I do not forget my honorable teacher **Prof. MEFTAH Afak** for her help and guidance during my work, without her I could not continue and succeed.

Last but not the least, I would like to thank my family: **my parents, my siblings** for supporting me spiritually throughout my life.

Special thanks to **my husband** and **my little daughter.**

الملخص

في هذا العمل، تمت دراسة وتحسين الخلايا الشمسية العضوية العادية والعكسية (OSC و IOSC) باستخدام برنامج GPVDM. تتكون الخليتان الأوليتان اللتان تمت دراستهما (OSC و IOSC) من طبقة ضوئية نشطة (PAL) وطبقة نقل الإلكترونات (ETL) وطبقة نقل الثقوب (HTL). كانت PAL عبارة عن مزيج من poly (3-hexylthiophene) (P3HT) و [6,6]-phenyl C61-butyric acid methylester (PCBM) شبه موصل عضوي (P3HT: PCBM). كان ETL الأولي هو أكسيد التيتانيوم (TiO_x) بينما كان ETL عبارة عن polystyrene (3,4-ethylenedioxythiophene) sulfonate (PEDOT: PSS) بسمك 50 nm في OSC و IOSC. تم دراسة تأثير سماكة الطبقة الفعالة بشكل منهجي ثم تم دراسة تأثير سمك ETL و HTL بعدها تم اقتراح مجموعة من المواد المرشحة كـ ETL و HTL. وجد أن أفضل ETL و HTL هما TiO_x و Cu_2O على التوالي للخلية العادية بينما كانا PEDOT: PSS و ZnO للخلية العكسية. كانت الكفاءة المُحسَّنة للخلايا العادية والعكسية 4.77٪ و 5.35٪ لكل من Al/ TiO_x (50 nm)/ P3HT:PCBM (150 nm)/ Cu_2O /(10 nm)/ITO و ITO/ ZnO (30nm)/ P3HT:PCBM (200 nm)/ PEDOT:PSS (20 nm)/ Ag للخلايا العادية والعكسية. تم أيضًا اقتراح أقطاب كهربائية متعددة الطبقات من النموذج TCO / Ag / TCO وتحسينها ضمن GPVDM. وجد أن AZO (40 nm) / Ag (6 nm) / AZO (40 nm) هو أفضل بديل لـ ITO مع تحسين الكفاءة إلى 4.96٪ و 5.29٪ للخلايا العادية والعكسية على التوالي.

تم إجراء نفس الدراسة باستخدام برنامج SILVACO ATLAS. أظهرت النتائج أن أفضل كفاءة للخلية العادية بلغت 4.73٪ للبنية Al / ZnO (Al / ZnO (10 nm) / P3HT:PCBM (100 nm) / PEDOT:PSS (10 nm) / ITO لـ OSC ، بينما وصلت 4.77٪ للخلية الشمسية العكسية ذات البنية Ag/ NiO (10 nm)/ P3HT:PCBM (300 nm)/ TiO_2 /(60nm)/ITO

تم أيضًا دراسة وتحسين القطب الكهربائي متعدد الطبقات TCO / Ag / TCO باستخدام برنامج MATLAB المطور، حيث وجد أن نفاذية جميع الأقطاب الكهربائية المدروسة تجاوزت 97 ٪ ، وهو أفضل مما تم الحصول عليه لـ ITO. عندما تم تطبيق الأقطاب الكهربائية المطورة في الخليتين الشمسيتين العضويتين المحسنتين، وجد أن النتائج قد تحسنت، ووصل أفضل أداء إلى 4.78٪ و4.97٪ لـ OSC وIOSC على التوالي. كان القطب متعدد الطبقات المحسن هو MoO_3(50nm)/Ag(7nm)/MoO_3(50nm).

كما هو متوقع النتائج متقاربة، لكنها ليست متطابقة تمامًا، ويعود هذا الاختلاف إلى طبيعة البرنامج، والمعادلات الفيزيائية المطبقة، والمعلمات المستخدمة.

الكلمات المفتاحية: الخلايا الشمسية العضوية، محاكاة رقمية، الخاصية J-V، GPVDM، Matlab، SILVACO-ATLAS

Abstract

In this work, the conventional and inverse organic solar cells (OSC and IOSC) were studied and improved using the GPVDM software. The initial studied two cells (OSC and IOSC) consist a of photoactive layer (PAL), an electron transporting layer (ETL) and a hole transporting layer (HTL). The PAL was a blend of the poly(3-hexylthiophene) (P3HT) and [6,6]-phenyl C61-butyric acid methylester (PCBM) organic semiconductor (P3HT:PCBM). The initial ETL was Tittanium Oxide (TiO_x) while the ETL was a poly(3,4-ethylenedioxythiophene) polystyrene sulfonate (PEDOT:PSS) with a thickness of 50 nm in OSC and IOSC. The effect of the active layer thickness was systematically investigated, then the ETL and HTL thicknesses effect were studied. Also, a group of candidate materials were proposed as ETL and HTL. It was found that the best ETL and HTL were TiO_x and Cu_2O respectively for the conventional cell while they were PEDOT:PSS and ZnO for the inverse cell. The optimised efficiency for normal and reverse cells were 4.77% and 5.35% for both Al/ TiO_x (50 nm)/ P3HT:PCBM (150 nm)/ Cu_2O (10 nm)/ITO and Ag/ PEDOT:PSS (20 nm)/ P3HT:PCBM (200 nm)/ ZnO (30nm)/ ITO for normal and reverse cells. Multilayer electrodes of the form TCO / Ag / TCO were also proposed and improved within GPVDM. It was found that AZO (40 nm) / Ag (6 nm) / AZO (40 nm) is the best alternative to ITO with efficiencies improved to 4.96% and 5.29% for the normal and inverse cells respectively.

The same study was carried out using the SILVACO ATLAS software. The results showed that the best efficiency for the normal cell reached 4.73% for the structure Al / ZnO (10 nm) / P3HT:PCBM (100 nm) / PEDOT:PSS (10 nm) / ITO OSC, while it reached 4.77% for an Ag/ NiO (10 nm)/ P3HT:PCBM (300 nm)/ TiO_2 (60nm)/ITO IOSC.

The TCO/Ag/TCO multilayer electrode was also studied and improved using a developed MATLAB program, where it was found that the transmittances of all studied electrodes exceeded 97%, which is better than what is obtained for ITO. When the developed electrodes applied in the two improved organic solar cells, it was found that the results were improved, and the best performances reached 4.78% and 4.91% for OSC and IOSC, respectively. The optimized multi-layer electrode was MoO_3(50nm)/Ag(7nm)/MoO_3(50nm).

As expected, the results are close, but not completely identical, and this difference is due to the nature of the program, the applied physical equations, and the parameters used.

Key words: Organic solar cells, numerical simulation, J-V characteristic, GPVDM, Matlab and SILVACO-ATLAS.

TABLE OF CONTENTS

LIST OF TABLES

LIST OF FIGURES

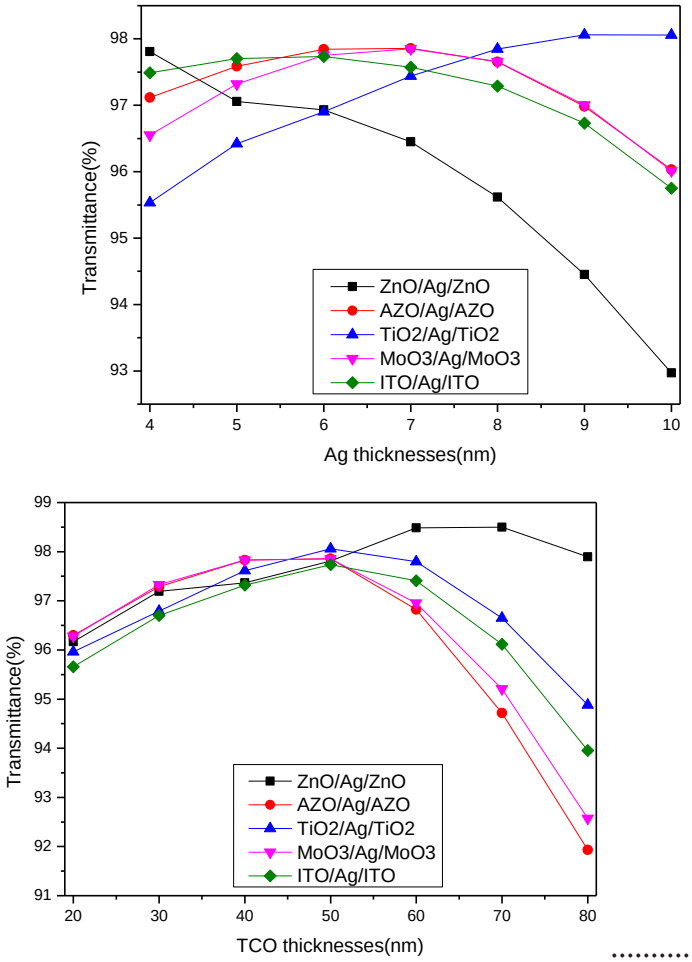

GENERAL

INTRODUCTION

General Introduction

The need for energy is increasing rapidly in the coming years due to expanding populations and economies. Radical adjustments in our global energy production and consumption habits are required due to the threat of global warming and the decreasing availability of fossil fuels. One of the key issues facing the twenty-first century is the primary supply of environmentally friendly and sustainable energy[1].

Photovoltaic (PV) technology was initiated so that people might benefit from unlimited sun energy. Inorganic photovoltaics (IPVs) are currently used extensively because of their high-power conversion efficiencies (PCEs) and remarkable stability. However, the pollution produced during the production procedures puts a limit on IPVs. Consequently, IPVs cannot be regarded as green energy sources. As an alternative to IPVs, organic PVs (OPVs) have less waste/pollution generation during device construction, making them one of the green energy sources. To increase the PCEs of OPVs, scientists and engineers have deployed great ressources over the past two decades to discover novel materials, construct new architectures, alter thin film morphology, and improve interfacial engineering. Single junction bulk heterojunction (BHJ) OPVs have achieved over 10% PCE, and triple junction BHJ OPVs have observed over 12% PCE (three single OPVs stacked together). Therefore, advancements in photovoltaic technology are now required to increase the efficiency and cost-effectiveness of solar energy harvesting[1, 2].

Effective solar spectrum absorption is required for optimal device performance. However, the short diffusion length of excitons limits the usage of thick organic absorbent films. Making very transparent electrodes that permit high absorption through adsorbing layer is one potential solution. The most popular transparent anode for organic devices is indium tin oxide (ITO), which has a very low sheet resistance (10 Ω/sq.) and a high optical transmittance (> 80%)[3, 4]. ITO, however, also has several drawbacks, such as:

- The long-term performance of OPVs is negatively influenced by the diffusion nature of indium ions formed by the indium etching within the ITO films, which is provided by the acidity of the organic material[5].
- There are also concerns about the cost, scarcity and toxicity of indium[6].

- ITO is also of a limited mechanical flexibility to be utilized in flexible electronics and therefore can create defects if it is too flexed [7].
- One of the main reasons of the efficiency drop is related to the high sheet resistivity of the Indium Tin Oxide (ITO) transparent electrode at large scale (Pandey and Nunzi, 2011)[8].
- Such polymer substrates cannot tolerate the high temperatures that are commonly used in the deposition of highly conductive ITO[6].
- The brittle nature of ITO films have limited its use in high-performance flexible electronic devices because cracks can form during bending, increasing the electrical resistance and, ultimately, lowering the device's performance. Furthermore, many plastic substrates with low melting temperatures are unfavourable because low sheet resistance ITO film demands high processing temperatures (> 300 °C). Even though there has been a lot of study done on transparent electrodes made of silver, carbon, and metal networks, they have been unable to overcome problems with low processing temperatures, uniform sheet resistance, high transmittance, and mass production[3].
- The production of ITO require complex sputtering and high temperature, this process are not compatible with organic material since it is an aggressive technique for deposition of organic materials[9, 10].
- Doped transparent conducting oxide thin films are typically between 150 and 700 nm thick, and when the thickness is reduced, the resistance increases significantly, making it impossible to employ as transparent electrodes for specialised optoelectronic devices[8, 11].

These drawbacks are particularly important because nowadays the demand for flexible electronics is growing fast. Therefore, alternative transparent conductive electrodes (TCEs) are required.

High optical transmittance in the visible spectrum, high conductivity, ease of managing its surface work function, and flexibility are requirements that the new TCE must fulfil. Additionally, its components must to be abundant, neutral, and environmentally friendly. The electrode's characteristics should remain stable in a room-temperature environment. To be applied in an industrial setting, the process employed for its deposition must be as soft as possible, performed at room temperature, and produce repeatable results. This new TCE must be suitable with plastic

substrate in terms of flexibility and adherence. It should have a smooth surface. To replace ITO, other alternative TCEs have been developed[12].

Here, possible alternatives include of PEDOT:PSS in combination with metal grids, transparent conductive oxides like Al-doped ZnO (AZO) or Ga-doped ZnO (GZO), graphene, carbon nanotubes, silver nanowires and oxide/metal/oxide stacks[6, 13, 14]. Although the PEDOT:PSS electrode may be made using a simple solution technique, its conductivity still has to be enhanced and stability has to be addressed[9, 14]. AZO or GZO are less inexpensive than ITO, but they are also less desired due to their similar brittleness and high-temperature sputtering technique, for Ag nanowire, graphene, and carbon nanotube electrodes, the relatively high surface roughness hinders the carrier transport in devices, additionally, the complicated process required to produce these film electrodes makes them unsuitable for OSC production in a wide scale. In contrast, thermal evaporation makes it simple to create a metal thin film (for instance, Ag). Metal thin film electrodes are also promising for application in roll-to-roll mass production of OSCs due to their low visible spectrum absorption, strong conductivity, smooth surface, and ductile nature. As a result, transparent metal electrodes are the subject of an increasing number of publications[14].

A typical TCE has a three-layer structure with similar top and bottom transparent metal oxide (TMO) layers and a middle metal layer[15]. In such oxide/metal/oxide multilayer (OMO) electrodes, the first oxide layer serves as a "seed layer" for the subsequent formation of an ultrathin metal film. The second oxide layer facilitates charge extraction or charge-blocking from the device when employed in an OPV, and the metal film provides strong lateral conductivity, ensuring a suitably low series resistance. Such oxide layers maximise optical transmittance while minimising reflection from the metal film in addition to their electrical functionality [6]. TCO/metal/TCO hence demonstrates high transmittance, great flexibility, and low sheet resistance. These benefits enable OMO multilayers to have a greater figure of merit than a conventional single-layer TCO film[16].The TCO/metal/TCO structures not only accomplish higher electrical performance, but also other properties (morphology, work function, bending endurance, and corrosion resistance) that can be adapted for each specific application in an easier way than can be accomplished for single-layer TCO electrodes[16].

The key element of the TCO/metal/TCO configurations is the metal layer, which has great electrical properties and can be manufactured thin enough to offer adequate transmittance, but the

global transmittance of the stack is still raised by embedding the metal between thin TCO films which minimize the reflection from the metal layer in the visible region and generate a selective transparent effect[16, 17].Researchers have employed intermediate metallic layers such as Ag, Au, Cu, and Al. Ag has been found to be the ideal choice for this application due to its lowest absorption coefficient and lowest refractive index (n ~ 0.05-2.90) in the visible region of the solar spectrum[3, 15]. ZnO/Ag/ZnO[18], Al:ZnO/Ag/Al:ZnO[18], TiO_2/Ag/TiO_2[4], WO_3/Ag/WO_3[19], MoO_3/Ag/MoO_3[10] and IZOAg/IZO [17], are just a few examples of TCO/metal/TCO and can be deposited by various techniques including: thermal evaporation, chemical vapor deposition, spray pyrolysis, sol–gel process, and sputtering [4]. With TCO/metal/TCO systems, it is therefore simpler to replace ITO with different transparent electrode because the metal interlayer enables the total resistivity reduction even when the TCO electrical quality is low[16].

One of the goals of this dissertation is to find an alternative to ITO single layer electrode by studying the ITO-free multilayer electrodes to use in OSCs. The other objectives are to compare different structures of organic solar cells.

This thesis is divided into four main chapters in addition to general introduction and conclusion: In the first chapter an overview of organic solar cells is presented. The second chapter deals with the properties of TCO/metal/TCO multilayers transparent electrode and its applications in OPVs. The third chapter is the numerical simulation using GPVDM and SILVACO ATLAS to optimize the performance of organic solar cells. Furthermore, an analytical approach is adopted to study the multilayer electrode using MATLAB. Finally, the fourth chapter details the results obtained and their discussion.

CHAPTER I:

ORGANIC SOLAR CELLS: STRUCTURES, WORKING PRINCIPLES AND PROPERTIES.

I.1. Introduction

New green energy sources have gained widespread acceptance in recent decades as essential to sustainable development. The use of solar energy has been regarded as an alternative energy source. With tremendous effort, photovoltaic (PV) technology has advanced for many years. Different photovoltaic technologies exist for converting photons into electrons include, for instance, Dye-sensitized solar cells (DSSCs), organic solar cells (OSC), quantum dot solar cells (QDSCs) and perovskite solar cells (PSCs). High efficiency, short energy payback, and cost-effective performance are the current research hot topics. OSC is the present focus of our research, due to their low-cost processing, special material features and simple fabrication processes [20].

I.2. An overview of Organic Solar Cells (OSCs)

I.2.1. Structure types of organic solar cells

As it is known, the design of the device architecture can dramatically affect the efficiency of harvesting solar light. For example, the variation of the structure from a single light absorber sandwiched between electrodes to a bilayer donor/acceptor organic heterojunction between two electrodes can dramatically increase the cell efficiency value from around 0.1 % to over 1 %. Nowadays, cell efficiency can reach over 10 % by blending donor and acceptor materials to form a bulk heterojunction structure and accumulating the device to achieve a tandem design. The different device structures are summarised in the following section [21].

I.2.1.1. Single layer solar cells

Single layer solar cells (Figure I.1) are the first generation of the simplest design for organic solar cells. It has only one active layer made by single component organic materials (only p-type or n-type), between electrodes, typically an anode with high work function, usually a layer of

indium tin oxide (ITO), while the cathode is a layer of low work function metal such as Al, Mg or Ca [22, 23].

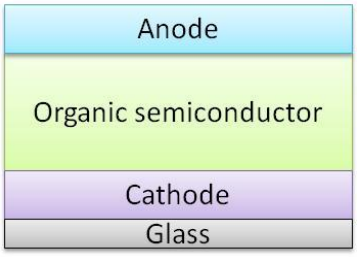

Figure I.1: Single layer OSC structure.

This structure has an intrinsic limitation in fulfilling high efficiency because the organic layer cannot correctly generate individual charges (holes and electrons) because of the great low charge separation yield created from the tightly-bound excitons in organic semiconductors. For this type, Kippelen B et al., reported single-layer OSCs with efficiencies up to $5.9 \pm 0.2\%$ [24].

I.2.1.2. Planar bilayer solar cells

In bilayer OSCs (Figure I.2), photoactive layers containing donor and acceptor organic materials absorb sunlight and generate photocurrents. The donor material (organic p-type material) is usually electron-rich molecules, which are capable of donating electrons and creating holes whereas the acceptor material (organic n-type material) should have the capacity to accept electrons (Figure I.3), with a hole transport layer (HTL) and an electron transport layer (ETL) are used to modify the work function of the electrodes to form an ohmic contact [25].

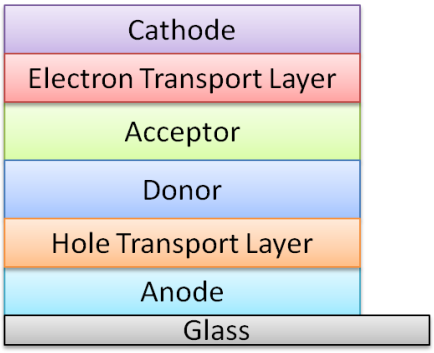

Figure I.2: Bilayer OSC structure.

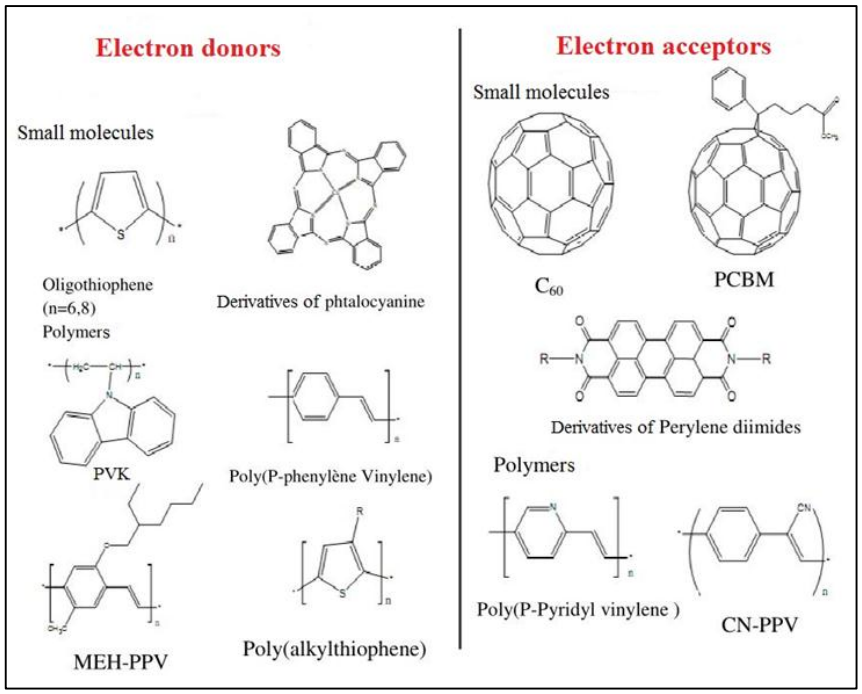

Figure I.3: Organic electron donors and acceptors .

One major drawback of this structure is the decay or recombination of excitons before they dissociate into free electrons and holes because the distance that the photogenerated excitons can be harnessed is on the order of exciton diffusion length from the donor/acceptor interface. As a result, wasting a large amount of absorbed photons, which lowers photovoltaic efficiency. Another

limitation of this construction is that the interfacial area between donors and acceptors is not large enough [26].

I.2.1.3. Bulk Heterojunction solar cell

To remove the drawback of planar bilayer cells, a bulk heterojunction (BHJ) structure was developed by blending together the donor and acceptor randomly and contacting the two electrodes simultaneously (Figure I.4), in order to reduce the distance that exciton must travel to reach a donor/acceptor interface. This structure is named bulk heterojunction because the heterojunction is dispersed throughout the bulk, whilst the donor and acceptor phases are completely separated from each other in the planar bilayer structure [21].

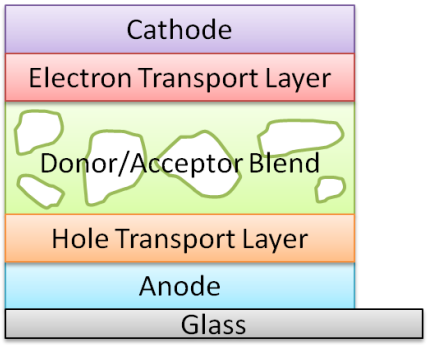

Figure I.4: Bulk heterojunction (BHJ) solar cell structure.

To avoid the unfavourable contact between organic materials and electrode (e.g., donor contacts with cathode or acceptor with anode) and unfavourable charge collection, interfacial layers such as electron transport layer (ETL) and hole transport layer (HTL) are inserted between the active layer and electrodes. In addition, electrodes with different work functions were used to create a local field to help the movement of the charges [21].

The formation of percolated pathways are required in order to transport holes and electrons to the corresponding electrodes. Otherwise, the charge trapping islands or cul-de-sacs can form during the thermodynamic phase separation and decrease the device efficiency. Therefore, the morphology of the active layer film is very critical to achieve high performance solar cells [21].

I.2.1.4. Tandem Solar cells

Another way to increase the overall absorption and efficiency of an organic solar cell is the use of Tandem structure, as shown in Figure I.5. A typical organic tandem solar cell is composed of two different cells stacked on top of each other. The sunlight that is not absorbed in the bottom cell can further infringe upon the top cell. The two cells are connected by an intermediate layer like a thin layer of Au or Ag, allowing the recombination of the holes coming from one cell with electrons coming from the other [21, 25, 27].

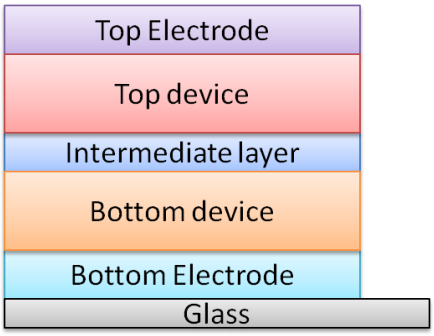

Figure I.5: Organic tandem solar cell.

I.2.2. Basics of bulk heterojunction solar cells

For inorganic photovoltaic devices, free charge carriers are produced after light absorption, while an exciton (electron–hole pair bound together electrostatically) is generated after absorbing a photon in OPVs.

The processes occurring at a donor/ acceptor heterojunction is concluded in the following five steps:

(1) Exciton generation by Photon absorption

(2) Exciton diffusion to the donor/ acceptor interface,

(3) Exciton dissociation at the interface,

(4) Carrier transport towards the electrodes,

(5) Carrier collection.

These five steps are illustrated in Figure I.6 [25, 28].

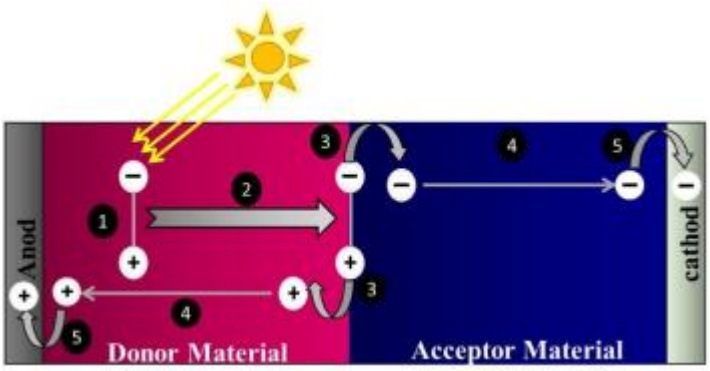

Figure I.6: The operating principle of organic solar cells.

I.2.2.1. Light absorption and exciton generation

Upon the absorption of a photon, excitation of an electron in the organic semiconductor occurs from the HOMO level to the LUMO level as shown in Figure I.6 (step 1), this is analogous to exciting an electron from the valence band to the conduction band of inorganic semiconductors.

As a result, an electron-hole pair (exciton) with binding energy typically in the range of $0.1-1.4\ eV$ is generated. The excitons then migrate to the donor-acceptor interface [29].

Light is usually absorbed by donor part of the BHJ photoactive layer. Due to high absorption coefficient of conjugated polymers ($10^7 m^{-1}$), they can effectively absorb light at maximum of their absorption spectrum with very low thickness of the photoactive layer (usually up to $100\ nm$) as compared to their inorganic silicon (an indirect semiconductor) based counterparts where thicknesses of hundreds of micrometres are required [29].

Interestingly, the absorption of light can be enhanced by lowering the band gap of donor polymers. For instance, a material with a band gap lower than $2\ eV$ is considered as a low band gap material that leads to the possibilities of improving the efficiency of OSCs due to a better overlap with the solar spectrum. For example, a band gap of $1.1\ eV$ can cover 77% of the $AM1.5$ solar photon flux as compared to the band gap of $1.9\ eV$ that can hardly cover 30% of the $AM1.5$ photon flux. Thus, a low band gap material can significantly improve the photocurrent generation [29].

I.2.2.2. Exciton diffusion

The second step involves the diffusion of the generated excitons through the active layer towards the interface between the two semiconductors (figure I.6, step 2) which works as a dissociation site. The exciton created diffuses in the material, to be able to then lead to the generation of electricity, this exciton will have to dissociate at the interface between the donor material and the acceptor material. Otherwise, it will de-energize radiatively or non-radiatively. The lifetime of an exciton is limited and varies from material to material. Its diffusion length varies from 5 to 20 nm depending on the nature of the material and the presence or not of traps in the material [30, 31].

I.2.2.3. Exciton dissociation

In organic semiconductors, photogenerated holes and electrons at the donor/acceptor interface suffer from a strong Coulomb binding energy, these Coulomb bound electron–hole pairs have to be dissociated to get free charge carriers. The difference in HOMO and LUMO between donor and acceptor layers creates electrostatic forces at the interface. When materials choice is proper, such differences generate an electric field that leads to the efficient break-up of excitons into electrons and holes (Figure I.6, step 3). Further, the free electrons are then accepted by the material with higher LUMO level and holes by the material with lower HOMO. Unfortunately, these free charge carriers can lead to recombination or trapping in a disordered interpenetrating organic material while traveling towards the electrodes [29].

I.2.2.4. Free charge carriers transport

After the exciton dissociation into free charge carriers, the charges should be transported towards the respective electrodes as shown in Figure I.6 (step 4). An internal electric field drives transportation of free charge carriers towards their respective electrodes due to the Fermi level difference of the electrodes. In general, a high work function (WF) anode and a low WF cathode create an internal electric field that determines the open circuit voltage (V_{oc}) of the cell [29].

I.2.2.5. Collection of the charge carriers at the electrodes

Photogenerated charge carriers that do not recombine are finally extracted from the photoactive layer to the respective electrodes (Figure I.6, step 5). The potential barrier at the photoactive layer/electrodes interface must be reduced to maximize the extraction of charges. Therefore, the WF of the anode should match with the HOMO of the donor material, while the WF of the cathode must match with the LUMO of the acceptor material. If the WFs match well as described, then the contacts are said to be Ohmic contacts. Contrary to this, if there is a mismatch between the anode and cathode with that of donor HOMO or acceptor LUMO, respectively, then

no Ohmic contacts would be established. Ultimately, the performance of the solar cells is reduced [29].

I.2.3. Properties of organic solar cells

The distinctions between organic and inorganic solar cells are described below [32].

- A three-dimensional crystal lattice, various intramolecular and intermolecular interactions, local structural disorders, amorphous and crystalline regions, and chemical impurities are absent from organic solar cells.
- When Inorganic solar cells absorb light, the development of more free carriers are resulting, whereas, when organic solar cells absorb light, the formation of more excitons are resulting.
- Excitons have greater binding energy in organic solar cells than in inorganic solar cells.

I.2.4. Advantages and disadvantages [33-35]

The main advantages and disadvantages of organic photovoltaic cells in general and in particular of those based on interpenetrating network are as follows.

Advantages

- **Lightness and exibility:** Organic semiconductors are very light, which can be practical for large installations. In addition, they are less fragile than inorganic semiconductors, which must be deposited on flat and rigid substrates.
- **More effective exciton dissociation:** In interpenetrated networks, all the organic volume deposited is likely to collaborate in the photovoltaic conversion because any exciton generated is close to a separation zone regardless of the direction taken during its diffusion.

- **Ease of fabrication:** Organic PV cells can be produced relatively inexpensively in the laboratory, making their fabrication process easy and economical.
- **Self-assembly:** Indeed, chemical engineering can develop molecules that self-assemble. The proof of this is that in 2001, Shmidt - Mende realized a self-assembled solar cell based on liquid crystals of hexabenzocoronene and perylene[36].
- **Solubility:** Given that organic materials are soluble, they can therefore be obtained in liquid form (inks, paints) and therefore printed on various materials.
- **Transparency:** It is possible to create transparent cells, which open up many possibilities:

1. Bifacial use: solar energy can be captured by both sides, so it is possible to use these cells in a low-light environment.

2. Insertion into architectural elements: these cells can be inserted into joinery (windows, door, etc.) or on elements (roofs, walls, etc.).

3. Multi-layer use: Multiple transparent layers can be layered, which will increase cell efficiency.

Disadvantages

- **Limited absorption:** The energy bandgap of semiconductor polymers is typically greater than 2eV. This energy corresponds to a maximum absorption wavelength of 620 nm, which limits the absorption of solar radiation to 30%. In addition, there may also be losses due to transmission and scattering in the anode.
- **Reduced mobility:** The mobility of charge carriers is very low in organic materials compared to that of inorganic materials.
- **Collection efficiency limit:** photovoltaic cells based on a heterojunction in the volume are limited by the transport of charges. The electron-hole recombination taking place in the volume only allows the charges close to the electrodes to contribute to the photocurrent.
- **Instability over time:** a solar cell must be able to produce electricity for at least twenty years without a significant drop in performance.

I.3. Characterizations of solar cells

There are two standard methods for characterizing the operation of a solar cell, the current-voltage $(J-V)$ characteristics and the Quantum efficiency QE. $(J-V)$ Characterization provides the overall efficiency of the device, while the QE gives the response at each wavelength.

I.3.1. $(J-V)$ Characteristics

The electrical behaviour of any solar cell can be best described by its current-voltage $(J-V)$ characteristics, including the relevant parameters. As shown in Figure I.11, there are four parameters: open-circuit voltage (V_{oc}),short circuit current (J_{sc}), fill factor (FF), power conversion efficiency (η) [26, 37].

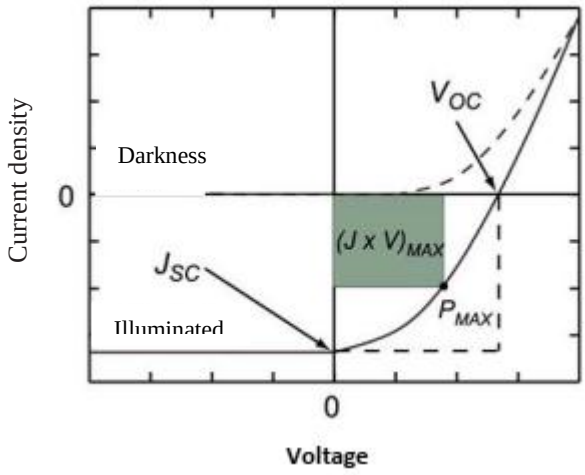

Figure I.11: $(J-V)$ characteristics of organic solar cells [38].

These parameters are:

- V_{oc} is the open circuit voltage, which is the voltage measured when no current flows in the cell; $J = 0$. Theoretically; it can be determined by the energy level difference between the (HOMO) level of the donor material and (LUMO) level of the acceptor material in devices

with ohmic contacts; if not, it is determined by the difference of work function of the contact electrodes [24, 39, 40].

- J_{sc} is the short circuit current density, it is the current corresponding to $V = 0$. This parameter is highly related to the property of absorption of donor material dependent on its band gap. The amount of J_{sc} is determined by the number of photogenerated carriers created in the active layer upon illumination process and the efficiency of the charge separation efficiency across the photoactive layer. Therefore, J_{sc} value can either be altered by modifying the structure leading to the lowest band gap or via altering the thickness of the active layer.
- There is a particular point on the curve $J\ (V)$, it is that which corresponds to the maximum power $P_{max} = J_{max}V_{max}$ represented by the shaded area of Figure.I.11.
- The Fill factor (FF) of the cells is determined by the factors like the shunt resistance, the series resistance, and recombination/extraction rate of the charge in the solar cell, which influence the cell effiecency and fully relatds to V_{oc}, J_{sc} and the morphology of active layer. It is given by the equation:

$$FF = \frac{P_{max}}{J_{sc}V_{oc}} = \frac{J_{max}V_{max}}{J_{sc}V_{oc}} \qquad \textbf{I.1}$$

- Finally, the efficiency η is defined by:

$$\eta = \frac{P_{max}}{P_{in}} = \frac{FF \times J_{sc} \times V_{oc}}{P_{in}} \qquad \textbf{I.2}$$

Where P_{in} is the input power.

I.3.2. Quantum efficiency (QE)

The quantum efficiency (QE) defines the number of charge carriers collected at the electrodes per number of incident photons on the solar cell area at a given wavelength. If every incident photon results in one collected charge carrier then the QE is equal to unity (no recombination losses). There are two types of quantum efficiency [41]:

I.3.2.1. External Quantum Efficiency (EQE)

External Quantum Efficiency (EQE) or often called Incident Photon to Charge Carrier Efficiency ($IPCE$) is the ratio between the number of collected carriers and the number of incident photons on the cell at a given wavelength [26, 41, 42].

$$EQE = \frac{J_{sc}(\lambda)}{\varphi(\lambda)} \times \frac{Eph(\lambda)}{e} = \frac{J_{sc}(\lambda)}{\varphi(\lambda)} \times \frac{hc}{e\lambda} \quad \textbf{I.3}$$

J_{sc} is the density of the short-circuit current, φ is the incident luminous flux, e the charge of the electron and Eph the photon energy with $Eph = hc/\lambda$ where h the Planck constant, c the speed of light in a vacuum and λ the wavelength.

The ratio $J_{sc}(\lambda)/\varphi(\lambda)$ is called the "spectral response" of the cell, it is noted $SR(\lambda)$ and represents the sensitivity of the cell to each wavelength. We can therefore rewrite the expression of the external quantum yield as follows:

$$EQE = SR(\lambda) \times \frac{hc}{e\lambda} \quad \textbf{I.3}$$

I.3.2.2. Internal Quantum Efficiency(IQE)

Internal Quantum Efficiency is the ratio between number of collected carriers and number of absorbed photons by the active layer of the device at a given wavelength. IQE does not take in to consideration the light transmitted through and reflected from the cell, as well as the light collected by the other layers that do not contribute in photo conversion process, it is just take into consideration the photons actually absorbed by the layer (absorption $A(\lambda)$). Thus, IQE is an indicator of pure electrical properties of solar cells to light, and is always greater than EQ [41, 42].

(IQE) can be expressed as follows:

$$IQE(\lambda) = \frac{EQE(\lambda)}{A(\lambda)} \quad \textbf{I.4}$$

CHAPTER II:

TCO/METAL/TCO MULTILAYERS TRANSPARENT ELECTRODE AND ITS APPLICATIONS.

II.1. Introduction

For use in big area solar systems and displays being developed for electronics and energy, transparent conductive electrodes are receiving more and more attention. Transparent and conductive oxides (TCO) based on In_2O_3, ZnO, or SnO_2 are often employed today, but novel electrodes with lower resistivities than previously attained and better optical characteristics than the current generation are needed for advanced devices.

TCO/metal/TCO multilayer structures have become an intriguing option because they have optical and electrical properties that are generally better than those attainable with a single-layer TCO or metal electrode and can be deposited at low temperatures onto affordable plastic substrates. In fact, roll-to-roll deposition techniques that can drastically lower production costs are being used to fabricate thin film devices on flexible substrates for use in lightweight products.

In this regard, organic electronics with minimal deposition temperature requirements stand the best opportunity of becoming the first to be converted from traditional glass to low-cost plastic substrates [16].

II.2. Materials and thickness selection to optimize the optical and electrical performance of TCO/metal/TCO electrode

To optimize the optical transmission and the electrical conduction for any transparent conductive electrode, materials and thickness selection are focused on the need and should be as large as possible. Hence, transparent conductive coatings are characterized by two main parameters: the sheet resistance (R_s) and the optical transmission (T), both depend on the coating thickness. The sheet resistance is: $R_s = 1/\sigma t$, where $\sigma(\Omega^{-1}\ \mathrm{cm}^{-1})$ is the electrical conductivity and $t(\mathrm{cm})$ is the coating thickness. The units of $R_s(\Omega/\mathrm{sq}\ )$ indicate that it measures the resistance of a square surface area independent of dimensions. The optical transmission T is given by: $T = I/I_0$ and is directly related to $exp(-\alpha t)$ where I_0 the radiation intensity entering the coating on

one side, I the radiation intensity leaving the sample on the opposite side and α (cm^{-1}) is the optical absorption coefficient.

TCO/metal/TCO multilayer structures work differently than electrodes based on single TCOs or metal thin films. The overall sheet resistance is mainly related to the metal film and is measured by $1/R_s = 1/R_{metal} + 2/R_{TCO}$ in which $R_{TCO} = 100\, R_{metal}$, $R_s = R_{metal}/1.02 \approx R_{metal}$. While the overall optical transmission is generally controlled by destructive interference in the beams reflected from the interfaces, also constructive interference in the corresponding transmitted beams through the multilayer structure and the transparent substrate. In this case, the electrical and optical performances achieved with the TCO/metal/TCO multilayer electrodes can be superior to that obtained with single layer TCO or metal thin films. The trilayer transparent electrode is represented in Figure II.1 [16].

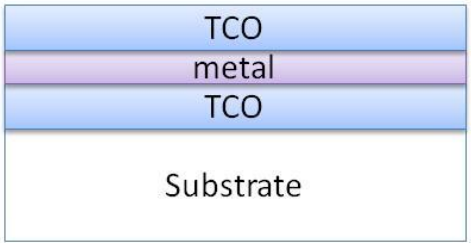

Figure II.1: TCO/metal/TCO multilayer structure.

II.2.1. Metal layer selection for optimum electrical performance

The metal layer is the key element to determine the sheet resistance in the TCO/metal/TCO design. Table II.1 listed the electrical resistivity values for bulk materials. According to that table, below 2 μΩ cm, Ag is the first and best choice because it has the minimum resistivity of all metals, followed by Cu which has only a slightly higher value [43].

Table II.1: Electrical resistivity value of several bulk metals [43].

Metal	Resistivity(μΩ cm) at 20°C
Ag	1.6
Cu	1.7
Au	2.4
Al	2.8
Mg	4.6
W	5.6
Mo	5.7
Zn	5.8
Ni	7.8
In	8.0
Pt	10.0
Pd	11.0
Sn	11.5
Cr	12.6
Ta	15.5
Ti	39.0

The transmittance and the sheet resistance change rapidly with metal layer thickness [44, 45]. A thin, continuous metal film may be transparent in the visible spectral range and exhibit strong electrical conductivity, but below a threshold film thickness, both electrical resistivity and optical absorption increase rapidly. This is due to a transition from a continuous film to one formed of distinct islands of metal atoms (aggregated state), which has properties that are quite different from the bulk metal [46]. The critical thickness for this transition, in general, is determined by the substrate and deposition conditions, as well as the specific metal [47, 48].

Figure II.2 presents the evolution of the sheet resistance and transmittance value as a function of metal layer thickness for Ag and Cu deposited by magnetron sputtering on soda lime glass

(SLG) substrate [49, 50]. When the film thickness of metal is raised from 5 to 15 nm, both optical and electrical characteristics show an abrupt decrease, the resistance being the steepest. It agrees with previous authors' theories about the evolution of thin film metal growth [46], This indicates that the change in slope is corresponded by a transition from metal clusters to a continuous layer [16].

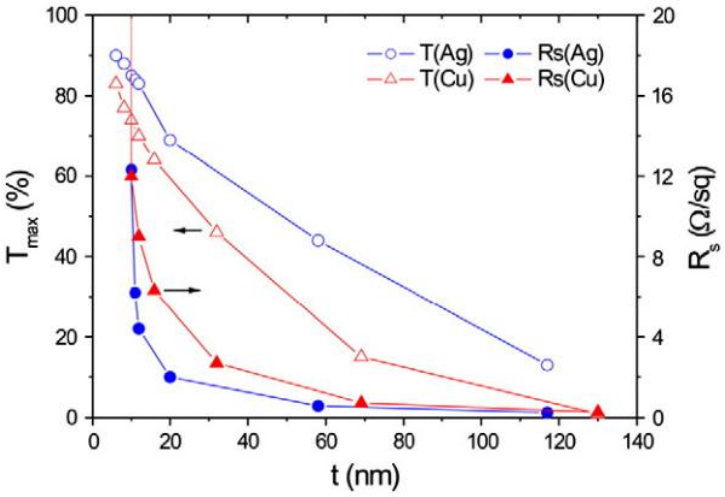

Figure II.2: Representation of the maximum transmittance and sheet resistance values obtained for sputtered Ag and Cu coatings as a function of film thickness.

The transmittance values above 60% for both Ag and Cu layers with thickness less than 20 nm are presented in Figure II.3. To estimate the optical losses due to metal films, not just the transmittance values T(%), but also the reflectance R(%), and therefore the absorptance A(%)= 100-T-R, should be known [51]. In Figure II.3, the transmittance and absorptance spectra of a 10-nm-thick Ag film and a 15-nm-thick Cu layer, both with the same 6 Ω /sq sheet resistance, are shown alongside the spectra of a soda lime glass substrate for comparison [52, 53].

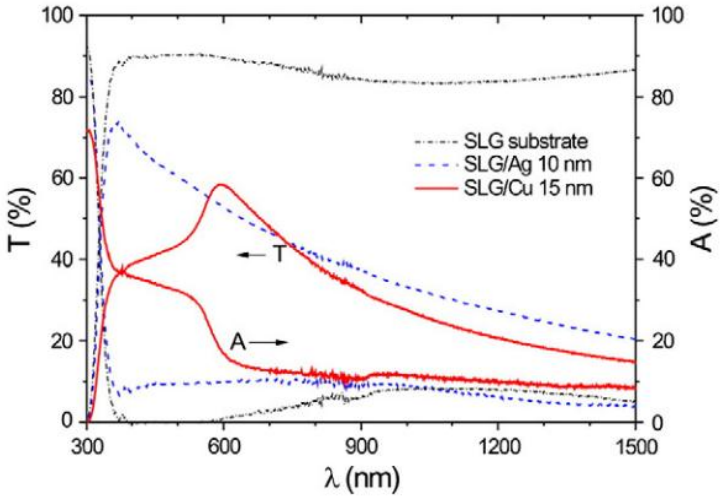

Figure II.3: Optical transmittance and absorptance spectra for a 10-nm-thick Ag film and a 15-nm-thick Cu layer deposited by magnetron sputtering on SLG substrates.

Ag is the most common metal interlayer for TCO/metal/TCO electrodes, according to the literature (see Table II.2). The table II.2 presents a collection of trilayer structures with reported sheet resistance of less than 15 Ω /sq and optical transmittance of more than 70%. The results are sorted by increasing metal film thickness. All of the TCO/metal/TCO structures were made by sputtering the TCO layers and sputtering or evaporation for the metal interlayer, all of which were done at room temperature without intentional substrate heating. In addition to standard glass substrates, such preparation processes are appropriate for low-cost manufacture on inexpensive thermoplastic substrates such as PET or PES, as well as PPC (polyphtalate carbonate), PEN (polyethylene naphthalate), and PC (polycarbonate) [54-56].

Table II.2: Values of optical transmittance (T) and sheet resistance (Rs) for several TCO/metal/TCO structures on different substrates, in OLED or OPV devices.

TCO/metal/TCO	*Substrate*	*T (%)*	*Rs (Ω/sq)*	*application*	*Ref*
ITO 50 nm/Ag 8 nm/ITO 50 nm	Glass	89	15	OPV	[54]
GIO 40 nm/Ag 8 nm/GIO 40 nm	Glass	92.9	11.3		[16]
ITO 37 nm/Ag(PdCu) 8 nm/ITO 37 nm	Glass	89	10	OLED	[57]
AZO 40 nm/Ag(PdCu) 8 nm/AZO 40 nm	Glass	88	10	OLED	"
ITO 30 nm/Ag 8 nm/ITO 30 nm	PEN	85	6.8		[58]
ZnO 57 nm/Ag 9 nm/ZnO 40 nm	Glass	95	7		[59]
ITO 35 nm/Ag 10 nm/ITO 35 nm	PET	77	10	OLED	[60]
ITO 35 nm/Ag 10 nm/ITO 35 nm	Glass	80	9	OLED	"
SnO2 45 nm/Ag 10 nm/ITO 45 nm	Arton	85	7		[16]
GZO 30 nm/Ag 10 nm/GZO 40 nm	Glass	90.7	7		[61]
ITO 30 nm/Ag 10 nm/ITO 30 nm	Glass	90	6		[49]
ITO 40 nm/Ag 10 nm/ITO 40 nm	Glass	87	6	OPV	[62]
ITO 45 nm/Ag 10 nm/ITO 45 nm	Arton	86	6		[63]
AZO 40 nm/Ag 10 nm/AZO 40 nm	PET	85	6		[64]

ITO 50 nm/AgCu-alloy 10 nm/ITO 50 nm	Glass	83	5.7		[65]
ITO 50 nm/Ag 10 nm/ITO 50 nm	Glass	88	5		[66]
ZnO 35 nm/Ag 12 nm/ZnO 35 nm	PET	75	10		[67]
GZO 30 nm/Ag 12 nm/GZO 30 nm	PES	87.2	7		[68]
IZO 30 nm/Ag 12 nm/IZO 30 nm	PET	84.8	6.9	OLED	[17]
AZO 40 nm/Ag 12 nm/AZO 40 nm	Glass	82	7	OPV	[69]
GZO 40 nm/Ag 12 nm/GZO 40 nm	Glass	87	6	OPV	"
ITO 40 nm/Ag 12 nm/ITO 40 nm	PES	89.3	4.3	OPV	[70]
ITO 50 nm/Ag 14 nm/ITO 50 nm	PET	81	11	OLED	[16]
ITO 70 nm/Ag 14 nm/ITO 70 nm	PPC	68	6.5	OPV	[71]
IZTO 30 nm/Ag 14 nm/IZTO 30 nm	PET	86	5	OLED	[72]
IZO 40 nm/Ag 14 nm/IZO 40 nm	Glass	87.7	4.2	OPV	[62]
ITO 40 nm/Ag 15 nm/ITO 40 nm	Glass	85	4.2		[73]
ITO 42 nm/Ag 15 nm/ITO 42 nm	Glass	85	3.3		[74]
ITO 43 nm/Ag 16 nm/ITO 43 nm	Glass	79.4	8.9		[75]
ITO 40 nm/Ag 16 nm/ITO 40 nm	Glass	86.5	4.4	OPV	[76]
ITO 50 nm/Ag 17 nm/ITO 50 nm	PET	83.2	6.7	OLED	[16]
ITO 54 nm/Ag 20 nm/ITO 54 nm	Glass	75	3.5		[56]

ZnO 50 nm/Cu 5 nm/ZnO 50 nm	Glass	83	10		[77]
ZnO 30 nm/Cu 6 nm/ZnO 30 nm	PEN	88	10		[78]
AZO 40 nm/Cu 8 nm/AZO 40 nm	Glass	84	9		[79]
ITO 40 nm/Cu 14 nm/ITO 40 nm	Glass	69	6	OPV	[62]
ITO 30 nm/Cu 16 nm/ITO 30 nm	Glass	88	6		[50]
AZO 50 nm/Au 9 nm/AZO 50 nm	Glass	83	12		[18]
ITO 50 nm/Au 10 nm/ITO 40 nm	PC	72	5.6		[80]
IZO 40 nm/Au 12 nm/IZO 40 nm	Glass	81.0	5.5	OPV	[13]

Pure silver is commonly used, but some Ag-based alloys such as Cu, Au, and Pd have also been used [54, 56, 65, 81]. According to these reports, such alloys can increase the electrode's thermal and moisture stability; nevertheless, some Cu or Au insertion has little effect on the transmittance and sheet resistance. When it comes to chemical stability, Pd–Cu outperforms Cu alone [94]. Furthermore, it was discovered that as the thickness of the Cu or Au layer is raised, the fall in transmittance is faster than that of Ag films. In order to retain a high transmittance value, the thickness must be lowered. The addition of a thin Fe layer to AZO/Fe/AZO structures has been proposed as a method of achieving ferromagnetic characteristics for specific applications, with overall transmittance and resistivity values on par with single-layer AZO electrodes [16].

II.2.2. TCO layers selection for optimum optical performance

Although TCO films made without heating have higher resistance, they can be used in TCO/metal/TCO structures since the metal conductivity dominates the total electrical

performance. Only enough TCO conductivity should be used to ensure a satisfactory electrical connection between the metal film and any location on the structure's surface. Their optical properties, on the other hand, are critical for the stack's transparency. TCO layers in stacked TCO/metal/TCO electrodes have the primary goal of increasing global transmittance in the visible spectral range by lowering reflection from the metal surface. Because reflectance losses are the primary cause of the metal film's low transmittance, it is feasible to increase the transmittance by adding antireflective coating layers. The goal is to fine-tune the interference processes that occur between multiple reflections at distinct interfaces in order to produce the lowest reflectance or highest transmittance in a given spectral region. TCO films of thicknesses in the 30–60 nm range are commonly employed for this purpose, and they are finely tuned to achieve maximum transmission at a certain wavelength, usually 550 nm [57], or optimum integral transmission in all the visible spectral region (400–800 nm) [65].

Several models for describing the optical properties of TCO/metal/TCO stacks have been proposed [16], and simulations based on the refractive indices, extinction coefficients, and component thicknesses have been utilized to maximize transmittance [57, 65]. In this regard, it's worth noting that simulations based solely on tabulated data can be far from accurate because the optical properties of TCO layers are highly dependent on the film thickness and oxygen concentration [16].

II.3. TCO/metal/TCO electrodes Characteristics

- TCO electrodes fail under lower mechanical strain than other device layers, while TCO/metal/TCO electrodes for flexible electronic devices have exhibited greater mechanical reliability than analogous single-layer TCOs [70, 82].

- The authors discovered that for ITO/Ag/ITO trilayer electrodes, employing 30-nm-thick ITO as shown in Figure II.4 and a 10-nm-thick Ag layer as shown in Figure II.3, and the same thickness of 30 nm for ITO film, the ITO/Ag/ITO structure crystallizes better than ITO single layer. TCO films with low crystallinity are expected due to the low process temperature

employed for deposition and the low layer thickness, notably for ITO, which is claimed to require typical thickness above 100 nm to crystallize at room temperature [83]. Other authors have reported similar behaviour for ITO/Au/ITO trilayer electrodes, in which the Au layer appears to be successful in crystallizing the upper ITO film with a thickness of 30–45 nm. The AZO/ Ag/AZO samples, which showed superior ZnO crystallization than AZO layers placed onto bare SLG or PET substrates, show a similar result [16, 49, 64].

- There is a trade-off in the design of single-layer TCO electrodes for flexible applications between utilizing a thick TCO layer to reduce sheet resistance and using thinner films that can endure more substrate strain. This can be solved by using TCO/metal/TCO electrodes, which offer greater electrical performance while reducing TCO thickness significantly [16].

- The crystallinity of the ITO film is significantly improved by adding a ductile metal underlayer, also the mechanical reliability and flexibility of TCO/Ag/TCO multilayer structures were also improved compared to single-layer TCOs [16].

- The ability to demonstrate good quality even at room temperature deposition is a major advantage of TCO/metal/TCO electrodes, enabling for low-cost manufacture on low-cost plastics [16].

- To test the stability of their optical and electrical properties, various single-layer TCOs were subjected simultaneously to moist atmospheres (over 70% humidity) at moderate temperatures (usually below 90 °C). Samples deposited on soda lime glass decayed faster than those deposited on alkali-free glass. In other hand, in air at a relative humidity of 90% and a temperature of 60 °C, ITO/Au/ITO structures show good stability in terms of metal interlayer use; the normalized sheet resistance remained constant over a 600-hour exposure time [16].

II.4. Application of TCO/metal/TCO electrodes in electronic devices

Although it has been established that suitable transmittance and sheet resistance values can be achieved with a variety of TCO/metal/TCO combinations, the best electrode material for a given application is also determined by the work function value of the TCO in relation to the energy level of the next layer in the device construction, because the contact interface should present the smallest possible barrier to carrier transport. As previously stated in the introduction, the TCO/metal/TCO electrodes have primarily been used in OLEDs and OPVs [13, 54, 62, 70, 71, 76]. The trilayer electrode is typically utilized as an anode in these devices, with two or more active organic layers layered between the upper TCO film of the anode and another metallic film used as cathode, as shown in Figure II.4. In semitransparent OLEDs with single-layer TCO anodes, the utilization of trilayer structures as cathodes has been reported [16].

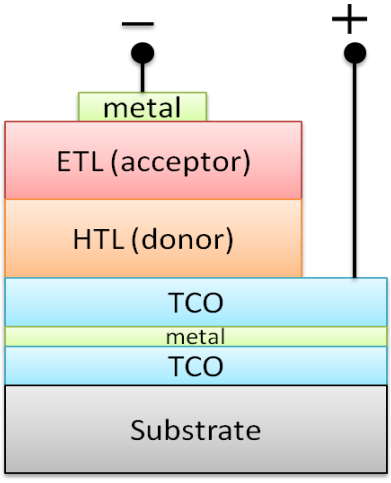

Figure II.4: Schematic of simple device with a TCO/metal/TCO anode.

The band alignment between the TCO and the adjacent organic layer is critical for device performance, however, different aspects must be considered for OLEDs and OPVs depending on the injection or extraction procedures shown in Figure II.5. The injection barrier between the electrode and the organic semiconductor is clearly a significant parameter of the TCO/organic

interface in the case of OLEDs. The energy differential between the electrode work function and the organic material's highest occupied molecular orbital (HOMO) determines this. The lower the barrier, the more efficiently holes are injected across the interface, and hence the device performs better. In OPVs, where the carrier must travel from the HOMO to the electrode Fermi level, this impact is less prominent. In reality, for both carrier injection and extraction, the energy barrier at the TCO/ organic contact should be as low as possible [84]. TCO/metal/TCO electrodes' work function is obtained in general from the TCO upper layer [58, 67], as evidenced by various measurements that yielded the same results for ITO/Ag/ITO and ITO/Ni/ITO samples as for equivalent single-layer ITO electrodes [57, 81, 85].

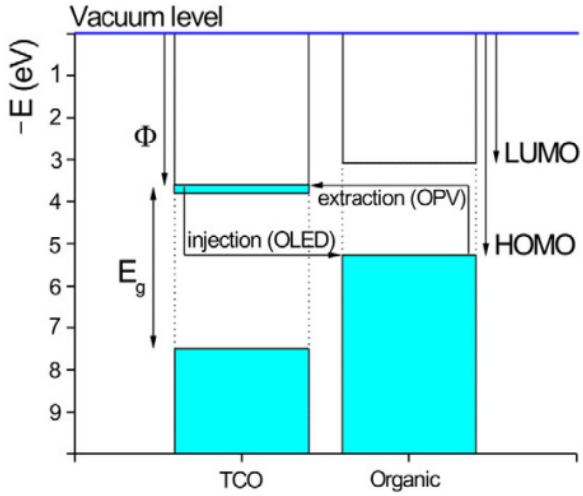

Figure II.5: A band diagram for TCO anode and a close organic material. In OLEDs, the TCO anode is utilized for hole injection, while in OPVs, it is used for photogenerated hole extraction.

Transparent and flexible capacitors, as well as non-volatile memory devices, have been the subject of recent research as steps toward the realization of increasingly complicated transparent and flexible electronic systems. Fully transparent resistive random access memory (TRRAM) devices based on ITO/ZnO/ITO/Ag/ITO multilayered structures fabricated on flexible PES substrates have high transparency of up to 80%, superior flexibility due to the bottom trilayer

electrode, excellent resistive switching characteristics, and reliable data retention properties that have been verified at room temperature and under thermal stress [82]. Furthermore, capacitors made of Pt/Bi3NbO7/AZO/Ag/AZO multilayered structures grown on PES substrates show good dielectric and leakage properties as well as good mechanical stability for flexible electronic applications [86].

On ITO-coated PET substrates, the first flexible OLEDs with small molecules were created in 1997. ITO films are currently used as single-layer anodes in flexible OLEDs, but the use of TCO/metal/TCO multilayer anodes with lower sheet resistance is proving to be a successful solution to improve mechanical stability and device efficiency. For both glass and PET substrates, multilayer transparent electrodes consisting of ITO/Ag/ITO with visible transmittance above 80% and sheet resistance of roughly 10 Ω / sq were employed as anodes in the device configuration substrate/ anode/CuPc/NPB/Alq3/metal-cathode. They have better efficacy than a single-layer ITO anode, and at a luminance of 10^4 cd/m^2, the power efficiency (in cd/W) of samples with ITO/Ag/ITO electrodes improves by 22% compared to samples with ITO anodes [16].

Furthermore, using trilayer electrodes for flexible OLEDs can lower the drive voltage, minimize the heat generated by the devices, and improve device efficiency and lifetime [41]. Several TCOs have been employed as multilayer anodes in flexible OLEDs grown on PET substrates, including ITO/Ag/ITO [87], IZO/Ag/IZO [43], and IZTO/Ag/IZTO [72]. In the 5–12 V range, they have a higher current density and luminance than equivalent devices constructed using single-layer ITO anodes.

ITO/Ag/ITO multilayers are also used as a transparent cathode in transparent OLEDs with the configuration glass/ITO-anode/PEDOT:PSS/PFO/LiF/trilayer-cathode, as well as in small molecule devices with the configuration glass/ITO-anode/PEDOT:PSS/NPB/Alq3/LiF /trilayer-cathode [88].

II.5. Application of TCO/metal/TCO electrodes in OPV devices

Organic photovoltaics are gaining popularity as a renewable, cost-effective, and low-cost energy source alternative to standard Si-based solar cells [89, 90]. Because of their simple fabrication process and device structure, as well as their ability to flex, roll, and fold for portability, bulk-heterojunction cells using networks of conjugated polymers and fullerene derivatives are the most widely investigated systems among the various types of OPV devices. Bulk heterojunctions containing the semiconducting polymer poly-3-hexylthiophene (P3HT) as an electron donor and the soluble fullerene derivative (6,6)-phenyl-C61 butyric acid methylester (PCBM) as an electron acceptor, in particular, are being studied extensively because theoretical studies predict an external efficiency of 11%. In practice, record power conversion efficiency (PCE=Pout/Pin) of 6% and average values of 4–5% on glass substrates after thermal annealing have been reported for P3HT:PCBM-based organic solar cells.

Unheated materials on flexible substrates produce PCE below 4% in most cases. In P3HT:PCBM-based solar cells, TCO/metal/TCO multilayer anodes have been used, and they provide greater power conversion efficiencies than single-layer TCO electrodes. Table II.3 compares the performance of an OPV device made with multilayer anodes to that of the identical device made with a single-layer TCO anode [16].

Table II.3: Parameters of several OPVs devices with TCO/metal/TCO electrodes.

Anode	*Active layer*	*Jsc (mA/cm2)*	*Voc (V)*	*FF*	*PCE (%)*	*Ref*
ITO 40 nm/Ag 10 nm/ITO 40 nm	P3HT:PCBM	8.49	0.56	0.69	3.26	[62]
ITO 40 nm/Cu 14 nm/ITO 40 nm		7.11	0.56	0.70	2.78	"
ITO 80 nm		7.41	0.50	0.46	1.72	"

AZO 40 nm/Ag 12 nm/AZO 40 nm	P3HT:PCBM	9.41	0.50	0.46	2.14	[69]
AZO 500 nm		9.20	0.48	0.31	1.36	"
GZO 40 nm/Ag 12 nm/GZO 40 nm	P3HT:PCBM	9.86	0.54	0.53	2.84	"
GZO 500 nm		8.00	0.50	0.39	1.57	""
ITO 40 nm/Ag 12 nm/ITO 40 nm	P3HT:PCBM	9.30	0.56	0.72	3.73	[70]
ITO 80 nm		9.61	0.54	0.62	3.21	"
ITO 70 nm/Ag 14 nm/ITO 70 nm	P3HT:PCBM	9.58	0.51	0.39	2.00	[71]
ITO 150 nm		3.33	0.39	0.35	0.48	"
IZO 40 nm/Ag 14 nm/IZO 40 nm	P3HT:PCBM	8.13	0.54	0.69	3.05	[13]
IZO 40 nm/Au 12 nm/IZO 40 nm		7.04	0.56	0.68	2.66	"
ITO 40 nm/Ag 16 nm/ITO 40 nm	P3HT:PCBM	9.22	0.54	0.65	3.25	[76]
ITO 150 nm		7.53	0.55	0.56	2.35	"
ITO 50 nm/Ag 8 nm/ITO 50 nm	CuPc–C60	2.89	0.47	0.40	0.57	[54]
ITO 100 nm		2.81	0.47	0.37	0.52	"

On rigid glass [62, 76] and flexible PES [70] and PPC [71] substrates, transparent electrodes consisting of ITO/Ag/ITO with sheet resistance in the 4–6 Ω /sq range have been used as anodes in the device configuration substrate/anode/PEDOT:PSS/P3HT:PCBM/metal-cathode. Devices with a multi-layer ITO anode have a better conversion efficiency than those with a single-layer

ITO anode. ITO/Ag/ITO and ITO/Cu/ITO electrodes with the same 6/ sq sheet resistance were compared for devices produced on glass substrates [62], and both demonstrated similar open circuit voltage (Voc) and fill factor (FF) values higher than those obtained with single-layer ITO anodes. They did, however, differ in terms of short circuit current density (Jsc). For a normal solar spectrum, with the incident illumination power Pin= 100 mW/cm^2, the power conversion efficiency of solar cells is calculated as PCE=Voc Jsc FF/Pin. The decreased multilayer electrode resistance is responsible for the observed FF rise. Both the series and shunt resistances have a significant impact on the FF value of solar cells. The anode and cathode sheet resistances, as well as the transverse current flow in the solar cell, are all sources of series resistance. As a result, the fill factor and current density of photovoltaic devices are greatly affected by the sheet resistance of the multilayer electrode to current flow [62, 76]. Despite having the same sheet resistance, the ITO/Ag/ITO electrode had a larger short circuit current density than the ITO/Cu/ITO electrode. This was attributed to the optical transmittance of the P3HT:PSS active layer in the wavelength range of 400–600 nm, which is its absorption region [71]. Because of the optical scattering of the added Cu film, the average transmittance of the ITO/Ag/ITO anode was roughly 20% higher than the ITO/Cu/ITO multilayer at such wavelengths [62]. The combination impact of high transmittance tailored to the absorption region of the active layer and very low sheet resistance arising from the conductive Ag film can therefore explain the greater conversion efficiency achieved with the OPV device constructed on the ITO/Ag/ITO electrode.

The significant improvement in conversion efficiency obtained by using ITO/Ag/ITO in place of ITO electrodes for devices grown on flexible PES or PPS substrates has also been attributed [70, 71] to the low sheet resistance of the multilayer anode in addition to the good fit of its optical characteristics with the absorption region of the organic layer as previously mentioned. Due to the limited active area of these solar cells (usually around 0.05 cm^2 [62, 70, 76]), determining the true benefit of trilayer electrodes against single-layer TCOs is difficult. For larger area devices, the effect of decreased sheet resistance for multilayer electrodes on the performance of flexible OPVs is expected to be even more critical.

By comparing IZO/Ag/IZO and IZO/Au/IZO anodes with similar sheet resistances in solar cells with a P3HT:PSS active layer, the influence of the metal interlayer has also been investigated

[13]. V_{oc} and FF values were similar due to the same sheet resistance and device structure. The IZO/Ag/IZO anode, on the other hand, has a greater current density and conversion efficiency due to its better optical transmittance. The average transmittance of the IZO/Ag/IZO electrode was nearly 10 % greater than the IZO/Au/IZO anode in the wavelength band 400–600 nm, which corresponds to P3HT:PSS absorption, resulting in a higher current density [13].

Indium-free TCOs were tested in multilayer structures with optimized sheet resistance and visible transmittance parameters, AZO/Ag/AZO ($7\,\Omega/sq, 82\,\%$) and GZO/Ag/GZO ($6\,\Omega/sq, 87\,\%$), as well as in annealed single-layers of AZO ($74\,\Omega/sq, 93\,\%$) and GZO ($30\,\Omega/sq, 94\,\%$), which were applied and compared as alternative anodes in the device configuration glass/anode/PEDOT:PSS /P3HT:PCBM/metal-cathode [69]. The solar cell made with the GZO/Ag/GZO electrode had the highest conversion efficiency of 2.84 %, followed by the cell made with the AZO/Ag/AZO anode, which had a conversion efficiency of 2.14 %.

The efficiency of the devices built on single-layer GZO and AZO electrodes was 1.57 % and 1.36 %, respectively. Although the conversion efficiency of the solar cell fabricated with the GZO/Ag/GZO electrode is slightly lower than that obtained with ITO-based multilayer anodes in the same device structure (see Table II.3), it is significantly higher than that reported for other cells with single-layer GZO electrodes 188,189], where the low efficiency has been attributed to GZO's small work function. Lower sheet resistance resulting from the insertion of the Ag layer, which enhanced the fill factor and current density of the OPV devices, has been linked to the higher efficiency achieved with multilayer electrodes.

When planar heterojunctions based on the CuPc–C60 donor-acceptor couple were used to compare ITO and ITO/Ag/ITO anodes in the glass/anode/PEDOT:PSS/CuPc/C60/BCP/Al-cathode configuration, the simultaneous measurement of the anode transmission and photogeneration spectra revealed that the best contribution to photocurrent production was in the 600–750 nm wavelengths region, which corresponded to the strongest phthalocyanine absorption, and where the multilayer anode transmission dropped from its maximum value obtained at about 550 nm [54]. Because of this, the use of a multilayer electrode in CuPc–C60-based devices resulted in low photocurrent and conversion efficiency, despite the fact that the FF was high due to the low sheet resistance [54]. The match between the most transparent range of the anode and the

absorption zone of the active organic material is critical for obtaining high conversion efficiency OPV devices. As a result, different organic solar cells require optimized anode layers.

CHAPTER III:

SIMULATION OF ORGANIC SOLAR CELLS.

III.1. Introduction

Simulation is the process of utilizing a computer to solve complex equations (usually second order differential equations) that describe concerned phenomena. The solution of equations can give behavior prediction of a real experience. Semiconductor simulation requires the numerical solution of equations describing the physics of semiconductor materials like drift diffusion, Poisson equation, and carrier continuity equations. Physically-based simulation is becoming very important for two reasons. One, it is always much quicker and cheaper than performing experiments. Two, it provides information that is difficult or impossible to measure. There are a number of available modeling tools for solar cells, among them: AMPS, wxAMPS, PC1D, AFORS-HET, ASA, SCAPS-1D, GPVDM and SILVACO TCAD[31, 91].

The simulation of solar cells (and other semiconductor devices) is based on defining their structures and the physics models used, and solving equations that describe the transport phenomena in semiconductors (the active layer). The output of simulation is current-voltage characteristics and solar cell internal parameters such as carriers ‘concentration, recombination…etc.

Analytical modelling is, in the other hand, solving the equations describing the material behavior with certain variables analytically since they are not complicated as in the numerical simulation. It usually involves direct simple relations or first order differential equatios which return analytical formula between variables.

In this work two softwares are used to numerically simulate solar cells, namely SILVACO TCAD and GPVDM. In addition, MATLAB is used to analytically used to sole the equations describing the materials used to optimize multipl-layer electrodes for these solar cells. Therefore, these tools are the subject of this chapter.

III.2. Basic physical models (numerical simulation)

The charge transport in the devices is described by a 1-D and time-independent drift-diffusion model, consisting of Poisson's equation (III.1), coupled with the continuity equation for electrons (III.2.a) and holes (III.2.b) [91]:

$$\frac{d^2\psi}{dx^2} = -\frac{q}{\varepsilon}\big(p(x) - n(x)\big) \qquad \textbf{III.1}$$

$$\frac{d}{dx}J_n(x) = q(R_e - \mathrm{G}) \qquad \textbf{III.2.a}$$

$$\frac{d}{dx}J_p(x) = q(R_h - \mathrm{G}) \qquad \textbf{III.2.b}$$

q is the elementary charge, $\psi$the electrostatic potential,$n(x)$ and $p(x)$are the electron and hole densities, ε is the dielectric constant., $R_{e(h)}$and G are the recombination and the generation rates of free carriers. The electron (hole) current density$J_{n(p)}(x)$[91]:

$$J_n = -qn\mu_n\frac{\partial}{\partial x}\psi + qD_n\frac{\partial}{\partial x}n \qquad \textbf{III.3.a}$$

$$J_p = -qp\mu_p\frac{\partial}{\partial x}\psi - qD_p\frac{\partial}{\partial x}p \qquad \textbf{III.3.b}$$

With$\mu_n$and $\mu_p$are the electron and hole mobility.$D_{n(p)}$ are the carrier diffusion coefficients, which are assumed to obey the Einstein relation[91].

$$D_{n(p)} = \mu_{n(p)}V_t \qquad \textbf{III.4}$$

V_t is the thermal voltage, i.e., $V_t = K_BT/q$, where $K_B$is the Boltzmann constant and $T$is the absolute temperature.

III.2.1. Carrier trapping, de-trapping and recombination model used in GPVDM software

The disordered organic semiconductors have a wide density of states close to the HOMO and LUMO energies [92]. Due to the structural and energetic disorder, an energetic distribution of localized gap states is created [93]. Additionally, defect states acting as traps have a tail shape distribution [94].

For a polymeric material, trapping and de-trapping are closely linked to the trap distribution. The trapping model is based on three processes: charge injection, trapping and de-trapping [95]. The origin of defects may be physical or chemical. The physical defects are induced by any deviation of the morphological crystallinity ratio, microstructure, and molecular weight [95, 96]. The chemical defects are caused by photo-oxidation process, which can change the chemical structure of the material [95, 96]. It has been pointed out that physical defects are correlated with shallow traps while chemical defects are related to deep traps [95, 96].

Although the Gaussian shape of the density of states (DOS) is the most common assigned distribution, an exponential DOS or a combination of both is also a possibility[97]. Alternatively, two Gaussians centered around LUMO and HOMO levels is another model [98].

Recently, Shockley–Read–Hall (SRH) recombination statistics have been used in OPVs including organic solar cells (OSC) and polymer light emitting diodes (PLEDs). In steady state, this model describes recombination of free-to-trapped carriers, and thus is similar to Langevin recombination model that contains carriers traps[98].

Figure III.1 shows the shape of the DOS across with the gap energy and the related trapping and recombination process. In this work the model composed of exponentially decaying tail states DOS, that act as trap states for free carriers, is considered. In addition, the carrier extended states are described by parabolic bands with LUMO energy as minima for electrons and HOMO energy as maxima for holes [98].

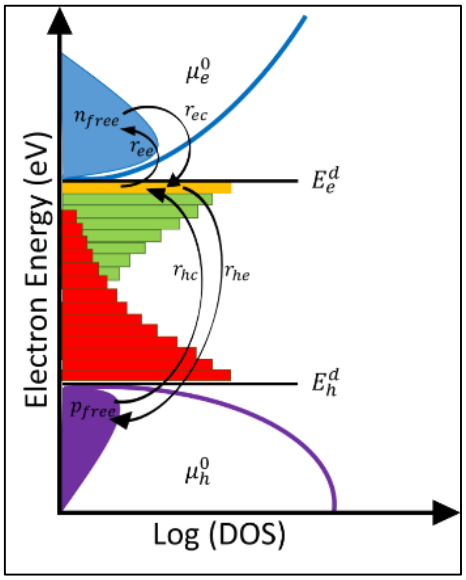

Figure III.1: The density of states (DOS) of the active P3HT: PCBM layer for both extended and trap states.

The carrier trapping and recombination are described using free-to-trap Shockley-Read-Hall recombination model for both electrons and holes. For each trap level the carrier balance equation is given by [99]:

$$\frac{\delta n_t}{\delta t} = r_{ec} - r_{ee} - r_{hc} + r_{he} \qquad \textbf{III.5}$$

Where n_t is the trapped electron density. The rates r_{ec}, r_{ee}, r_{hc} and r_{he} that define, respectively, electron and hole capture and escape are defined as follows:

$$r_{ec} = nv_{th}\sigma_n N_t(1-f), r_{ee} = e_n N_t f, r_{hc} = pv_{th}\sigma_p N_t f, r_{he} = e_p N_t(1-f) \qquad \textbf{III.6}$$

A similar equation is given to trapped hole density p_t:

$$\frac{\delta p_t}{\delta t} = r_{hc} - r_{he} - r_{ec} + r_{ee} \qquad \textbf{III.7}$$

Electrons and holes escape rates e_n and e_p, respectively, are given by [99]:

$$e_n = v_{th}\sigma_n N_c exp\left(\frac{E_t - E_c}{KT}\right) \quad \textbf{III.8.a}$$

$$e_p = v_{th}\sigma_p N_v exp\left(\frac{E_v - E_t}{KT}\right) \quad \textbf{III.8.b}$$

where v_{th}, $\sigma_{n,p}$and $N_{c,v}$are the thermal emission velocity of the carriers, the trap cross sections and the effective density of states for free carriers,f is the Fermi-Dirac occupation function. $N_t$is the trap density of the exponential tail distribution.

At a given energy E ,$N_t(E)$ for any given trap level is obtained by averaging the DOS function over the energy range (ΔE) which the trap occupies [99]:

$$N_t(E) = \frac{\int_{E-\Delta E/2}^{E+\Delta E/2} N^{e/h} exp\left(E/E_u^{e/h}\right) dE}{\Delta E} \quad \textbf{III.9}$$

Where $E_U^{e/h}$is the characteristic tail slope energy,$N^{e/h}$is the trap density at the LUMO (HOMO) band edges.

Recombination rates $R_e(R_h)$ of electrons (holes) is then the net difference between the all captured by and those escaped from $\int_{HOMO}^{LUMO} N_t(E)dE$ [98, 99].

III.2.2. Recombination model used in SILVACO atlas

In Braun's model, the probability of electron-hole pair dissociation depends on temperature T and field strength F and given by[100]:

$$P(x,T,F) = \frac{K_{diss}(x,T,F)}{K_{diss}(x,T,F) + K_f(T)} \quad \textbf{III.10}$$

The bound electron-hole pair may decay to the ground state with a decay rate $K_f$or dissociate (rate constant K_{diss}) into free carriers.

In disordered organic semiconductors, the Langevin bimolecular recombination mechanism is expected to be applicable and described as [101]:

$$R = \gamma(np - n_i^2)np \qquad \textbf{III.11}$$

Where$n_i = N_c exp(-E_{gap}/2V_t)$, is the intrinsic carrier density of electrons and holes. The recombination strength $\gamma$is given by the Langevin[100, 102].

$$\gamma = \frac{q}{\langle\varepsilon\rangle}\langle\mu\rangle \qquad \textbf{III.12}$$

$\langle\varepsilon\rangle$ is the spatially averaged dielectric constant and $\langle\mu\rangle$is the spatially averaged sum of hole and electron mobility[100, 103].

Assuming Maxwell–Boltzmann statistics, the electron and hole concentrations are expressed as[91]:

$$n = N_{LUMO} exp\left(\frac{E_{Fn} - E_{LUMO}}{K_B T}\right) \qquad \textbf{III.13.a}$$

$$p = N_{HOMO} exp\left(\frac{E_{HOMO} - E_{Fn}}{K_B T}\right) \qquad \textbf{III.13.b}$$

Where E_{LUMO} and E_{HOMO} are the energy levels of LUMO and HOMO, $E_{F,n}(E_{F,p})$ is the quasi-Fermi level for electrons (holes) and $N_{LUMO}(N_{HOMO})$ is the density of states in the LUMO (HOMO)[25].With the intrinsic carrier density n_i:

$$n_i = N_0\left(-\frac{E_g}{2K_B T}\right) \qquad \textbf{III.14}$$

Because of the disordered structure, most organic materials have electric field dependent mobility. The electric field dependence of mobility can be modeled by the Poole-Frenkel equation[101].

$$\mu(E) = \mu_0 exp\left(\sqrt{E/E_0}\right) \qquad \textbf{III.15}$$

With the zero-field mobilityμ_0, the electric field$E = -d\psi/dx$, and a material related parameter E_0 known as the characteristic field.

As opposed to inorganic semiconductors, the density of states for organic semiconductors is described by a Gaussian shape since transport is assumed to occur via a hopping process between uncorrelated sites. Thus, polymers and small molecules have broadened energy levels of their highest occupied molecular orbital (HOMO) and lowest unoccupied molecular orbital (LUMO) as shown in Figure III.2 and are described in the following way [91, 104].

$$N_{Gauss}(E) = \frac{N_0}{\sqrt{2\pi\sigma^2}} exp\left[-\left(\frac{E-E_0}{\sqrt{2}\sigma}\right)^2\right] \quad \textbf{III.16}$$

N_0denotes the site density, σ the width of Gaussian and E_0 the reference energy level.

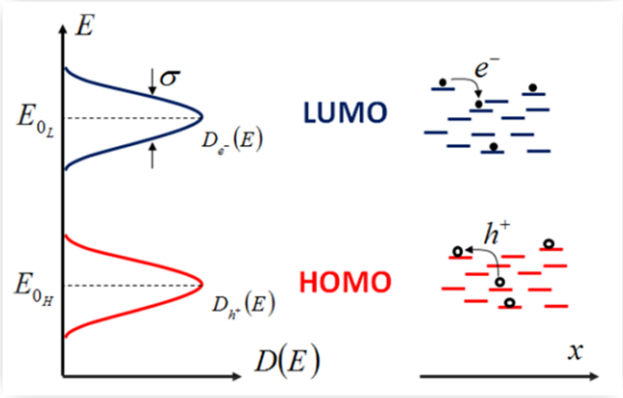

Figure III.2: Illustration of the Gaussian distribution of LUMO and HOMO states (left) and of the hopping transport mechanism (right)[104].

In the extended Gaussian disorder model, the Gaussian density of states affects charge diffusion. Tessler pointed out that the use of the generalized instead of the classical Einstein relation is appropriate The generalized Einstein diffusion coefficient is now determined by [105]:

$$D = \frac{K_B T}{q}\mu(T,p,F)g_3(p,T) \quad \textbf{III.17}$$

where the enhancement function $g_3$is given by [105]:

$$g_3(p,T) = \frac{1}{K_B T}\frac{p}{\frac{\partial p}{\partial E_f}} \quad \textbf{III.18}$$

Using the expression[105]:

$$p(E_F) = \int_{-\infty}^{\infty} DOS(E)\, f\left(E, E_f\right) dE \qquad \textbf{III.19}$$

For the density and inserting the Fermi-Dirac distribution and the Gaussian DOS we obtain[105]:

$$\frac{D}{\mu} = \frac{K_B T}{q} \frac{\int_{-\infty}^{\infty} N_{Gauss}(E) \frac{1}{1+exp\left(\frac{E-E_F}{KT}\right)} dE}{\int_{-\infty}^{\infty} \frac{N_{Gauss}(E) exp\left(\frac{E-E_F}{KT}\right)}{\left[1+exp\left(\frac{E-E_F}{K_B}\right)\right]^2} dE} \qquad \textbf{III.20}$$

III.3. GPVDM software

III.3.1. An overview of GPVDM software

GPVDM (general-purpose photovoltaic device model) is a free tool to simulate thin film optoelectronic devices including, organic solar cells, perovskite solar cells, thin film light emitting diodes and transistors beside silicon/CIGS-based devices. The 1/2D electrical and optical solvers in the model allow for the simulation of a device's current/voltage and optical characteristics.

III.3.1.1. Running GPVDM

GPVDM can install on both Windows and Linux. After clicking on it to start it, a window similar to that in figure III.3 will open:

Figure III.3: First window cotains deferent device structures type.

After choosing the structure and its pathway to save, a window like figure III.4 will appear.

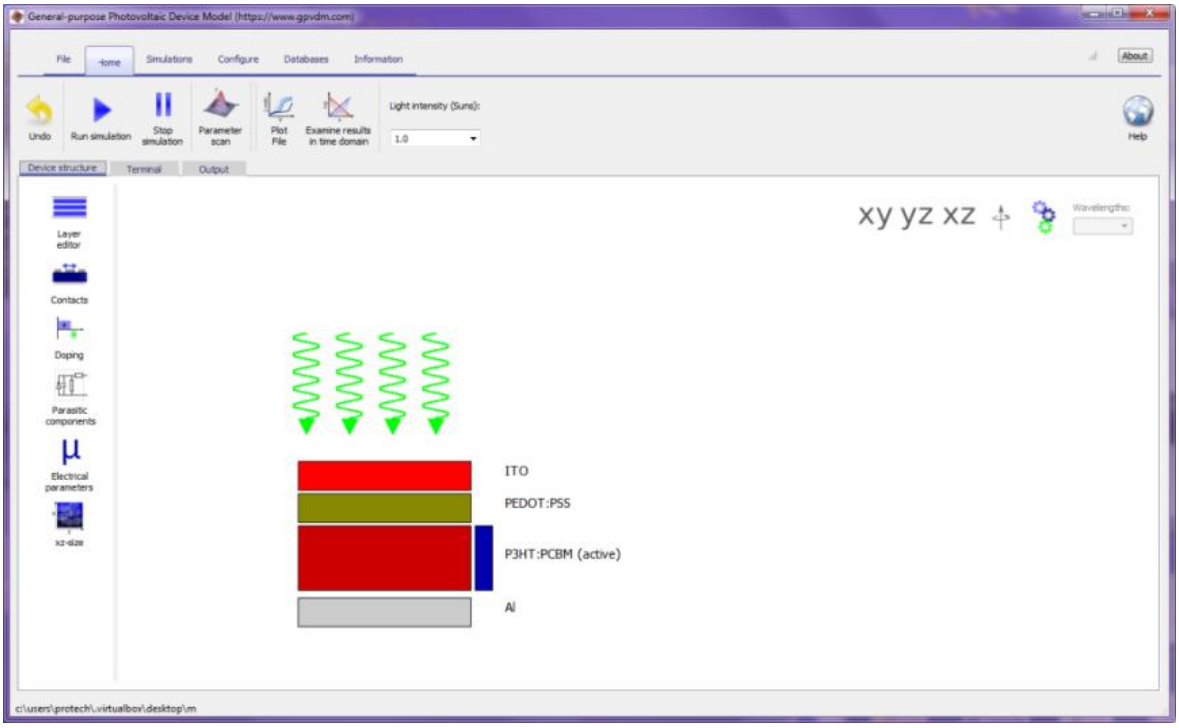

Figure III.4: The main window, with a picture of the structure on the right and the device layer editor on the left.

III.3.1.2. The layer editor

To set up and edit the vertical device structure, use the layer editor in figure III.4. Using this tool, you can add layers, remove layers, and move layers up and down (figure III.5).

The first column: This is a name of the layers.

The second column: The thickness of the layer in meters.

Third column: Sets the optical material properties.

Forth column: Select the type of layer (Active layer; contact or other).

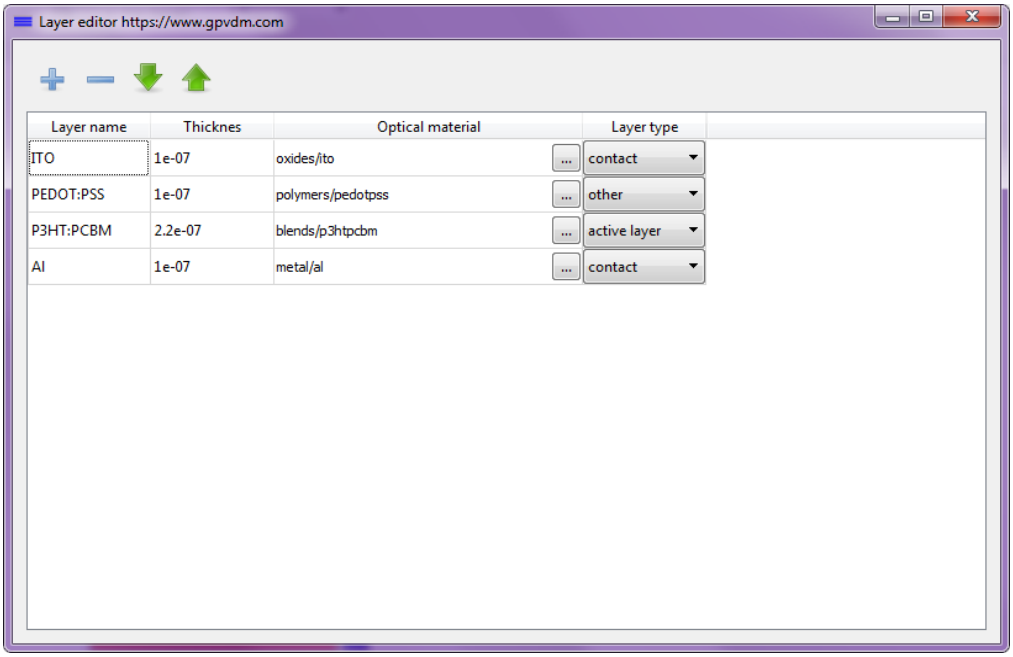

Figure III.5: Layers editor.

III.3.1.3. Define the electrical parameters

The tab "electrical parameters" in figure III.4 contains the material parameters for active layer. These include mobility, affinity, permittivity and band gap…etc (figure III.6).

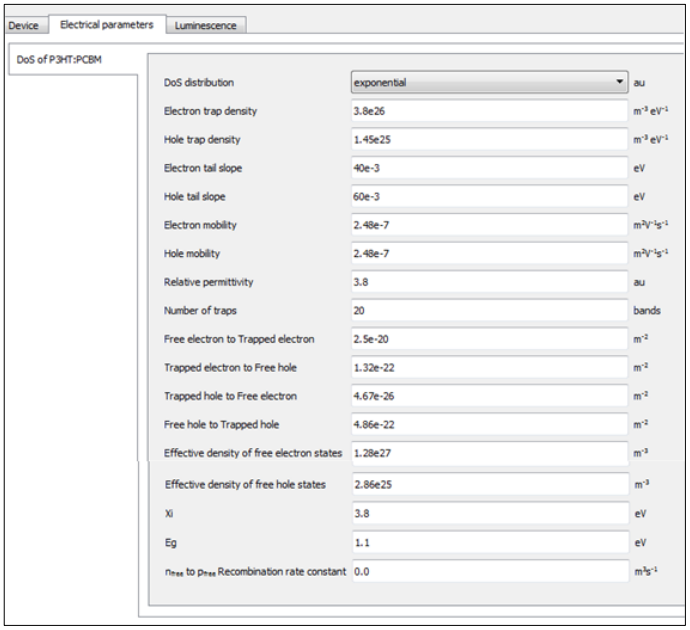

Figure III.6: Electrical parameters.

III.3.1.4. The calculations and displaying the results

The calculation will begin after clicking on "Run simulation" in figure III.7. The simulation outputs results and J-V curve (figure III.8) will be found after clicking on "plot file" then open the file "sim_info.dat" and in "jv.dat".

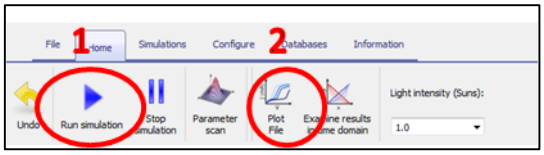

Figure III.7: Running simulation and display the results.

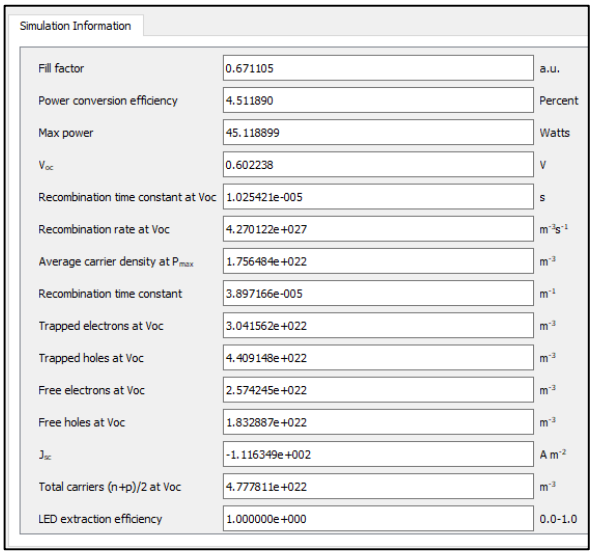

Figure III.8: Results panels.

III.4. SILVACO-ATLAS Simulator

III.4.1. Presentation

SILVACO is a company that specializes in the creation of simulation software targeting almost every aspect of modern electronic design. The phenomena modeled range from simple electrical conductivity to such things as thermal analysis, radiation and laser effects. A wide variety of detailed layer-growth processes and material properties (e.g. mobilities, recombination, ionization coefficients, and optical parameters) add to the accuracy of the simulation [91].

ATLAS is a physically-based two and three-dimensional device simulator. It predicts the electrical behaviour of specified semiconductor structures and provides insight into the internal physical mechanisms associated with device operation. The software takes a two- and three-dimensional input structure, which is specified and gridded by the user through an input program and solves the differential equations derived from Maxwell's laws to simulate the transport of carriers within the structure at each of the points of the grid. The user can specify any type of device using a large library of conductors, semiconductors, and insulators and can use solve statements to simulate the behaviour of a device under certain conditions[91].

III.4.2. Working with ATLAS

The text input deck, Deckbuild, is used for the specification and solve statements of devices. In Deckbuild, users type input commands that first specify the structure and then put the conditions for simulating its behavior. These statements must follow a set structure to properly run the ATLAS software [106].The Deckbuild window is represented in figure III.9. It is considered as SILVACO's main window, from which all simulators can be managed.

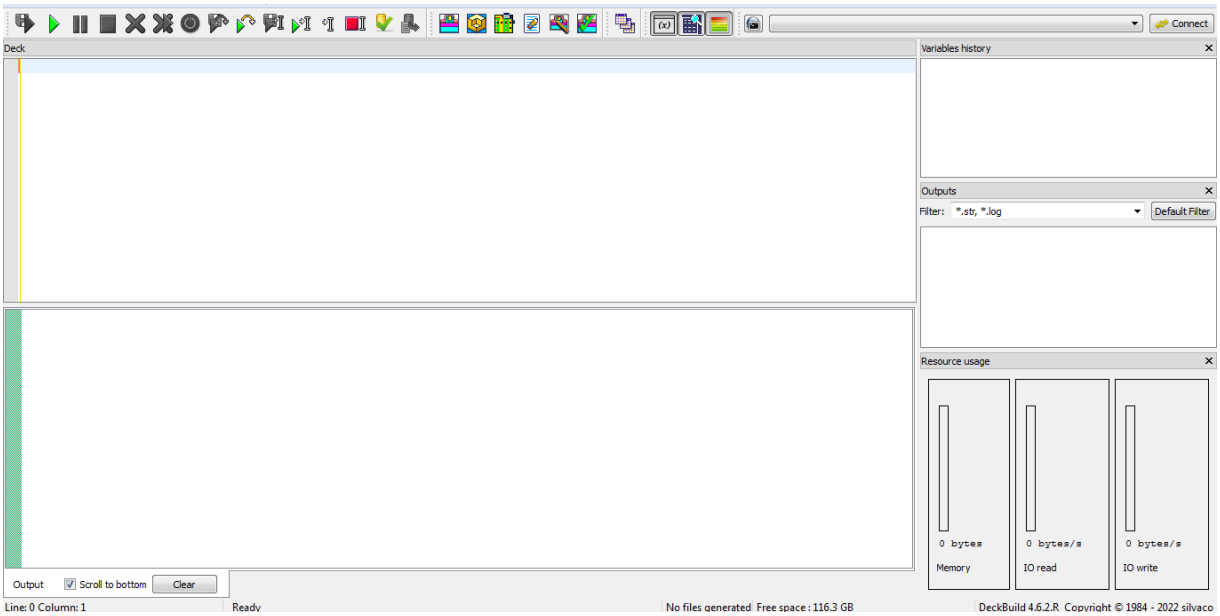

Figure III.9: DECKBUILD window.

The obtained results plotted and analyzed by another tool named TONYPLOT. TONYPLOT is a visualization tool which plots the results obtained from simulation.

The atlas input file contains a command line order. Each row consists of a number of statements that identifies the command and a set of parameters. The control groups are presented in Table III.1 [51].

Table III.1: Atlas Command Groups with the Primary Statements in each Group.

Group	*Statements*
Structure Specification	Mesh
	Regions
	Electrodes
	Doping
Materials Model Specification	Material
	Models
	Contacts
	Interface
Numerical Method Selection	Method
	Log
Solution Specification	Solve
	Lead and save
Results analysis	Extract
	Tonyplot

III.4.2.1. Structure Specification

The structure specification is done by defining the mesh, the region, the electrodes and the doping levels [91].

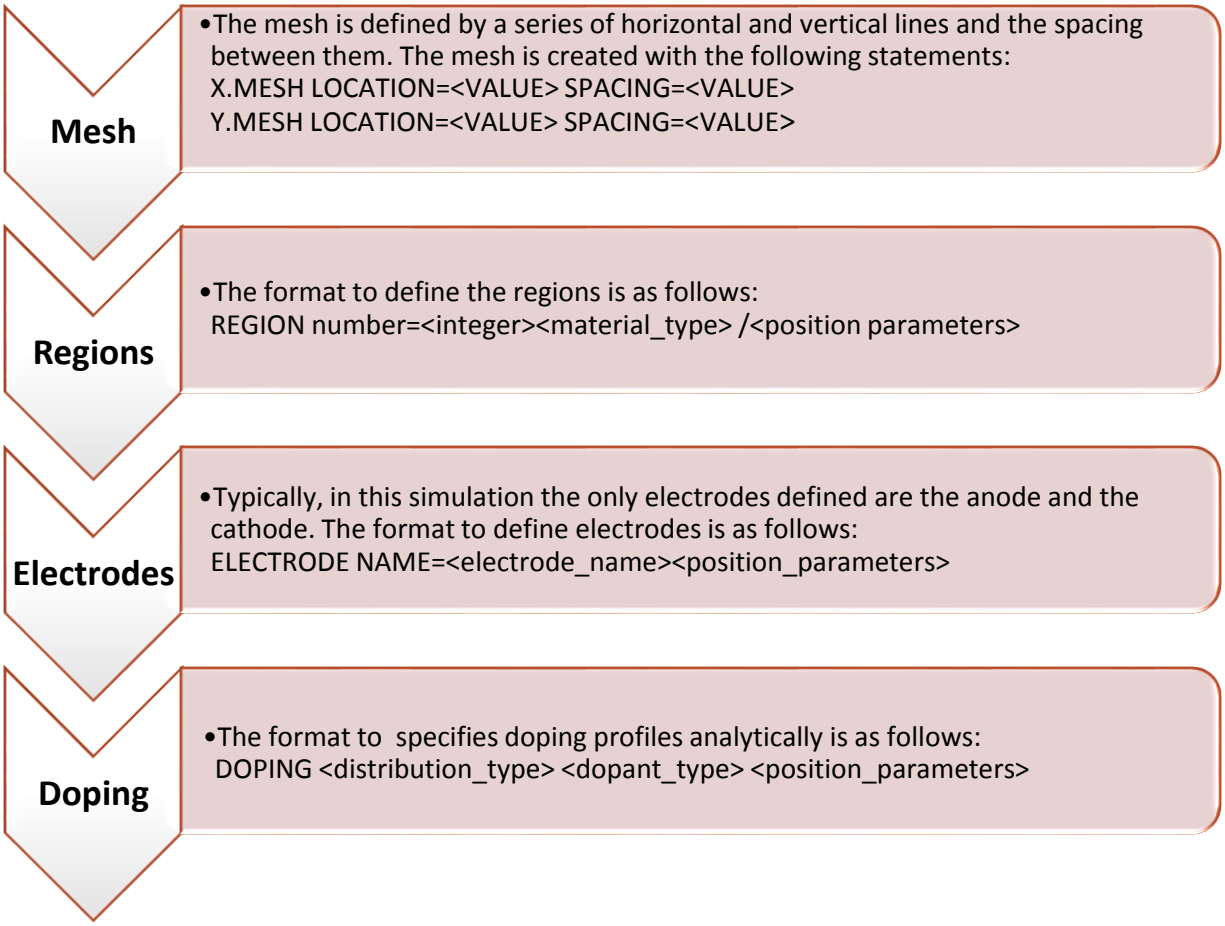

III.4.2.2. Materials Model Specification

After the structure specification, the materials model specification is the next step [91].

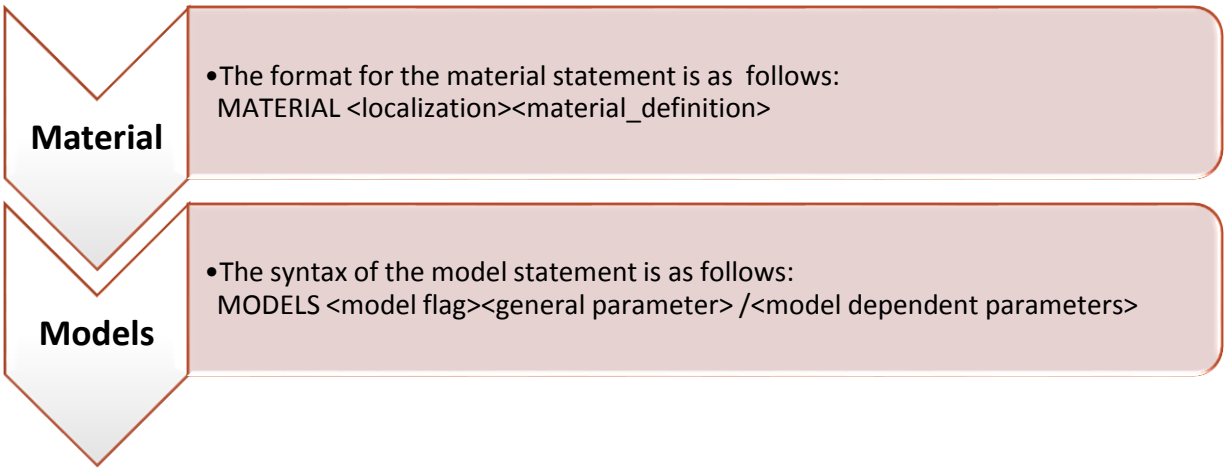

III.4.2.3. Numerical Method Selection

There are various numerical methods to calculate solutions to semiconductor device problems. There are three types of solution techniques used in SILVACO Atlas [91]:

GUMMEL (Decoupled):	NEWTON (Fully coupled):	BLOCK:
•which uses to solve each unknown in turn, keeping the other variables constant and repeating the process until a stable solution is achieved.	•can solves the total system of unknowns together.	•solves some equations fully coupled while others are decoupled. It is useful when lattice heating or energy balance equations are included.

III.4.2.4. Solution Specification

After completing the numerical method selection, the solution specification is next. Solution specification is broken down into log, solve, load, and save statements [91].

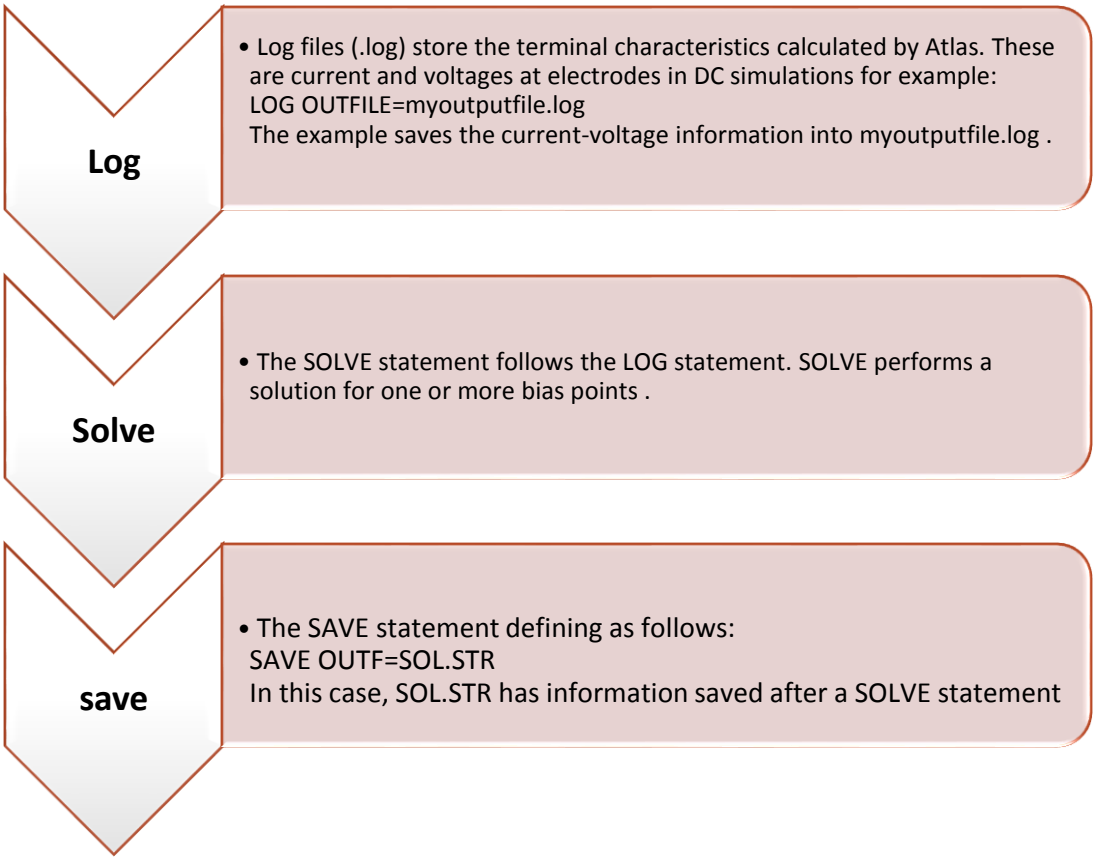

III.4.2.5. Data Extraction and Plotting

Once a solution has been found for a semiconductor device problem, the information can be displayed graphically with TonyPlot. Additionally, device parameters can be extracted with the EXTRACT statement [91].

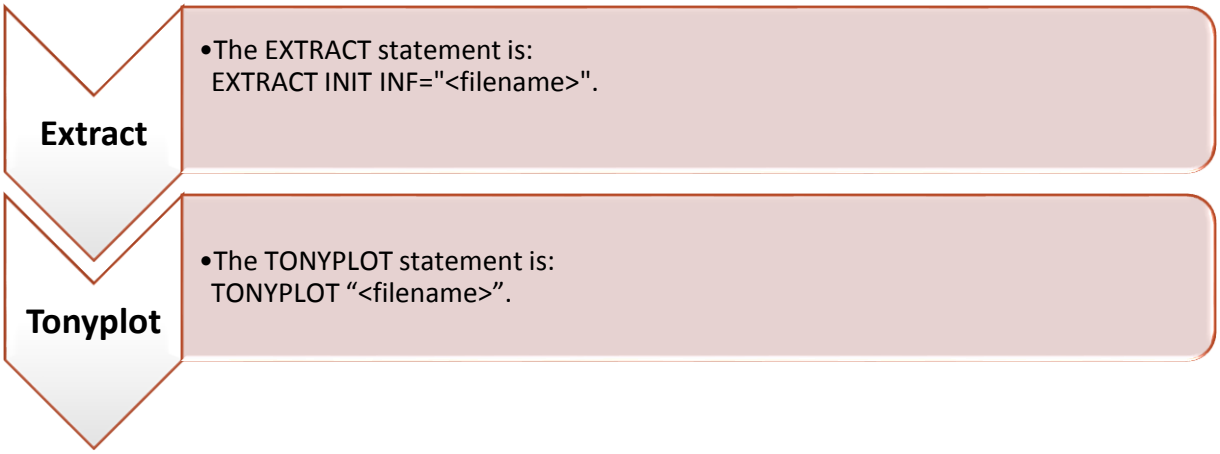

III.5. Analytical approach for the multilayer electrodes

The behavior of electromagnetic radiation through a multilayer system can be modelled by different methods [107]. The Matrix transfer method (TMM) is the most widely adopted, it exhibits a rapid and precise way to calculate the reflectivity and transmission spectra, band diagrams, emission spectra, the porosity and thickness gradients [108].

To study the transmittance (T), the reflectance (R) for a multilayer structure, and determine the optimal thicknesses of each layer of structure, with the TMM method, we consider a one-dimensional multilayer structure consisting of N+1 of thin films layered with different refractive index n_j and thicknesses d_j, on thick substrates exposed to non-orthogonal incidence light. Fig.III.10 shows this structure, where n0 is the refractive index of air, n_1 and n_2 are the layers refractive index, $d_1$andd_2 are the thicknesses of the respective layers[107, 109].

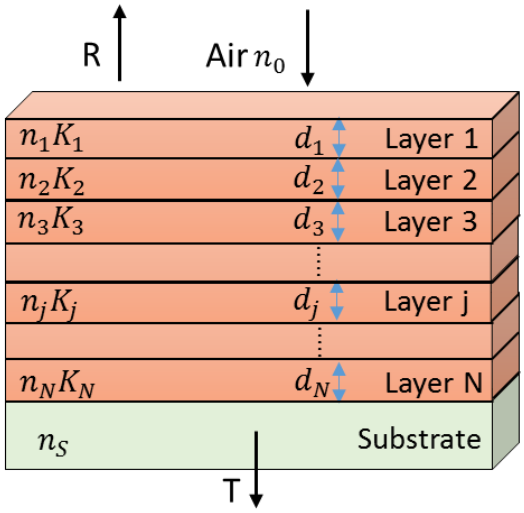

Figure III.10: multi-thin layers structure.

The characteristic matrix of multilayer system is given by the multiplication of each single layer matrixM_j. Firstly, we describe the characteristic matrix of one layer. The matrix connects

tangential components of the electric E(j) and magnetic H(j) fields at the layer boundaries j=0 and j=s, where j is the number of layers boundaries[107]:

$$\begin{bmatrix} E(j=0) \\ H(j=0) \end{bmatrix} = M_j \begin{bmatrix} E(j=s) \\ H(j=s) \end{bmatrix} \quad \textbf{III.21}$$

The matrix M_j is given by[107]:

$$M_j = \prod_{j=1}^{N} \begin{bmatrix} \cos\delta_j & (i\sin\delta_j)/n_j^{eff} \\ in_j^{eff}\sin\delta_j & \cos\delta_j \end{bmatrix} \quad \textbf{III.22}$$

Where δ_j is the phase thickness of the layer jth, given by[107]:

$$\delta_j = \frac{2\pi}{\lambda} n_j^{eff} d_j \quad \textbf{III.23}$$

With[107]:

$$n_j^{eff} = \begin{cases} n_j/\cos\theta_j \text{ for P-polarized wave} \\ n_j\cos\theta_j \text{ for S-polarized wave} \\ n_j \text{for normal light incidence} \end{cases} \quad \textbf{III.24}$$

Noted that θ_j the incident angle, n_j is the complex refractive index $n_j = n_j - ik_j$, of j^{th} layer for a given wavelength λ. Where n_j is the real part of refractive index while the imaginary part k_j denote the extinction coefficient, which relating to the absorption coefficient α_j according to[109]:

$$k_j = \alpha_j\lambda/4\pi \quad \textbf{III.25}$$

The optical admittance that n_s that relates the components E and H is[107]:

$$n_s = \frac{H(j=s)}{E(j=s)} \quad \textbf{III.26}$$

By analogy with equation that is before, Y represents the input optical admittance of the assembly, as a function of B and C, the normalized electric and magnetic fields, respectively, at the front interface [107]:

$$Y = \frac{H(j=0)}{E(j=0)} = \frac{C}{B} \qquad \textbf{III.27}$$

In the case of N layers, and as mentioned earlier, the characteristic matrix of the multilayer system is given by the production of the individual matrices as[107]:

$$\begin{bmatrix} B \\ C \end{bmatrix} = \left\{ \prod_{j=1}^{N} \begin{bmatrix} \cos\delta_j & (i\sin\delta_j)/n_j^{eff} \\ in_j^{eff}\sin\delta_j & \cos\delta_j \end{bmatrix} \right\} \begin{bmatrix} 1 \\ n_s \end{bmatrix} \qquad \textbf{III.28}$$

The optical parameters can be writing as a function of B and C as fellow[109]:

$$T = \frac{4n_0 R_e(n_s)}{(n_0 B + C)(n_0 B + C)^*} \qquad \textbf{III.29}$$

$$R = \left(\frac{n_0 B - C}{n_0 B + C}\right)\left(\frac{n_0 B - C}{n_0 B + C}\right)^* \qquad \textbf{III.30}$$

$$A = 1 - (T + R) \qquad \textbf{III.31}$$

Where T, R and A are the transmistion, reflection and absorption coefficients, respectivelly. By taking into consideration the imaginary part of refractive index, these equations aremore general than fresnel formulae.

The equivalent refractive index of whole structure can be calculated by:

$$n_{eq} = \left(\frac{1+\sqrt{R}}{1-\sqrt{R}}\right) \qquad \textbf{III.32}$$

Beer's law to find the absorption coefficient is given by

$$\alpha_j = \left(ln(100/T\%)\right)\Big/_{D} \qquad \textbf{III.33}$$

where

$$D = \sum_{j=1}^{N} d_j. \qquad \textbf{III.34}$$

By calculating the absorption coefficient from (III.33) and replacing in expression **III.25,** the extinction coefficient can be evaluated.

In this work, an optimization of Oxide/Metal/Oxide multilayer electrodes has been realized using a developed numerical simulation code with MATLAB software. It is necessary to optimize the layers thickness and the materials constituting the structure to obtain maximum transmittance.

CHAPTER IV:

RESULTS AND DISCUSSIONS.

IV.1 Introduction

Enhancing the power conversion efficiency in any type of solar cells is coupled to its parameters. These parameters are mainly: the open circuit voltage (V_{oc}) which is the potential level difference between the potential in the region where the free electrons are the majority and the region where the free holes are the majority. The second important parameter is the short circuit current density (J_{sc}). The magnitude of J_{sc} is determined by the number of photogenerated carriers created in the active layer upon illumination process and the efficiency of the charge separation across the photoactive layer. Therefore, J_{sc} can either be altered by modifying the structure leading to the lowest useful band gap or via altering the thickness of the active layer [39, 110]. The third parameter is the fill factor (FF) which is defined by the ratio between the maximum electrical power produced by the cell and the product $\boldsymbol{J_{sc} \times V_{oc}}$. FF is controlled by factors like shunt resistance, series resistance, and recombination/extraction rate of the charge in the solar cell, hence significantly influences the cell quality and fully related to V_{oc}, J_{sc} and the morphology of active layer [39, 110]. The last parameter is the performance efficiency (η), and is defined by the product of $V_{oc} \times J_{sc} \times FF$[110]. This is the more important parameter since it presents the ratio between the cell electrical power and the incident light power.

In this chapter, the results and discussion of a one-dimensional modeling of conventional and inverted organic solar cells are presented. The numerical simulation was performed using GPVDM software in the study of conventional and inverted organic solar cells. Then the multi-thin layers electrodes optimization is carried out and applied in the optimized standard and inverted OSC. A similar study was investigated using SILVACO ATLAS, while the optimization of multi-thin layers electrodes was performed using MATLAB and then applied in optimized standard and inverted OSC. Therefore, this work is focused on designing an organic based solar cell and extracting its output parameters. For both types of solar cells, the conventional and inverted structures are compared. The simulation is based on studying the effect of layers thicknesses, changing electron and hole transport layers (ETL and HTL, respectively).

The numerical simulation is carried out under AM1.5 spectrum at 300 °K. The calculated current density-voltage characteristics (J-V) are used to extract the solar cell electrical outputs which are the short-circuit current density (J_{sc}), the open circuit voltage (V_{oc}) , the fill factor (FF), and the efficiency (η).

IV.1.1. Study of conventional and inverted P3HT: PCBM organic solar cell

Bulk hetero-junction structure consists of an interpenetrating network of n-type material (usually conjugated polymers, oligomers or conjugated pigments) and p-type materials (frequently fullerene derivatives material)[111, 112]. Based on this idea, conventional (OSCs) with poly (3-hexylthiophene-2,5-diyl):(6, 6)-phenyl C61 butyric acid methyl ester (P3HT:PCBM) blend are the most recent used in polymer solar cells[113, 114].

Bulk heterojunction solar cells (BHJSCs) are built on a transparent substrate coated with a transparent conductive electrode material, usually indium tin oxide (ITO)[112]. There are two types of BHJSC conception: conventional (standard) structure and inverted structure[112, 114]. In the so-called standard structure, ITO substrate is the anode and is coated with a hole transport layer (HTL) often a doped conjugated polymer thin film such as PEDOT:PSS (poly(3,4-ethylenedioxythiophene) poly(styrenesulfonate)) or a thin oxide layer such Nickel oxide (NiO), Cuprous oxide (Cu_2O), Molybdenum Oxide (MoO_3) or Vanadium Oxide (V_2O_5)[114]. On top of HTL, is deposited a BHJ layer (basic region for light absorption) formed by a blend of n-type and p-type material (P3HT:PCBM). This layer is followed by an electron transport layer (ETL) often formed by a conductor oxide such as Zinc Oxide (ZnO)or Titanium Oxide (TiO_2)[24] and finally the cathode. Usually for this solar cell type, the concept of top and bottom electrode is related to the substrate (which is the bottom of the cell). Consequently for the conventional structure, the cathode is the top electrode and is formed by a low work function metal (calcium, barium or aluminum)[112, 115].However, this structure suffers a high acidity of PEDOT:PSS interfacial layer and a low air stability of the low-work-function metal cathode. To remedy these drawbacks, the inverted organic solar cell (IOSC) structure is introduced[116, 117]. In comparison to the BHJ of the conventional structure the active layer of the IOSC is characterized by a higher concentration of PCBM compound near the ITO side, while the P3HT compound is more concentrated at the metal electrode side. This is to promote charge collection and transport[118]. In addition, in the inverted design, the cathode is the bottom ITO substrate coated by an ETL. While an HTL is used on the top of the active layer, followed by an air stable high work function electrode material such as silver or gold[112, 119, 120].

Another issue in organic materials is the low absorption, mainly in a narrow range in the visible spectrum[121, 122]. To solve this problem, two solutions were suggested. The first is the increase of the thickness of the active polymer layer to absorb more light, but this is possible only for a polymer

with relatively high mobility. In case of a lower mobility, the thickness increase rises the internal series resistance and, thereby, reduce the fill factor[122, 123]. The second approach is to keep the active polymer layer thickness and change the spatial distribution of the internal optical electric field by inserting an optical spacer between the active layer and the top electrode[123].The choice of the suitable optical spacer depends on the fact that it must be a good electron-transport material (ETM)and transparent. Thus, the use of an optical spacer provides an enhancement of the photocurrent while keeping the thickness fixed[122].

Most of the recent work is focused on OSC or IOSC separately, and there are a few comparison performances reports. Therefore, the aim of this work is to investigate the difference between OSC and IOSC electrical characteristics, the effect of active layer thickness on their electrical outputs, testing several of ETL and HTL materials to choose between.

IV.1.1.1. Devices structure

Using GPVDM software, the study of P3HT: PCBM organic solar cell is investigated in this part. The OSC and IOSC studied in this work are presented in Figure IV.1 (a) and (b) specifying the materials and thicknesses of the different layers. The conventional OSC has a structure: substrate/ITO/PEDOT:PSS (HTL)/P3HT:PCBM (blend p-n active layer)/TiO_x (ETL)/Al. The IOSC structure is: substrate/ITO/TiO_x (ETL)/P3HT:PCBM (blend p-n active layer)/PEDOT:PSS (HTL)/Ag.

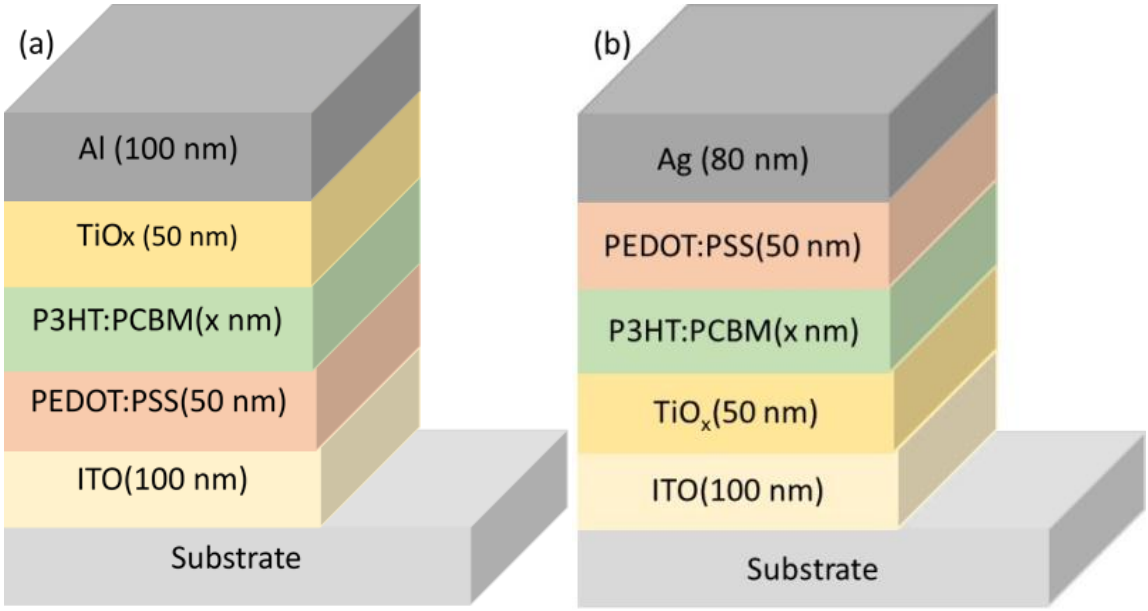

Figure IV.1: The initial structure of the bulk organic bulk heterojunction solar cell: (a) conventional (OSC)and (b) inverted (IOSC).

Both OSC and IOSC are illuminated on the side of the transparent ITO substrate. Electron and hole collection, by their respective electrode, is assured by ETL and HTL regions respectively.

In this section, three effects are presented and compared between the two cells, OSC and IOSC: the thickness of the different layers, the best performing ETL and HTL materials are deduced. The input parameters of all materials used in this work are in the software database. The DOS parameters are given in Table IV.1[98].

Table IV.1: The material and the density of states (DOS) used parameters.

Parameter	Symbol	Value	Unit
Electron trap density	N_e^{exp}	3.8×10^{26}	$m^{-3}eV^{-1}$
Hole trap density	N_h^{exp}	1.45×10^{25}	$m^{-3}eV^{-1}$
Electron tail slope	N_e^U	40×10^{-3}	eV
Hole tail slope	N_h^U	60×10^{-3}	eV

Electron mobility	μ_{n0}	2.48×10^{-7}	$m^2V^{-1}s^{-1}$
Hole mobility	μ_{p0}	2.48×10^{-7}	$m^2V^{-1}s^{-1}$
Relative permittivity	ε_r	3.8	au
Effective density of free electron states	N_c	1.28×10^{27}	m^{-3}
Effective density of free hole states	N_v	2.86×10^{25}	m^{-3}
Affinity	χ_i	3.8	eV
Energy gap	E_g	1.1	eV

IV.1.1.2. Effect of thicknesses: comparison between OSC and IOSC

IV.1.1.2.1. The active layer thickness

Layers stacked sequentially on top of each other in the BHJ device, and the optical events such as reflections at interfaces between layers and their interferences create a complex enhancement task with respect to the thickness of the active layer [124]. Therefore, the study of the active layer thickness is very important since the thickness impacts the light absorption and thereby the generation of excitons inside the active layer [124].

In order to perform a comparative study and to optimize the performance of each structure of BHJ, the thickness of the active layer has been varied from 100 nm to 500nm. Figure IV.2 shows the J-V characteristics obtained for OSC and IOSC.

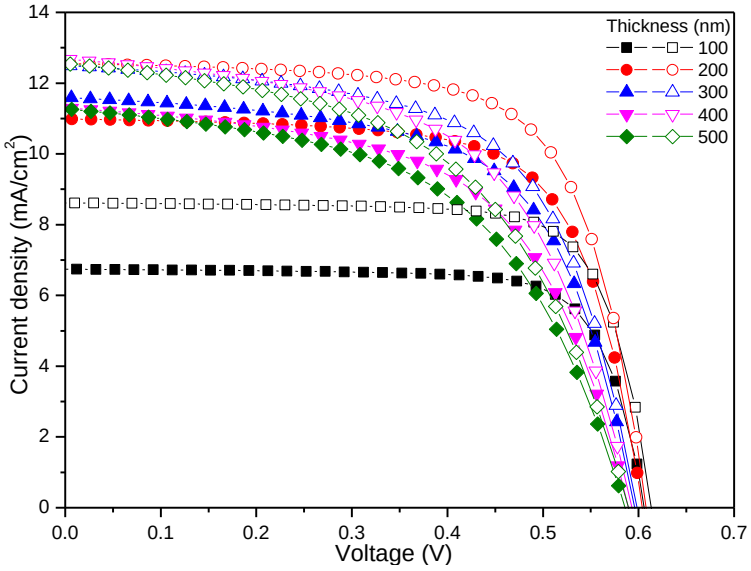

Figure IV.2: J-V characteristic for different active layer thicknesses: OSC (solid symbols), IOSC (hollow symbols).

Figure IV.3 presents the extracted electrical outputs (OSC: solid symbols and IOSC: hollow symbols) from the J-V curves (Figure IV.2) for different active layer thicknesses. To calculate the relative change in a variable A, use the formula $\Delta A\ (\%) = \frac{A-A_0}{A_0} \times 100$ where A_0 is the initial value of the variable A.

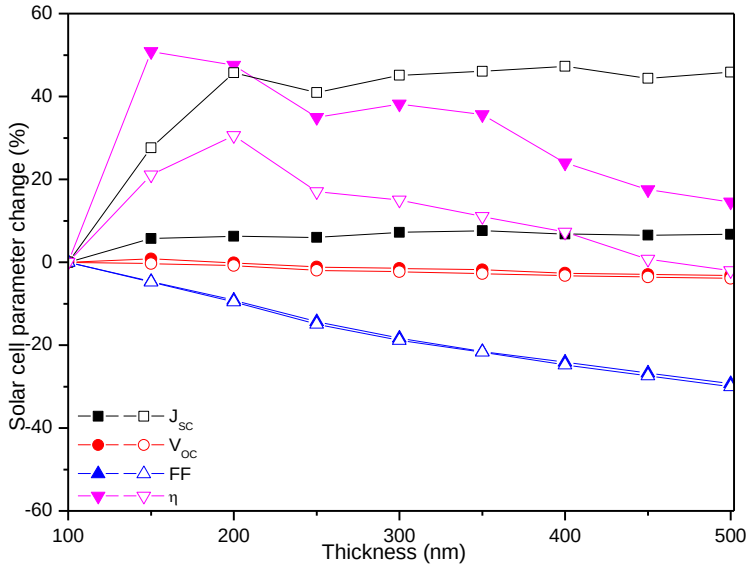

Figure IV.3: The percentage change in the extracted electrical outputs (OSC: solid symbols and IOSC: hollow symbols) from the J-V curves (Figure IV.2) with active layer thickness increase.

It is observed that the J–V characteristics are very sensitive to the active layer thickness variation, as mentioned before, J_{sc} is highly related to the absorption in the active layer.

From Figure IV.3, it is observed that J_{sc} , η and FF present significant variations with the active layer thickness increase for both OSC and IOSC, while V_{oc} seems to be less sensitive. The carrier photogeneration and transport expressed by J_{sc} are controlled by the absorption and the diffusion length. In the OSC the best thickness obtained for J_{sc} is around 350 nm while in IOSC a saturation of the optimal J_{sc} is observed near 400 nm. The presence of a maximum in the current curve at a certain thickness means that for lower thicknesses, the absorption is not complete. While greater thicknesses exceed the exciton average pathway and reduce the internal field that ensures exciton dissociation and hence the carrier collection efficiency will be smaller. Smaller thicknesses, 150 nm in OSC and 200 nm in IOSC, give optimal efficiencies which are, respectively, 4.66% and 5.21%. FF decreases significantly with increasing active layer thickness which is due to the series resistance effect while V_{oc} decreases slightly from 0.61 to 0.59 V in both devices.

IV.1.1.2.2. Effect of ETL thickness

The importance of ETL and HTL, known also as buffer layers, is the possibility to act as exciton blocking layers (EBL) and to enhance carrier extraction/collection in the device [125]. In this section, a study of ETL thickness effect on the performance of OSC and IOSC is undertaken. The previously obtained optimum thickness of P3HT:PCBM layer is fixed at 150 nm for OSC and 200 nm for IOSC. The first chosen ETL material is TiO_x and its thickness is varied from 10 nm to 60 nm. Figure IV.4 shows the obtained J-V characteristics.

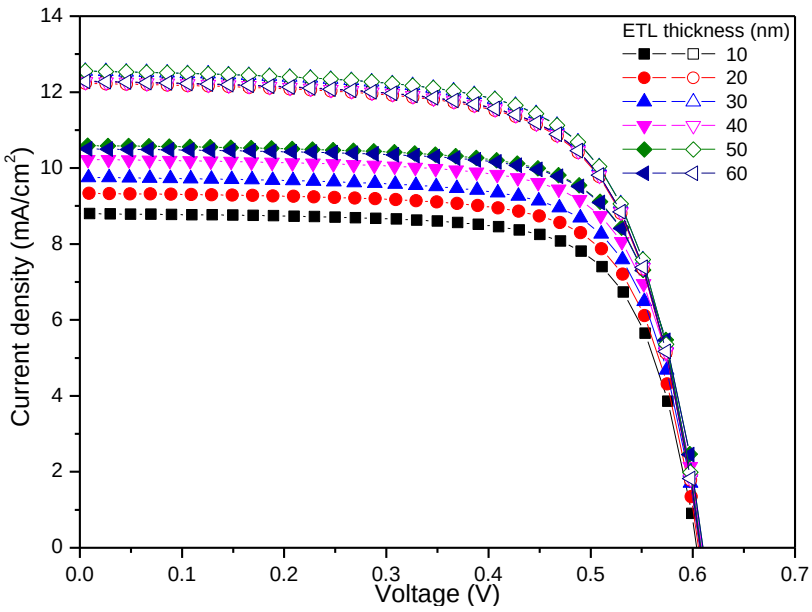

Figure IV.4: J-V characteristic obtained by varying the ETL thickness: OSC (solid symbols), IOSC (hollow symbols).

Figure IV.5 presents the extracted electrical outputs. There is some similarity between the variations of J_{sc} and PCE in either OSC or IOSC. In addition, the increase of the ETL thickness has an effect only in OSC. J_{sc} and PCE greatly increase from 8.80 to 10.51 mA/cm^2 and from 3.83 to 4.66% respectively. However, in IOSC, J_{sc} and PCE are higher but without appreciable variations with ETL thickness increase. In addition, V_{oc} and FF exhibit very slight variations in OSC and IOSC although FF of the first is a bit better.

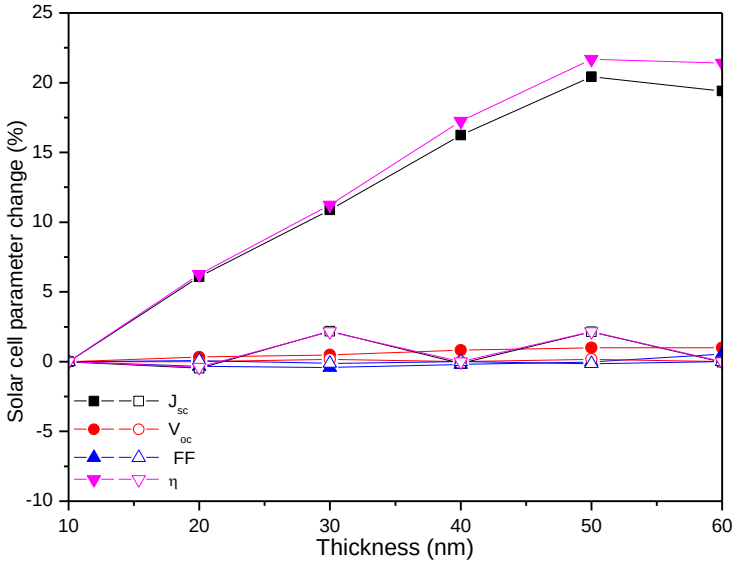

Figure IV.5: The percentage change in the extracted electrical outputs (OSC: solid symbols and IOSC: hollow symbols) from the J-V curves (Figure IV.4) with the ETL thickness increase.

Similar results have been reported concerning the greater sensitivity of OSC to ETL thickness [121, 126, 127]. It is worth to mention that this is may be due to the fact that: in OSC, ETL is at the top immediately below the cathode and illumination is from the bottom. ETL affects OSC more than IOSC because, the insertion of the TiO_x which is an optical spacer for OSC between the top Al metal electrode and the BHJ layer enhance the photocurrent, by optimizing the absorption of light inside the photoactive layer through enhancing the spatial distribution of light by the back reflection [122, 128].

IV.1.1.2.3. Effect of HTL thickness

Now, the HTL thickness effect is considered. ETL and active layer thicknesses are fixed in OSC at 50 and 150 nm while at 30 and 200 nm in IOSC. The chosen thicknesses correspond to the best efficiencies. The chosen HTL material PEDOT:PSS (different materials will be considered later) and the thickness of the layer is varied from 10 to 60 nm in both OSC and IOSC. The resulting J–V characteristics are shown in Figure IV.6, the extracted electrical outputs are plotted in Figure IV.7.

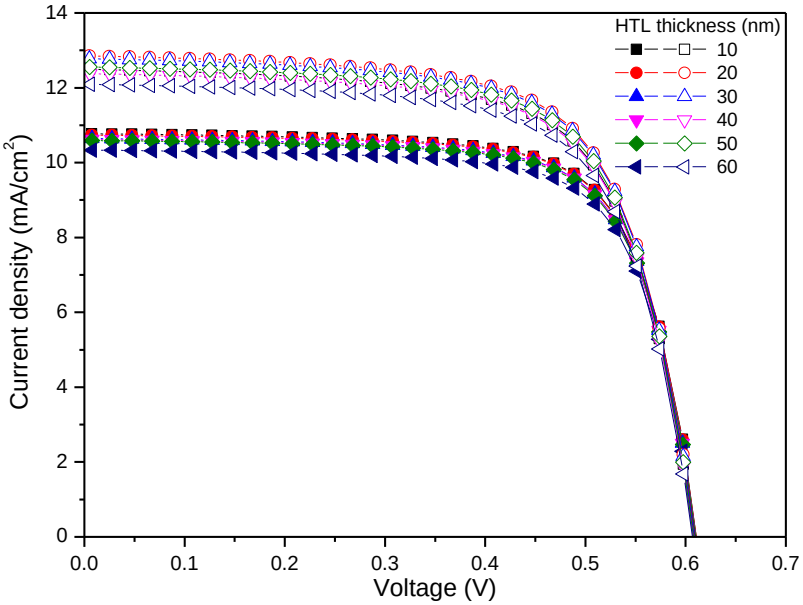

Figure IV.6: J-V characteristics obtained by varying the HTL thickness: (solid symbols) OSC, (hollow symbols) IOSC.

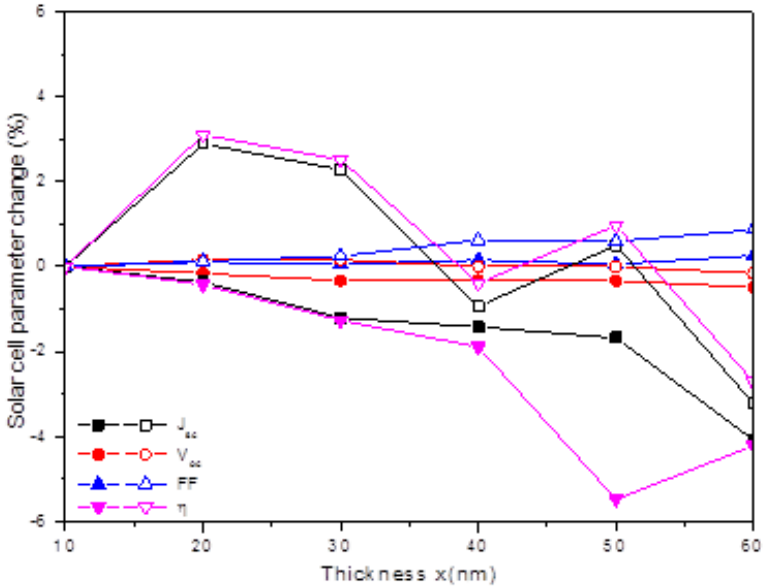

Figure IV.7: The percentage change in the extracted electrical outputs (OSC: solid symbols and IOSC: hollow symbols) from the J-V curves (FigureIV.6) with the HTL thickness increase.

The best OSC and IOSC performances are obtained for 10 and 20 nm HTL thicknesses respectively. Furthermore, in OSC, as the HTL thickness increases, slight decrease is observed in J_{sc} and PCE, in agreement with [126]. However, in IOSC and similarly to the ETL thickness effect, there is no evident relation between the increase of HTL thickness and the variations of J_{sc} and PCE that present a slight decrease from the maximum. Overall, the effect of the HTL thickness is minor and more exactly nonexistent for FF and V_{oc} in both solar cells and which can be explained by the low mobility of holes (majority carriers) in this region.

IV.1.1.3. Effect of ETL material

In this section, a number of materials used as ETL in organic solar cells are proposed in order to determine which one gives better performance. A good material for ETL between the Al cathode and the active layer, for the OSC, and between ITO cathode and the active layer, for the IOSC should fulfill some crucial conditions. Mainly it should be suitable for electron conduction and acts as a hole-blocking layer to facilitates only electron transport to the cathode and providing a barrier to prevent the flow of holes toward cathode, hence, delays the electron-hole pair recombination near the cathode [122, 129].

In this study the proposed materials are:TiO_x, ZnO, and PCBM. Figure IV.8 presents the obtained J-V characteristics, and the extracted output parameters are given in Table IV.2.

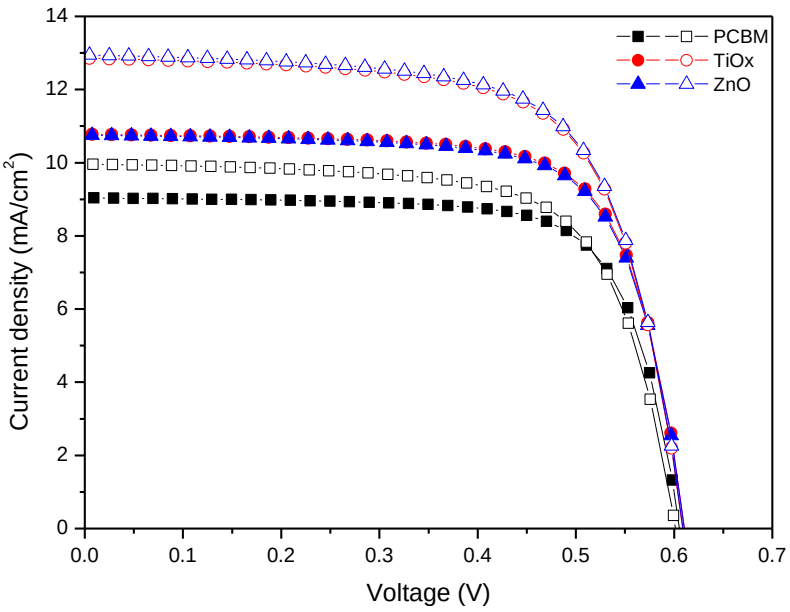

Figure IV.8: The J-V characteristics obtained for three different ETL materials: (solid symbols) OSC, (hollow symbols) IOSC.

It is clear that TiO_x and ZnO are the most suitable ETL materials for OSC and IOSC, respectively. To give an explanation to this, the energy level alignment of the active layer, cathode, anode and the proposed ETL materials are presented in Figure IV.9. It is clear that ZnO with its larger energy band gap (better light transmission) and identical affinity to that of ITO is more suitable in this case. However, for OSC where the ETL is located at the back with simple metals (Al) as cathode, TiO_x is more adequate for the electron injection and collection.

Table IV.2: Effect of different ETL materials on electrical outputs of OSC and IOSC.

Parameters		$J_{sc}(mA/cm^2)$	$V_{oc}(V)$	FF (%)	η(%)
OSC	**TiO_x**	**10.78**	**0.61**	**72.13**	**4.75**
	ZnO	10.75	0.61	71.83	4.71
	PCBM	9.04	0.61	73.01	3.40
IOSC	TiO_x	12.86	0.61	67.94	5.32
	ZnO	**12.95**	**0.61**	**67.91**	**5.35**

PCBM	9.96	0.61	68.78	4.12

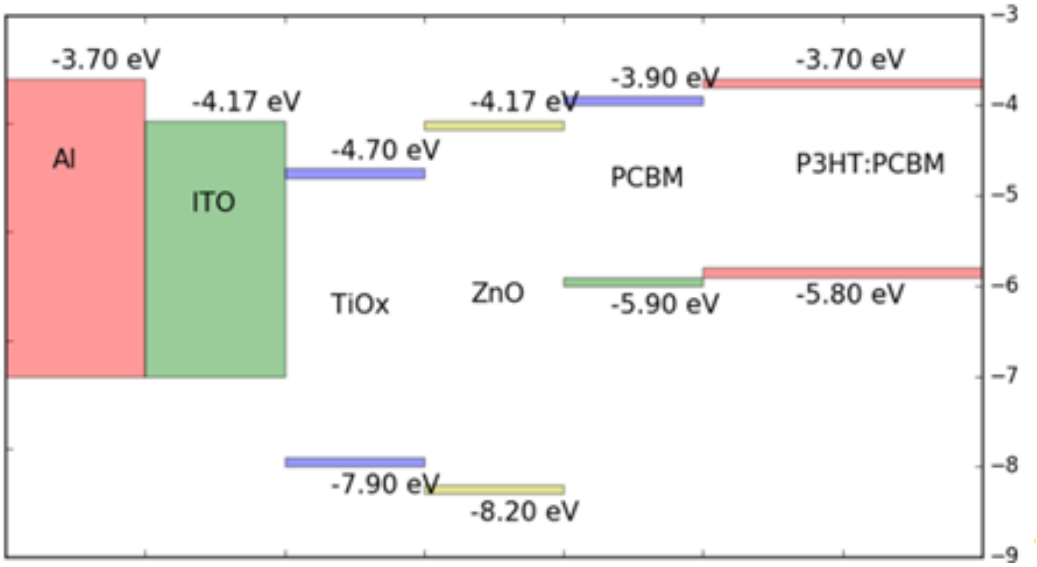

Figure IV.9: Band level alignment of the proposed ETL material located between the Al and the active P3HT: PCBM layer in OSC and between the active layer and ITO in IOSC.

IV.1.1.4. Effect of HTL material

In this section, the proposed materials as HTL are: PEDOT: PSS (Poly(3,4-ethylenedioxythiophene)-poly (styrenesulfonate)), P3HT (poly(3 hexylthiophène-2,5-diyl)) and Cu_2O. Figure IV.10 shows the J-V characteristics of OSC and IOSC and the extracted electrical outputs are summarized in Table IV.3.

The energy level alignment of the active layer, cathode, anode and the proposed HTL materials are presented in Figure IV.11. For the OSC, the best performance is achieved for Cu_2O HTM, with an efficiency reaches to 4.77%. This is due to the high band gap energy of Cu_2O which located at the side of the illuminated substrate ITO and hence ensures a good transmission. In addition, a higher energy barrier between the active layer LUMO level and the HTL conduction band as well as a better matching between the HOMO level of the active layer and the HTL valence band, result in an enhanced hole collection and electron blocking at the interface.

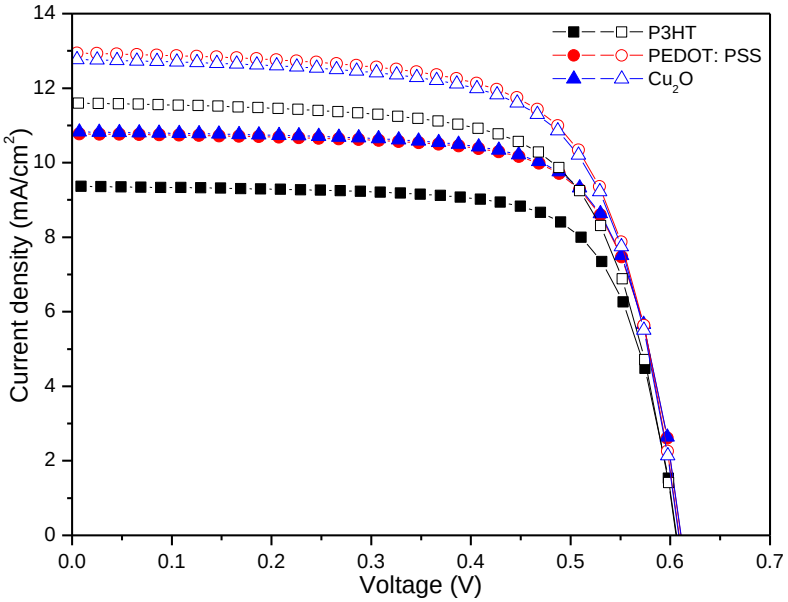

Figure IV.10: The J-V characteristic obtained for three different HTL materials: (solid symbols) OSC, (hollow symbols) IOSC.

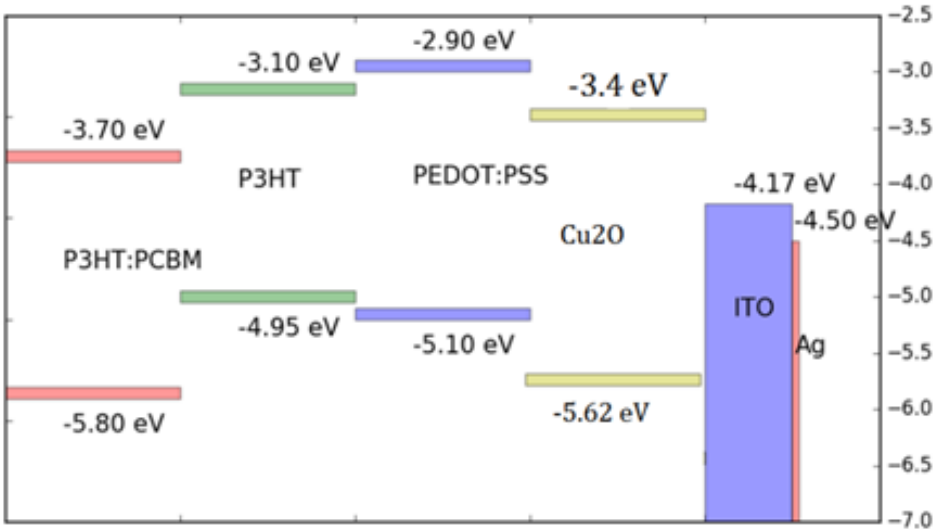

Figure IV.11: Band level alignment of the three suggested HTL material located between the active layer and the ITO in OSC and between the active layer and Ag in IOSC.

Whilst for the IOSC, PEDOT:PSS gives an optimum efficiency of 5.35%. This is due to the high work function of the PEDOT:PSS (a good matching of commonly used donor polymers with

the HOMO level), good transparency in the visible region, high electrical conductivity and easier transport of holes rather than electrons, as reported in [130].

Table IV.3: Effect of different HTL materials on electrical outputs of OSC and IOSC. The bold values are the best performances.

Parameters		$J_{sc}(mA/cm^2)$	$V_{oc}(V)$	FF (%)	η(%)
OSC	PEDOT:PSS	10.78	0.61	72.13	4.75
	P3HT	9.37	0.61	72.57	4.12
	Cu_2O	**10.83**	**0.61**	**72.09**	**4.77**
IOSC	**PEDOT:PSS**	**12.95**	**0.61**	**67.91**	**5.35**
	P3HT	11.60	0.61	68.55	4.82
	Cu_2O	12.77	0.61	68.06	5.29

The band level energy of optimized OSC and IOSC structure are illustrated in Figure IV.12 and Figure IV.13

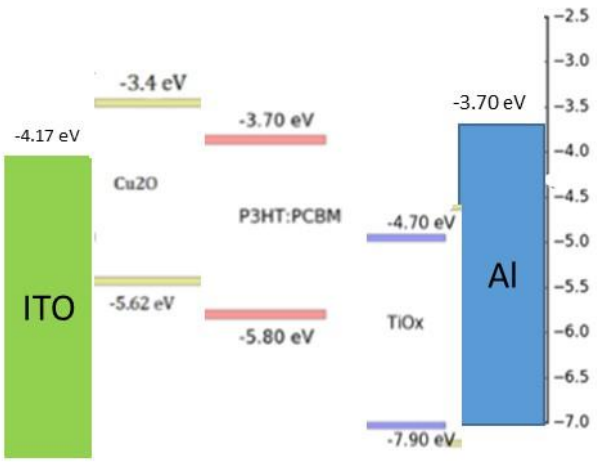

Figure IV.12: Band level energy of optimized OSC.

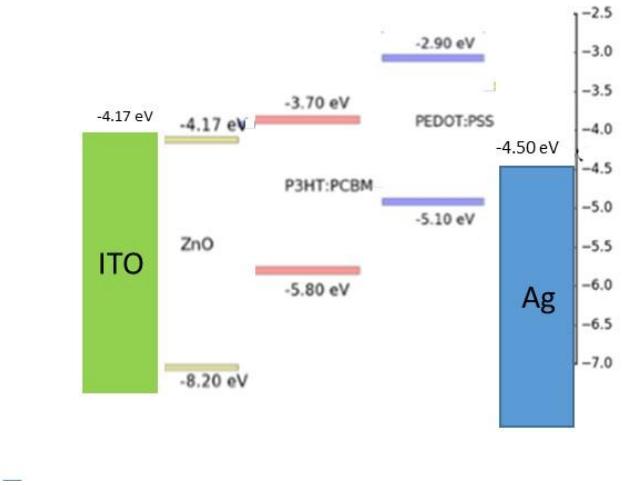

Figure IV.13: Band level energy of optimized IOSC.

IV.1.1.5. Investigation of multi-layer electrode

In the previous sections the substrate ITO through which the light is transmitted was used as bottom electrode (anode for OSC, cathode for IOSC) while the top electrode was formed by simple metal; Al as cathode for OSC and Ag as anode for IOSC. Many other works suggested that the use of multi-layer electrodes instead of the mono-layer electrode and its ETL (or HTL) enhances the cell performances [16].

In this part, multi-layer electrodes, at the bottom facing light, while keeping the top electrode metal (Al for OSC and Ag for IOSC). Two types of multi-layer electrode are proposed: TCO/metal/TCO and TCO/TiOx/ZnO for both OSC and IOSC, in order to find the best multi-layer that gives the cells the best performance.

IV.1.1.5.1. TCO/metal/TCO bottom electrode

TCO/metal/TCO instead of ITO is tested to improve the performance of the studied solar cells. HTL for OSC and ETL for IOSC are then omitted. Finding suitable metal and transparent conductive oxide (TCO) will be studied. Ag, Au, Cu, Al were tested as an intermediate metallic layer and the best choice was the Ag since it has an excellent conductivity [16] and offers the

possibility to form a thin enough film to provide sufficient transmittance. In addition, the real parts in its refractive index (n ~ 0.05-i2.90) is the lowest compared to other metals, which gives the best reduction in light absorption [3, 15]. Consequently, Ag thickness in the ITO/Ag/ITO will have an important impact on the transmittance and the sheet resistance.

First, we use ITO as TCO in the multi-layer bottom electrode TCO/Ag/TCO. The thickness of both ITO layers is fixed at 40 nm while the Ag thickness will be varied from 4 to 14 nm in both OSC and IOSC. The obtained J-V characteristics are plotted in Figure IV.14. Figure IV.15 shows the extracted outputs for OSC and IOSC.

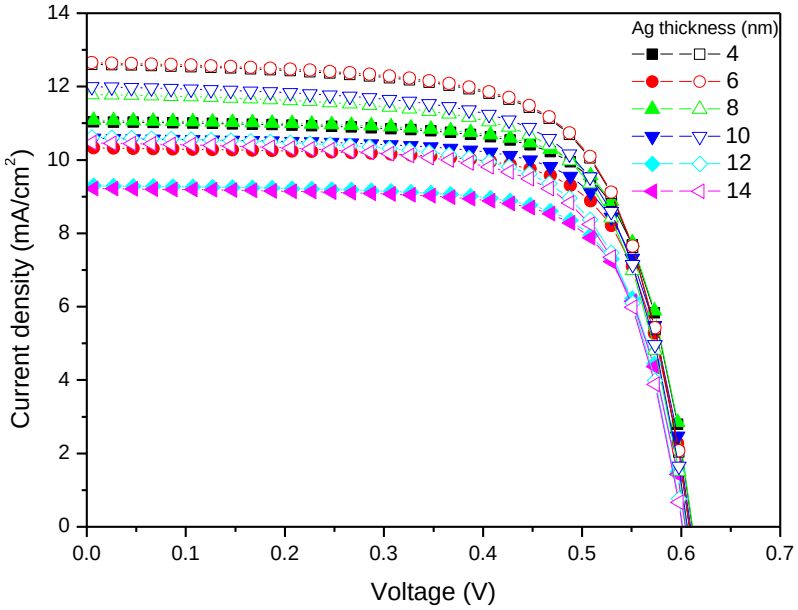

Figure IV.14: Effect of the Ag thickness in ITO/Ag/ITO bottom contact for: (solid symbols) OSC, (hollow symbols) IOSC.

For Ag thickness of 6 nm, OSC and IOSC have an optimum performance of 4.87% and 5.10% respectively, for the. Efficiency shows an abrupt decrease, if metal film thickness increases further. This is explained by the Ag layer transmittance decrease. However, 4 nm thickness cannot be achieved experimentally [13, 76, 131]. Consequently, the Ag optimum value of 6 nm is fixed, while the oxide layer material is varied with maintaining its thickness at 40nm. The proposed TCO are: ITO, FTO, AZO and TiOx.

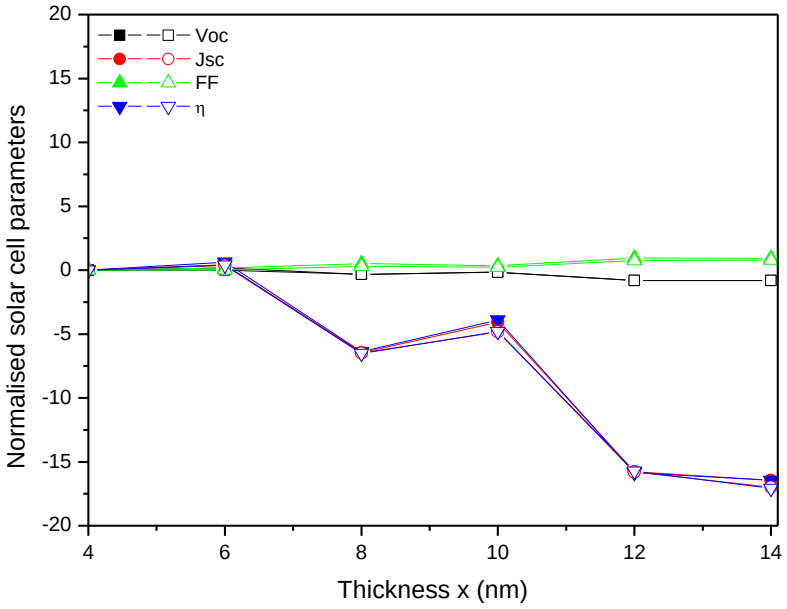

Figure IV.15: Effect of the Ag thickness in ITO/Ag/ITO bottom contact on the extracted electrical outputs in OSC and IOSC: (solid symbols) OSC, (hollow symbols) IOSC.

The obtained J-V characteristics of OSC and IOSC are presented in Figure IV.16 and the extracted outputs are summarized in Table IV.4.

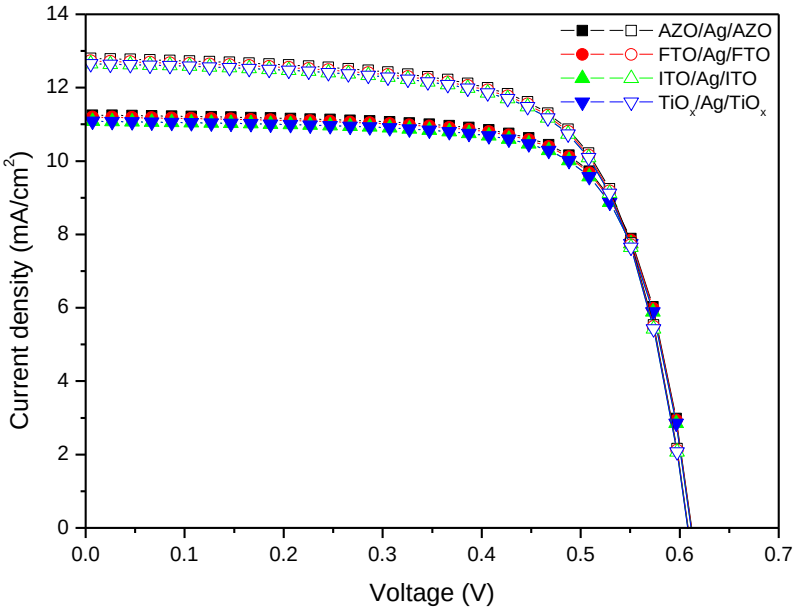

Figure IV.16: Effect of different TCO materials in bottom TCO/Ag/TCO electrode on J-V characteristics for: (solid symbols) OSC, (hollow symbols) IOSC.

Table IV.4: Effect of different TCO in (TCO/Ag/TCO) multi-layers electrode on OSC and IOSC outputs.

Structure	Multilayers electrode	$J_{sc}(mA/cm^2)$	$V_{oc}(V)$	FF (%)	η(%)
OSC	ITO/Ag/ITO	11.09	**0.61**	72.08	4.89
	FTO/Ag/FTO	11.20	0.61	72.03	4.93
	AZO/Ag/AZO	**11.25**	0.61	**72.02**	**4.96**
	TiO_x/Ag/TiO_x	11.09	0.61	72.08	4.89
IOSC	ITO/Ag/ITO	12.66	0.61	67.99	5.23
	FTO/Ag/FTO	12.73	0.61	67.98	5.26
	AZO/Ag/AZO	**12.80**	0.61	**67.95**	**5.29**
	TiO_x/Ag/TiO_x	12.66	0.61	67.99	5.23

The different TCO layers have comparable PCE (~4.9% in OSC and ~5.2% in IOSC). A slight improvement is noticed for AZO (Al doped ZnO) in OSC with an optimal efficiency of 4.96 % and for IOSC with 5.29%. Figure IV.17 presents the band banding in the structure and it seems that a good alignment of the active layer HOMO level and the AZO valence band in OSC as well as a better matching between the active layer LUMO level and the AZO conduction band of in IOSC.

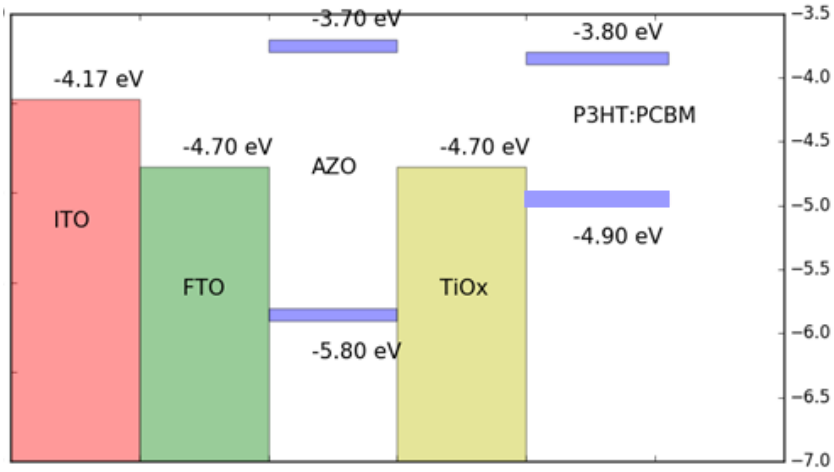

Figure IV.17: Band level alignment of the different TCO materials suggested for the bottom multi-layer electrode.

In summary, it can be said that the TCO type does not have a significant impact on the performance of both OSC and IOSC.

IV.1.1.5.2. TCO/TiO_x/ZnO electrode

In this part, tri-layer oxides electrode (oxide/TiO_x/ZnO is suggested). First, FTO is used as the oxide and its thickness is varied from 40 nm to 140 nm, while the thicknesses of TiO_x and ZnO layers are fixed at 10 nm. Figure IV.18 shows the J-V characteristics as a function of FTO thickness for both OSC and IOSC. Figure IV.19 presents the extracted outputs.

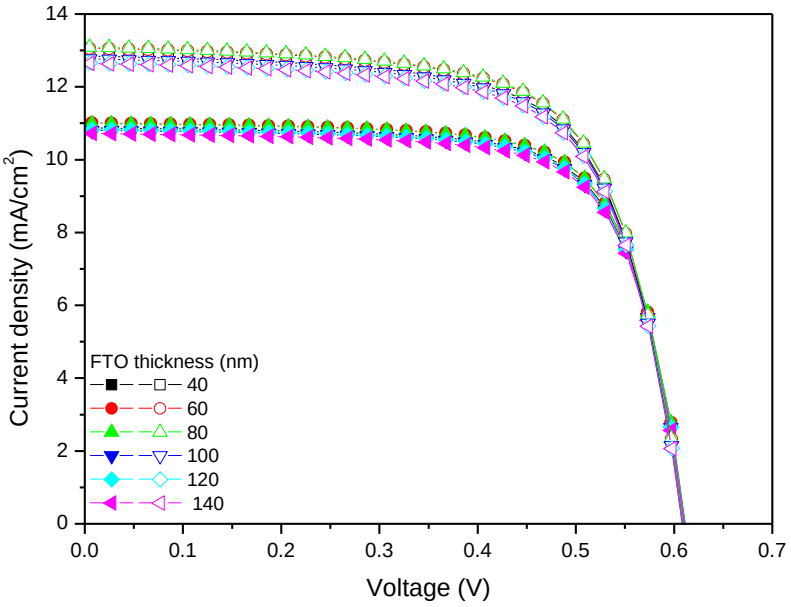

Figure IV.18: Effect of the FTO thickness in FTO/TiO_x/ZnO as bottom multi-layer electrode on the J-V curves for: (solid symbols) OSC, (hollow symbols) IOSC.

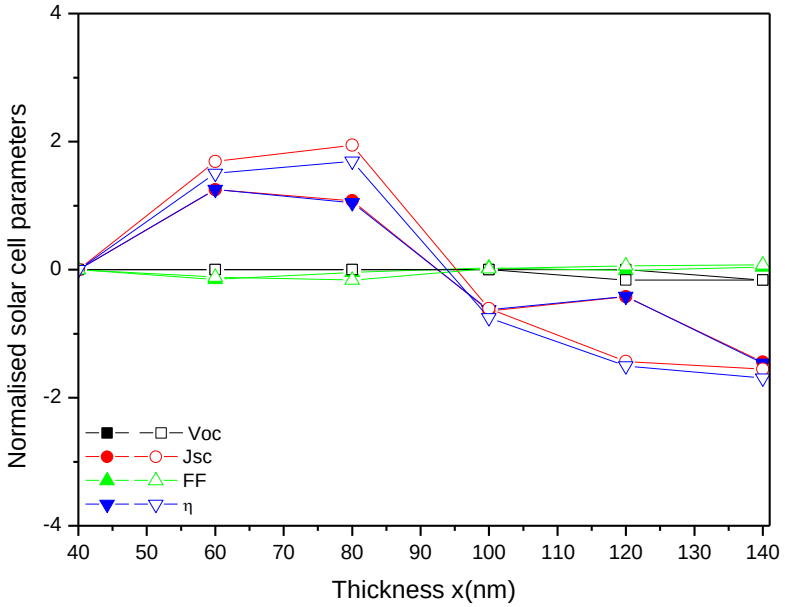

Figure IV.19: Effect of the FTO thickness in FTO/TiO_x/ZnO bottom multi-layer electrode on the extracted electrical outputs of: (solid symbols) OSC, (hollow symbols) IOSC.

The performance of both OSC and IOSC seems to be slightly better at low thicknesses of FTO layer because it is located on the bottom where is the light incidence takes place; This layer should be thin enough to minimize its contribution to light absorption. The optimum thicknesses (60 and 80 nm for OSC and IOSC respectively) are fixed and the FTO layer material is replaced by other alternative oxides including AZO, ITO and ZnO.

The obtained J-V characteristics are presented in Figure IV.20 for OSC and IOSC and figures of merit in Table IV.5.

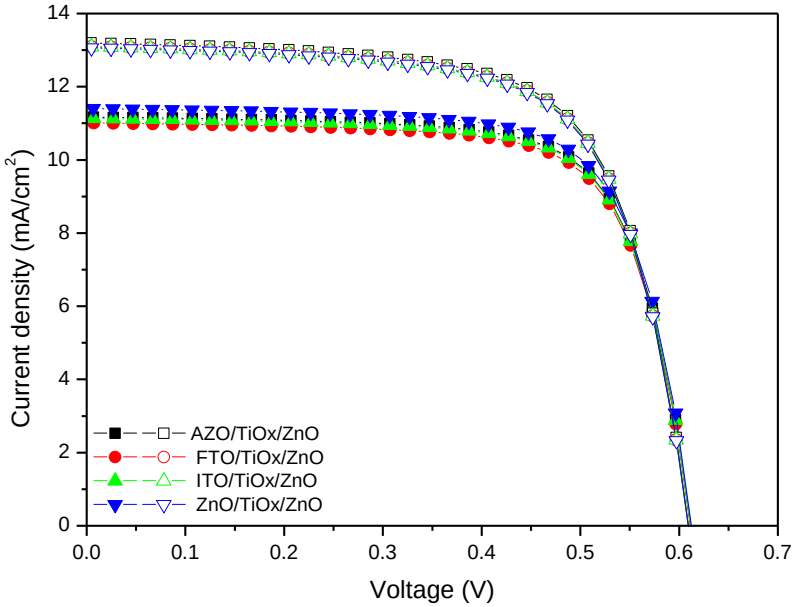

Figure IV.20: Effect of different TCO in TCO/TiO_x/ZnO bottom electrodes on J-V characteristics for: (solid symbols) OSC, (hollow symbols) IOSC.

Table IV.5: Effect of different bottom oxides using in tri-layer electrode on OSC and IOSC outputs.

Structure	Multilayers electrode	$J_{sc}(mA/cm^2)$	$V_{oc}(V)$	FF (%)	η(%)
OSC	FTO/TiO_x/ZnO	11.01	**0.61**	72.05	4.85
	AZO/TiO_x/ZnO	11.17	0.61	71.99	4.92
	ITO/TiO_x/ZnO	11.14	0.61	72.00	4.90
	ZnO/TiO_x/ZnO	**11.41**	**0.61**	**71.88**	**5.02**
IOSC	FTO/TiO_x/ZnO	13.10	0.61	67.84	5.41
	AZO/TiO_x/ZnO	**13.20**	**0.61**	**67.81**	**5.46**
	ITO/TiO_x/ZnO	13.10	0.61	67.83	5.41
	ZnO/TiO_x/ZnO	13.07	0.61	67.83	5.40

It can be seen that TCO has the most impact on OSC efficiency than that of IOSC. ZnO improves OSC efficiency to 5.02%. However, IOSC efficiency reaches only 5.46% by using AZO.

Figure IV.21 presents band level alignment of the considered TCO in TCO/TiO_x/ZnO. It shows that the collection of electrons in the bottom of the IOSC is more favored by the use of AZO/TiO_x/ZnO. However, less improvement in hole collection is associated with the use of ZnO/TiO_x/ZnO. Better transmission have to be performed at the bottom while electron collection that occurs exclusively at the top of OSC is controlled by energy level alignment. Since the electrons mobility exceeds that of holes, their collection will be more sensitive to the top electrode proprieties then the slow hole collection at the top for IOSC.

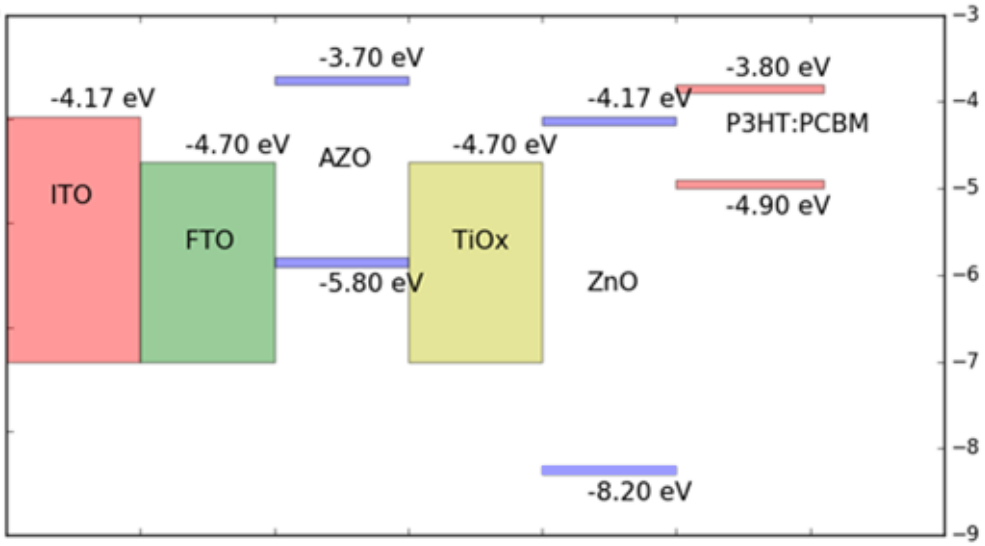

Figure IV.21: Band level alignment of the suggested TCO in TCO/TiOx/ZnO bottom contacts.

IV.1.2. Study of conventional and inverted P3HT:PCBM OSC using SILVACO ATLAS

In this section P3HT:PCBM OSCs are investigated using SILVACO ATLAS. The same steps are followed as in the previous subsection to optimize and compare between the two cells, the conventional (OSC) and inverted (IOSC) organic solar cell: the thickness of the different layers and a number of materials are tested for the best performing ETL and HTL materials.

The structures studied in this work are presented in Figure IV.1. The input parameters of primarily structure used in this work are in the Table IV.6.

Table IV.6: Organic solar cell (OSC) input parameters.

Parameters	Symbol	PEDOT:PSS [132]	P3HT:PCBM [98]	TiO_2 [133, 134]
Energy gap	$E_g(eV)$	2.2	1.1	3.26
Affinity	$\chi(eV)$	2.9	3.8	4.2
Relative permittivity	ε_r	3	3.4	10
Effective density of states in the valence band	$N_c(cm^{-3})$	2.2×10^{15}	2.2×10^{18}	1×10^{21}
Effective density of states in the conduction band	$N_v(cm^{-3})$	1.8×10^{18}	1.8×10^{19}	2×10^{20}
electron mobility	$\mu_n(cm^2/Vs)$	2×10^{-2}	2×10^{-3}	20
hole mobility	$\mu_p(cm^2/Vs)$	2×10^{-4}	2×10^{-4}	10
Electron trap density	$N_e^{exp} cm^{-3}eV^{-1}$		3.8×10^{20}	
Hole trap density	$N_h^{exp} cm^{-3}eV^{-1}$		1.45×10^{19}	
Electron tail slope	N_e^U eV		40×10^{-3}	
Hole tail slope	N_h^U eV		60×10^{-3}	

IV.1.2.1. Effect of thicknesses: comparison between OSC and IOSC

IV.1.2.1.1. The active layer thickness

In order to perform a comparative study and to optimize the performance of each structure of BHJ, the thickness of the active layer has been varied from 100 nm to 500 nm. Figure IV.22 shows the J-V characteristics obtained for OSC and IOSC. Figure IV.23 presents the extracted electrical outputs.

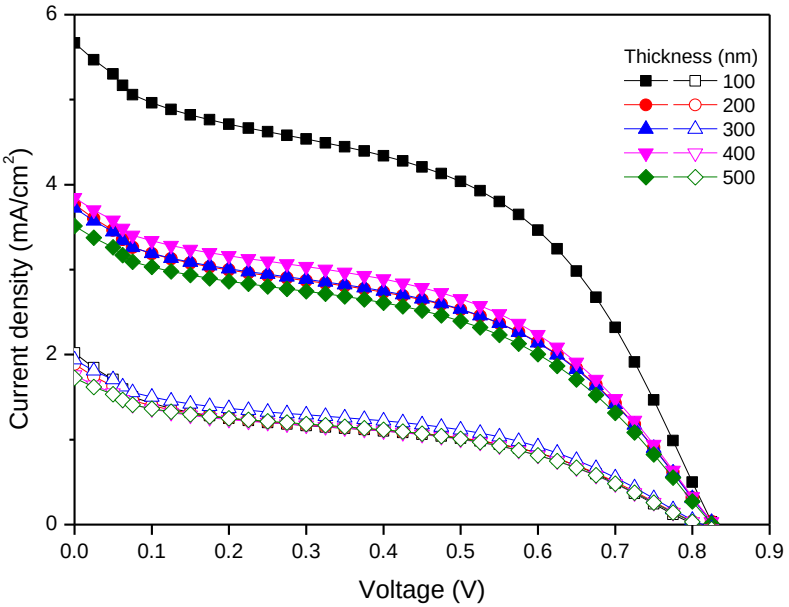

Figure IV.22: J-V characteristic for different active layer thicknesses: (solid symbols) OSC, (hollow symbols) IOSC.

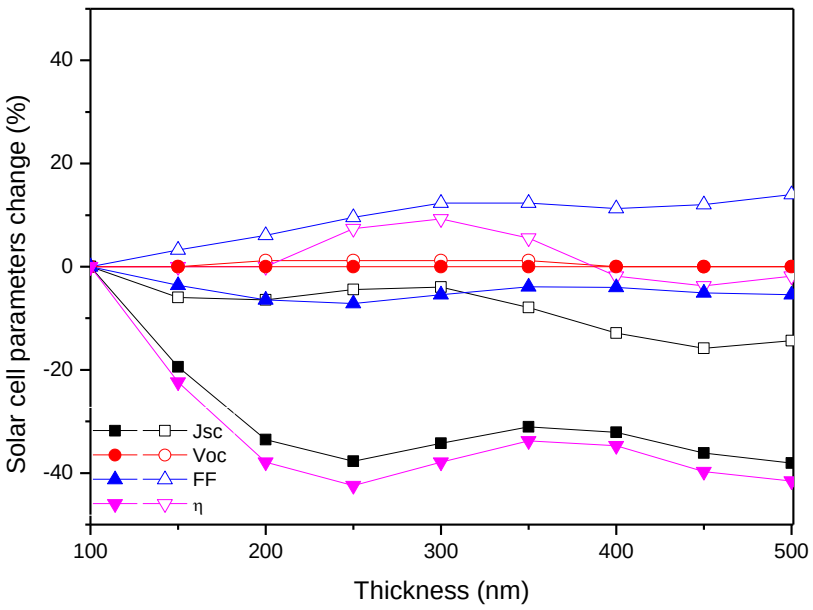

Figure IV.23: The percentage change in the extracted electrical outputs (OSC: solid symbols and IOSC: hollow symbols) from the J-V curves (figure IV.20) with active layer thickness increase.

From Figure IV.22, We observe S-shaped J–V curves for the two cells studied, this deformation in curves reduce with reduction of active layer thickness.

S-shaped deformation, or kink, is one important issue often encountered in OSCs and its origin is still under discussion. The kink in J–V curves can severely reduce the fill factor (FF) leading to poor efficiency of the solar cell. The S-shaped J–V curve has been attributed in OSCs to various physical phenomena: charge accumulation at the interface, unbalanced charge transportation, poor extraction of charge, interfacial energy barriers, exciton blocking layer thickness, transport layer doping, morphology and thickness of the active layers, besides to charge carrier mobility [135, 136].

Further studies demonstrate the presence of S-shaped J–V curves in the cells of different materials and structures as well as in inorganic solar cells. Experimentally, they found that the curvature of the J-V curves disappeared upon light soaking under UV radiation [136].

In Figure IV.23, it is observed that the electrical outputs are very sensitive with active layer variation, whilst V_{oc} seems to be constant at 0.85 V and 0.84 V in OSC an IOSC. Smaller thicknesses of 100 nm in OSC, gives optimal efficiency of 2.19%, which decreases significantly with increasing active layer thickness, while 0.59% for IOSC at 300 nm.

IV.1.2.1.2. Effect of ETL thickness

Now, the ETL thickness effect is considered. Active layer thicknesses is fixed at 100 nm and 300 nm for OSC and IOSC, respectively. The chosen thicknesses correspond to the best efficiencies. The chosen ETL material TiO_2 (different materials will be considered later) and the thickness of the layer is varied from 10 to 60 nm in both OSC and IOSC. The resulting J–V characteristics are shown in Figure IV.24, the extracted electrical outputs are plotted in Figure IV.25.

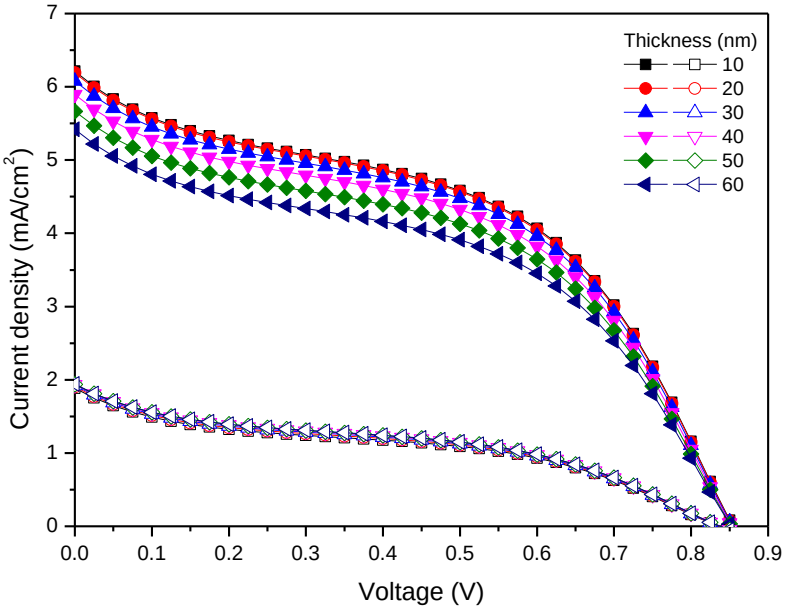

Figure IV.24: J-V characteristics obtained by varying the ETL thickness: (solid symbols) OSC, (hollow symbols) IOSC.

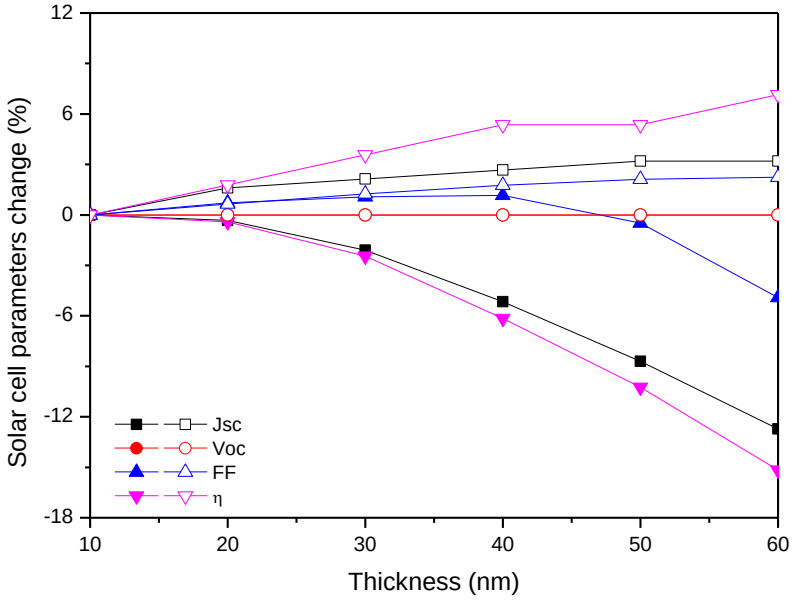

Figure IV.25: The percentage change in the extracted electrical outputs (OSC: solid symbols and IOSC: hollow symbols) from the J-V curves (figure IV.22) with the ETL thickness increase.

The best OSC and IOSC performances obtained are 2.44% and 0.6% for 10 nm and 60 nm ETL thicknesses. For conventional cell, as the ETL thickness increases, slight decrease is observed

in FF, J_{sc} and PCE. Completely opposite changes observed for the inverted structure. Overall, the effect of the ETL thickness is minor and more exactly nonexistent for outputs parameters in both solar cells except for $V_{oc}$is constant at 0.85 V and 0.84 V for both solar cells.

IV.1.2.1.3. Effect of HTL thickness

In this section, a study of HTL thickness effect on the performance of OSC and IOSC is undertaken. The first chosen HTL material is PEDOT:PSS and its thickness is varied from 10 nm to 60 nm. Figure IV.26 shows the obtained J-V characteristics and Figure IV.27 plots the extracted electrical outputs.

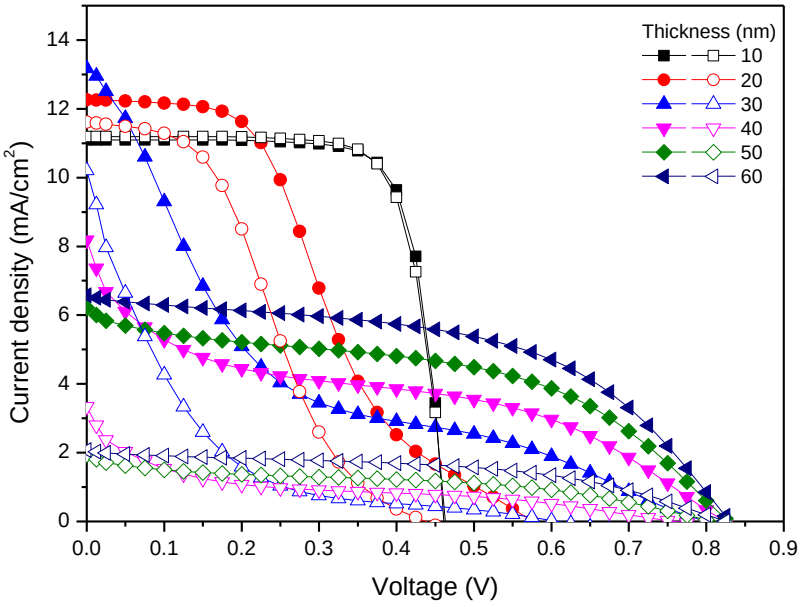

Figure IV.26: J-V characteristic obtained by varying the HTL thickness: (solid symbols) OSC, (hollow symbols) IOSC.

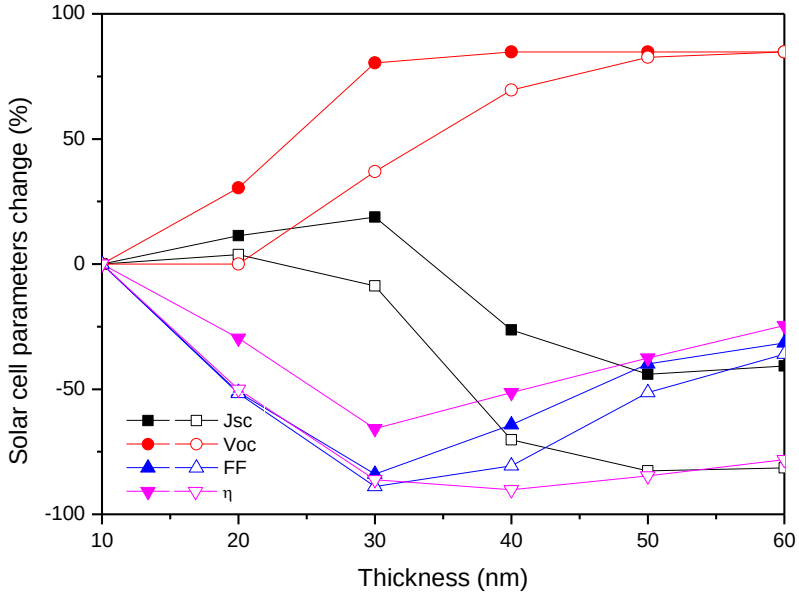

Figure IV.27: The percentage change in the extracted electrical outputs (OSC: solid symbols and IOSC: hollow symbols) from the J-V curves (figure IV.24) with the HTL thickness increase.

It clear that the best performances obtained at minimal HTL thickness. 10 nm gives an efficiency of 3.91% and 3.90%. Furthermore, as the HTL thickness increases, slight decrease is observed in FF and η until it reaches 30 thickness, they start to increase gradually. J_{sc} presents a slight decrease from 11.10 to 6.58 mA/cm^2 and from 11.19 to 2.07 mA/cm^2, FF decreases from 76.54 to 52.43% and from 75.33 to 48.13%, the efficiency η changes from 3.91% to 2.95% and from 3.90 to 0.85%, for OSC and IOSC, respectively. While $V_{oc}$is increasing from 0.46 to 0.85 V for the both cells.

IV.1.2.2. Effect of ETL material

In this section, a number of materials used in other works as ETL in organic solar cells are tested in order to determine which one gives better performance.

In this study the proposed materials are: TiO_2, ZnO and AZO, their parameters are listed in Table IV.7, and the obtained J-V characteristics are presents Figure IV.28.

Table IV.7: Input parameters of the proposed ETL materials.

Parameters	ZnO[134]	AZO [137]
$E_g(eV)$	3.3	3.3
$\chi(eV)$	4.1	4.45
ε_r	9	9
$N_c(cm^{-3})$	4×10^{18}	3×10^{18}
$N_v(cm^{-3})$	1×10^{19}	1.7×10^{19}
$\mu_n(cm^2/Vs)$	100	100
$\mu_p(cm^2/Vs)$	25	31
$N_d(cm^{-3})$	1×10^{18}	1×10^{20}

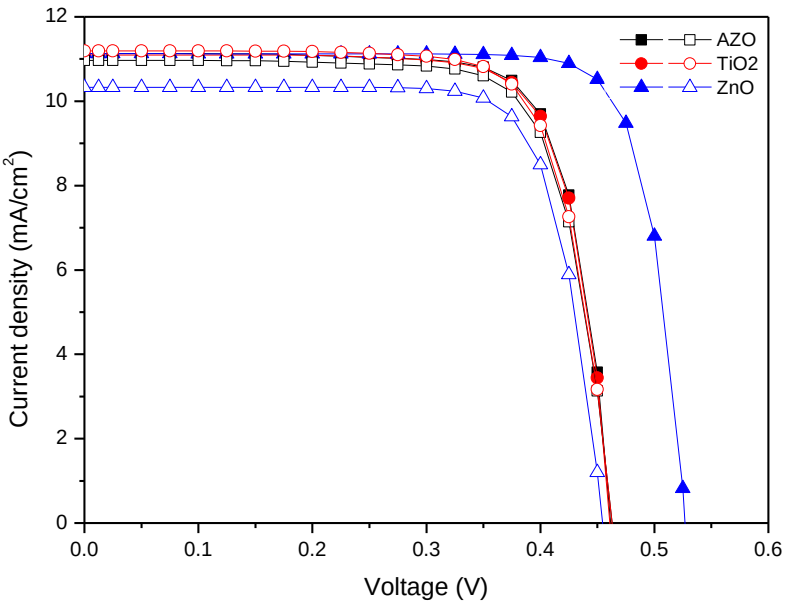

Figure IV.28: The J-V characteristics obtained for three different ETL materials: (solid symbols) OSC and (hollow symbols)IOSC.

ZnO is the most suitable ETL materials for OSC, gives best efficiency of 4.73%, and for the inverted structure 3.90% is the better efficiency when using TiO_2. The variation of J_{sc} in OSC is not significant, can be interpreted as ETL is in the back of active layer which considered as optical

spacer and don't affect the absorption of light. The extracted output parameters are given in Table IV.8.

Table IV.8: Effect of different ETL materials on electrical outputs of OSC and IOSC. The bold values are the best performances.

Parameters		$J_{sc}(mA/cm^2)$	$V_{oc}(V)$	FF (%)	η(%)
OSC	**ZnO**	**11.13**	**0.53**	**80.71**	**4.73**
	TiO_2	11.10	0.46	76.54	3.91
	AZO	11.13	0.46	76.60	3.93
IOSC	ZnO	10.33	0.45	76.92	3.61
	TiO_2	**11.19**	**0.46**	**75.33**	**3.90**
	AZO	10.97	0.46	75.45	3.83

IV.1.2.3. Effect of HTL material

In this section, the proposed materials as HTL taken from other works are: PEDOT: PSS (Poly(3,4-ethylenedioxythiophene)-poly(styrenesulfonate)), NiO and Cu_2O, the parameters of these materials are listed in Table IV.9. Figure IV.29 shows the J-V characteristics of OSC and IOSC and the extracted electrical outputs are summarized in Table IV.10.

Table IV.9: Input parameters of the proposed HTL materials.

Parameters	NiO[134, 138]	Cu_2O[139]
$E_g(eV)$	3.6	2.2
$\chi(eV)$	1.46	3.2
ε_r	11	7.11
$N_c(cm^{-3})$	1.1×10^{19}	2×10^{17}
$N_v(cm^{-3})$	1.6×10^{19}	1.1×10^{19}
$\mu_n(cm^2/Vs)$	12	200

$\mu_p(cm^2/Vs)$	25	80
$N_d(cm^{-3})$	0	0
$N_a(cm^{-3})$	1×10^{16}	1×10^{18}

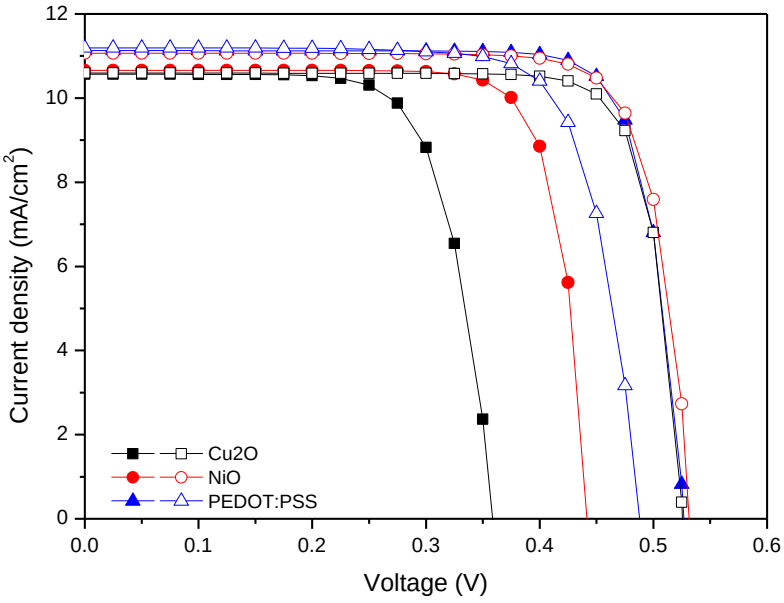

Figure IV.29: The J-V characteristic obtained for three different HTL materials: (solid symbols) OSC, (hollow symbols) IOSC.

It is observed from Table IV.10, the best performance is achieved for PEDOT: PSS and NiO HTM, with an efficiency reaches to 4.73% and 4.77% for OSC and IOSC. The variation of HTM don't effect on J_{sc} value in IOSC because it is located at the back of absorber layer, contrary to OSC which situated in the front.

Table IV.10: Effect of different HTL materials on electrical outputs of OSC and IOSC. The bold values are the best performances.

Parameters		$J_{sc}(mA/cm^2)$	$V_{oc}(V)$	FF (%)	η(%)
OSC	**PEDOT:PSS**	**11.13**	**0.53**	**80.71**	**4.73**
	NiO	10.66	0.44	79.77	3.76

	Cu_2O	10.57	0.36	71.71	2.72
IOSC	PEDOT:PSS	11.19	0.46	75.33	3.90
	NiO	**11.12**	**0.53**	**80.56**	**4.77**
	Cu_2O	11.06	0.53	80.18	4.71

IV.1.2.4. Investigation of multilayers electrode

In this part, electrodes consisting of multilayers of different materials are investigated since this may gave a positive effect on the solar cell efficiency. Firstly, the optical properties of different transparent multilayers are investigated to find the best electrodes (materials and thicknesses) using a developed MATLAB code. Secondly, this optimised multilayer electrode is used in the optimized OSC in its standard and inverted devices.

IV.1.2.4.1. Transmittance evaluation

Various researchers have employed intermediate metallic layers made of Ag, Au, Cu, Al, etc. However, due to its lowest absorption coefficient and lowest refractive index (n=0.05-i2.90) in the visible range of the solar spectrum, Ag is thought to be the ideal option for this application [3].

In the optimization of the TCO/Ag/TCO multilayer, the proper choice of Ag interlayer thickness is extremely important because the optical and electrical properties of the TCO/metal/TCO multilayer are greatly influenced by Ag thickness [140]. As mentioned in chapter II, Ag has to be thin enough to be transparent, when the metal layer thickness is increased to 15 nm, both optical and electrical parameters exhibit a sharp drop, with resistance being the most pronounced [16]. It was found that TCO/metal/TCO multilayer with same top and bottom TCO thickness produce a higher optical transmittance than multilayer with different bottom and top TCO thickness [140]. Therefore, we used identical bottom and top TCO layers with same variation of thickness.

Through the numerical method described previously in a MATLAB code (in chapter III), we were able to calculate the optical properties of TCO/Ag/TCO structures, by using the TCO complex refractive index and the thin Ag complex refractive index.

The first step is studying the multilayers electrode which has (TCO/Ag/TCO) structure by changing the silver thickness from 4 nm to 10 nm in order to find the best metal thickness and then changing the TCO thickness from 20 nm to 80 nm in each anode structure. The TCOs studied in the multilayer electrodes are ZnO, AZO, TiO_2, and MoO_3. The transmittances of the studied multilayers are illustrated in Figures IV.30.

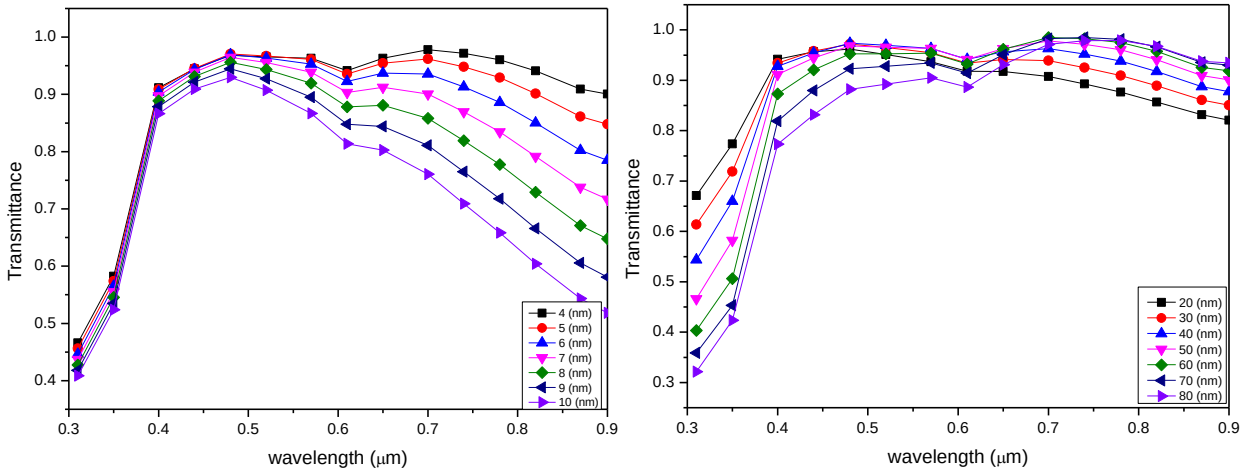

a) ZnO/Ag/ZnO

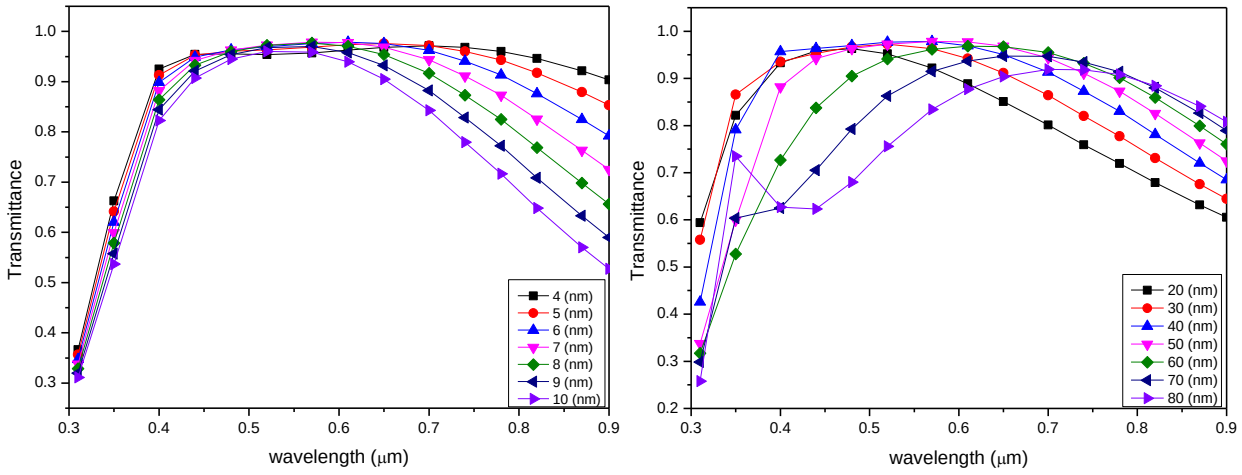

b) AZO/Ag/AZO

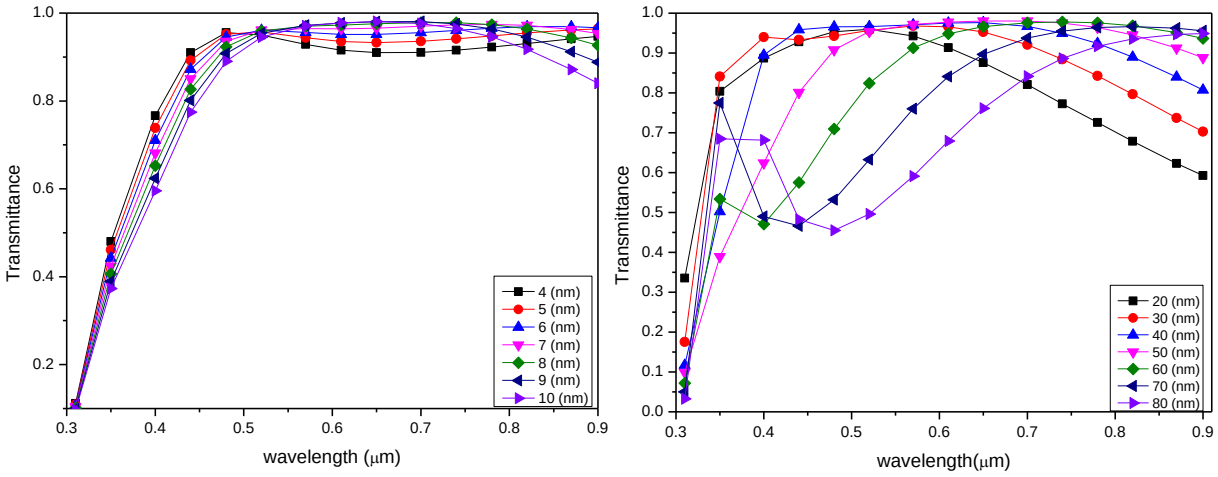

c) $TiO_2/Ag/TiO_2$

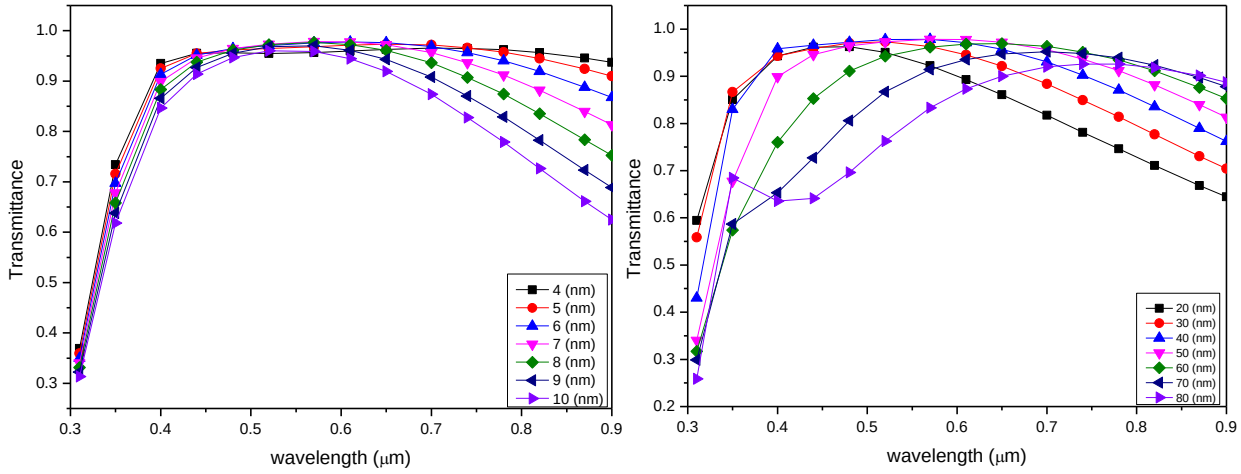

d) $MoO_3/Ag/MoO_3$

Figure IV.30: In the left is silver thicknesses variation and in the right the TCO thicknesses variation versus wavelength in a) ZnO/Ag/ZnO, b) AZO/Ag/AZO, c) $TiO_2/Ag/TiO_2$, and d) $MoO_3/Ag/MoO_3$ multilayer structures.

One of the key factors in achieving high transmission and low sheet resistance in these TCO/metal/TCO electrodes is the metal thickness. For a thin Ag thickness, the TCO/Ag/TCO multilayer showed fairly high optical transmittance. As the thickness of Ag interlayer increases, the multilayer showed low transmittance owing to reflection of light on the Ag metal layer. A

TCO/Ag/TCO multilayer electrodes with Ag interlayer thickness of 4 nm showed an optimal optical transmittance.

Figure IV.31 Shows the transmittance curve of ITO thin film taken from [141], the maximum transmittance is about 81.23% at 0.5876 μm of wavelength with 100 nm of thickness. Figure IV.32 represents the transmittance of multilayers versus the metal and TCO thickness.

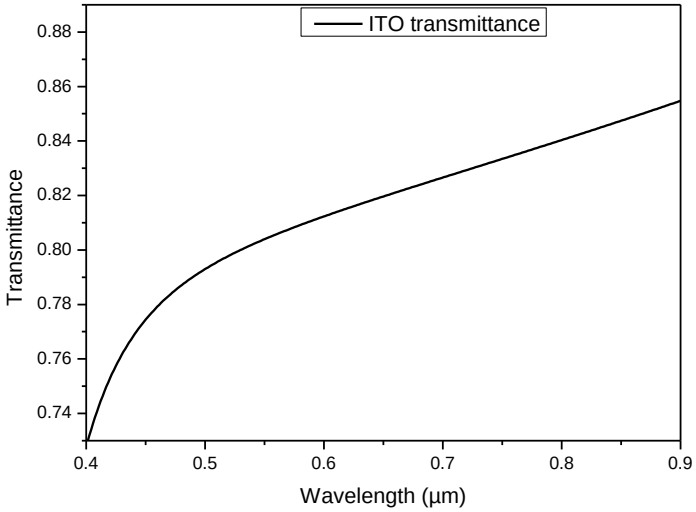

Figure IV.31: The transmittance of ITO versus wavelength.

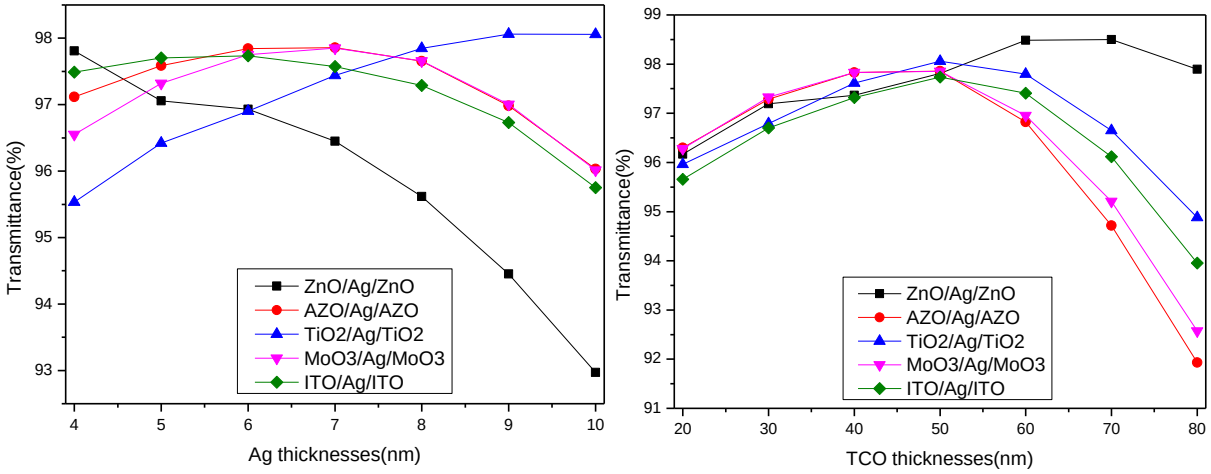

Figure IV.32: The transmittance variation versus (left: silver thickness change, right: TCO thickness change) in multilayers structure.

Table IV.11 resumes the optimal results obtained from each best multilayer structure. Obviously, it can be said that the results are very close to each other, but the best one is for ZnO(70nm)/Ag(4nm)/ZnO(70nm) that takes the optimal transmittance of 98.5% followed by TiO_2(50nm)/Ag(9nm)/TiO_2(50nm) with transmittance of 98.06%.

Table IV.11: The transmittance obtained for all multilayers studied.

Structure	Transmittance (%)
ITO (100 nm)	81.23 [141]
ZnO(70nm)/Ag(4nm)/ZnO(70nm)	98.5
AZO(50nm)/Ag(7nm)/AZO(50nm)	97.86
TiO_2(50nm)/Ag(9nm)/TiO_2(50nm)	98.06
MoO3(50nm)/Ag(7nm)/MoO3(50nm)	97.85

As seen in Table IV.11, the transmittance of studied multilayers is above 97% and their values are similar and higher than transmittance of ITO single layer (81.23%).

IV.1.2.4.2. Application of the multilayer electrode in standard and inverted OSCs

Having studied the multilayer electrodes, we will examine the effect of these multilayers electrodes in the optimized standard and inverted OSC, and compare the results with ITO electrode. The J-V characteristics of multilayers electrodes based OSC and IOSC are presented in Figure IV.33, and the obtained results are resumed in TablesVI.12.

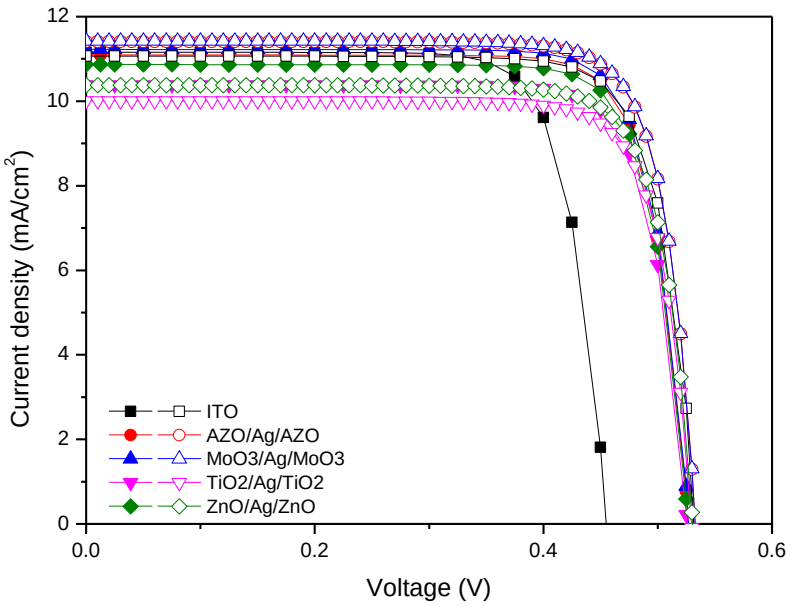

Figure IV.33: J-V characteristics of the organic solar cells optimized as function of deferent multilayer electrode: (solid symbols) OSC, (hollow symbols) IOSC structure.

Table IV.12: Effect of different TCO in (TCO/Ag/TCO) multi-layers electrode on OSC and IOSC outputs.

structure	Multilayers electrode	J_{sc} (mA/cm^2)	V_{oc} (V)	FF (%)	η(%)
OSC	**MoO_3(50nm)/Ag(7nm)/MoO_3(50nm)**	**11.22**	**0.53**	**80.71**	**4.78**
	ZnO(70nm)/Ag(4nm)/ZnO(70nm)	10.87	0.53	80.70	4.62
	TiO_2(50nm)/Ag(9nm)/TiO_2(50nm)	10.39	0.53	80.66	4.40
	AZO(50)/Ag(7nm)/AZO(50nm)	11.09	0.53	80.71	4.72
IOSC	**MoO_3(50nm)/Ag(7nm)/MoO_3(50nm)**	**11.43**	**0.53**	**80.61**	**4.91**
	ZnO(70nm)/Ag(4nm)/ZnO(70nm)	10.38	0.53	80.49	4.43
	TiO_2(50nm)/Ag(9nm)/TiO_2(50nm)	10.01	0.53	80.47	4.27
	AZO(50)/Ag(7nm)/AZO(50nm)	**11.41**	**0.53**	**80.61**	**4.90**

As see in Table IV.12, all the alternative electrodes have the efficiencies generally close and similar to that obtained with using single layer ITO electrode. The best multilayer anode for OSC

is MoO_3/Ag/MoO_3 with total thickness of 107 nm which has an efficiency of 4.78%, followed by AZO/Ag/AZO, ZnO/Ag/ZnO and TiO_2/Ag/TiO_2 with the efficiency of 4.72%, 4.62% and 4.40%, respectively. On the other hand, the performance of IOSC is improved with using multilayer cathode from 4.77% by using single layer ITO cathode to 4.91% and 4.90% after using MoO_3/Ag/MoO_3 and AZO/Ag/AZO electrodes, while the use of ZnO/Ag/ZnO and TiO_2/Ag/TiO_2 give an efficiency of 4.43% and 4.27%, respectively.

Conclusion

Using GPVDM software, the electrical comparative of Conventional and Inverted P3HT: PCBM Organic Solar Cells have been investigated. The organic solar cell (OSC) and Inverted organic solar cell (IOSC) have been simulated at different active layer thickness, different ETL and HTL thicknesses and materials and also by using multi-thin layer electrodes.

Similar work done using Silvaco atlas, while the design and the optimization of multilayer electrodes done by Matlab. The results are close and not far from the experimental results. whether by using gpvdm software or by silvaco atlas program.

For TCO/metal/TCO multilayers electrode, by using GPVDM software, the best performance obtained after utilize AZO(40nm)/Ag(6nm)/AZO(40nm) multilayer for the both configuration. For OSC the efficiency reaches 4.96% for the structure Al/TiOx(50 nm)/P3HT:PCBM(150 nm)/multilayer, whereas, for IOSC the best structure is Ag/PEDOT:PSS(20 nm)/P3HT:PCBM(200 nm)/multilayer with the best efficiency of 5.29%,.

On other hand, after using silvaco atlas, the employ of MoO_3(50nm)/Ag(7nm)/MoO_3(50nm) or AZO(50)/Ag(7nm)/AZO(50nm) gives a close results for both type configuration of OSC. For OSC the optimal performance reaches to 4.78% for the structure Al/ZnO(10 nm)/P3HT:PCBM(100 nm)/multilayer after using MoO_3/Ag/MoO_3 while the inverted is Ag/NiO(10 nm)/P3HT:PCBM(300 nm)/multilayer, with the efficiency of 4.91%.

The tri-layer oxides electrode (oxide/TiOx/ZnO) are tested only using GPVDM. ZnO(60nm)/TiO_x(10nm)/ZnO(10nm) and AZO(80nm)/TiO_x(10nm)/ZnO(10nm) are the chosen one give an efficiencies 5.02% and 5.46% for OSC and IOSC respectively.

CONCLUSION

CONCLUSION

The aim of our work is to find an alternative for ITO single layer electrode for organic solar cells applications. The structure TCO/Metal/TCO is evaluated as a candidate for a multiple layer electrode. Before this evaluation organic solar cells in conventional (OSC) and inverted (IOSC) configurations were simulated under AM1.5 solar spectrum at 300 °K using GPVDM and SILVACO ATLAS software. Each cell has been studied and optimized from the point of view of the thickness of each constituent layer (active layer, electron transporting layer ETL and hole transporting layer HTL). After that, a number of materials as ETL and HTM have been tested and their effect has been studied, finally numbers of multilayer electrodes configurations are tested.

In the first part of simulation, the two types of organic solar cells structure were simulated by GPVDM in order to compare between them and enhance their performance. In the primary cell, the considered "ETL" and "HTL" layers were a 50 nm of TiO_2 and PEDOT:PSS, respectively, the active layer was a bulk heterojunction (BHJ) P3HT:PCBM. After optimization of the layers thicknesses and ETL/HTL materials, it was found that the best structures are Al/ TiO_x (50 nm)/ P3HT:PCBM (150 nm)/ Cu_2O (10 nm)/ITO and Ag/ PEDOT:PSS (20 nm)/ P3HT:PCBM (200 nm)/ ZnO (30nm)/ITO for conventional organic solar cell (OSC) and inverted organic solar cell (IOSC) with a power conversion efficiency of 4.77% and 5.35% respectively. The best candidate as TCO/Metal/TCO multilayers transparent electrode is AZO(40 nm)/Ag(6 nm) /AZO(40 nm) for both structures. The resulting performances were found to be 4.96% and 5.29% for OSC and IOSC, respectively.

In the second part, the same primary cells with similar parameters and study steps are simulated by SILVACO ATLAS. It was found that best performance achieved for OSC and IOSC, respectively, were 4.73 % and 4.77 %, for the configurations of Al/ ZnO (10 nm)/ P3HT:PCBM (100 nm)/ PEDOT:PSS (10 nm)/ITO and Ag/ NiO (10 nm)/ P3HT:PCBM (300 nm)/ TiO2 (60nm)/ITO.

Here, the design and optimization of TCO/Ag/TCO multilayer electrodes are achieved by using MATLAB. In the structure of TCO/metal/TCO, Ag is the ideal option as an intermediate metallic layer for this application due to its lowest absorption coefficient and lowest refractive index in the visible range of the solar spectrum. So the optimization has gone through two steps.

First, study and optimize Ag and TCOs thickness followed by selecting the TCO material. It was found that the transmittance of all multilayers studied are above 97% almost better than ITO single layer electrode (around 81%), the highest transmittance achieved was 98.50% for ZnO(70nm)/Ag(4nm)/ZnO(70nm) multilayers structure. Investigation of optimized multilayers in organic solar cell enhanced the solar cell performance, compared to the single TCO electrode, and give an improved efficiency of 4.78% and 4.91% after using MoO_3(50nm)/Ag(7nm)/MoO_3(50nm) for OSC and IOSC, respectively. These results are due to the improved electrical and optical performances accomplished with the TCO/metal/TCO electrodes compared to that obtained with single TCO or metal thin films.

Our primary goal was to design by optimizing the TCO/Metal/TCO multilayer electrodes numerically using MATLAB, and then realise these optimized electrodes in laboratory. The final step was to use the characterised lab-made multilayers performances to improve solar cells in SILVACO. Unfortunately, the laboratory realisation of the optimized multi-layer electrodes has been cancelled because of the very small thickness of layers.

REFERENCES

1. Tonui, P., et al., *Perovskites photovoltaic solar cells: An overview of current status.* Renewable and Sustainable Energy Reviews, 2018. **91**: p. 1025-1044.

2. Shi, Z. and A.H. Jayatissa, *Perovskites-based solar cells: A review of recent progress, materials and processing methods.* Materials, 2018. **11**(5): p. 729.

3. Sibin, K., et al., *Highly transparent and conducting ITO/Ag/ITO multilayer thin films on FEP substrates for flexible electronics applications.* Solar Energy Materials and Solar Cells, 2017. **172**: p. 277-284.

4. Kim, J.H., et al., *Dependence of optical and electrical properties on Ag thickness in TiO2/Ag/TiO2 multilayer films for photovoltaic devices.* Ceramics International, 2015. **41**(6): p. 8059-8063.

5. Drakonakis, V.M., et al., *Investigating electrodes degradation in organic photovoltaics through reverse engineering under accelerated humidity lifetime conditions.* Solar Energy Materials and Solar Cells, 2014. **130**: p. 544-550.

6. Barrows, A.T., et al., *Indium-free multilayer semi-transparent electrodes for polymer solar cells.* Solar Energy Materials and Solar Cells, 2016. **144**: p. 600-607.

7. Kim, M., et al., *Design of a MoOx/Au/MoOx transparent electrode for high-performance OLEDs.* Organic Electronics, 2016. **36**: p. 61-67.

8. Hrostea, L., et al., *Oxide/metal/oxide electrodes for solar cell applications.* Solar energy, 2017. **146**: p. 464-469.

9. Lopéz, I.P., et al., *Dielectric/metal/dielectric structures using copper as metal and MoO3 as dielectric for use as transparent electrode.* Thin Solid Films, 2012. **520**(20): p. 6419-6423.

10. Cattin, L., et al., *Investigation of low resistance transparent MoO3/Ag/MoO3 multilayer and application as anode in organic solar cells.* Thin Solid Films, 2010. **518**(16): p. 4560-4563.

11. He, X., et al., *Experimental and theoretical analysis of ZnO/Au/ZnO transparent conducting thin films.* Vacuum, 2015. **120**: p. 17-21.

12. Mouchaal, Y., et al., *Broadening of the transmission range of dielectric/metal multilayer structures by using different metals.* Vacuum, 2015. **111**: p. 32-41.

13. Jeong, J.-A., Y.-S. Park, and H.-K. Kim, *Comparison of electrical, optical, structural, and interface properties of IZO-Ag-IZO and IZO-Au-IZO multilayer electrodes for organic photovoltaics.* Journal of Applied Physics, 2010. **107**(2): p. 023111.

14. Wang, Z., et al., *Efficient Inverted ITO-Free Organic Solar Cells Based on Transparent Silver Electrode with Aqueous Solution-Processed ZnO Interlayer.* International Journal of Photoenergy, 2017. **2017**.

15. Zhao, Z. and T. Alford, *The optimal TiO2/Ag/TiO2 electrode for organic solar cell application with high device-specific Haacke figure of merit.* Solar Energy Materials and Solar Cells, 2016. **157**: p. 599-603.

16. Guillen, C. and J. Herrero, *TCO/metal/TCO structures for energy and flexible electronics.* Thin Solid Films, 2011. **520**(1): p. 1-17.

17. Cho, S.-W., et al., *Highly flexible, transparent, and low resistance indium zinc oxide–Ag–indium zinc oxide multilayer anode on polyethylene terephthalate substrate for flexible organic light light-emitting diodes.* Thin Solid Films, 2008. **516**(21): p. 7881-7885.

18. Dimopoulos, T., et al., *Characterization of ZnO: Al/Au/ZnO: Al trilayers for high performance transparent conducting electrodes.* Thin Solid Films, 2010. **519**(4): p. 1470-1474.

19. Liu, S.-W., et al., *ITO-free, efficient, and inverted phosphorescent organic light-emitting diodes using a WO3/Ag/WO3 multilayer electrode.* Organic Electronics, 2016. **31**: p. 240-246.

20. Kung, P.K., et al., *A review of inorganic hole transport materials for perovskite solar cells.* Advanced Materials Interfaces, 2018. **5**(22): p. 1800882.

21. Huang, H. and J. Huang, *Organic and Hybrid Solar Cells*2014: Springer.

22. Nunzi, J.-M., *Organic photovoltaic materials and devices.* Comptes Rendus Physique, 2002. **3**(4): p. 523-542.

23. Li, D., *Development of imide-and imidazole-containing electron acceptors for use in donor-acceptor conjugated compounds and polymers*, 2013, Carleton University.

24. Kumavat, P.P., P. Sonar, and D.S. Dalal, *An overview on basics of organic and dye sensitized solar cells, their mechanism and recent improvements.* Renewable and Sustainable Energy Reviews, 2017. **78**: p. 1262-1287.

25. Choy, W.C., *Organic solar cells: Materials and device physics*2012: Springer.

26. Wang, C.C., *Organic solar cells towards high efficiency: plasmonic effects and interface engineering*, 2012, University of Hong Kong.

27. Potscavage Jr, W.J., *Physics and engineering of organic solar cells*2011: Georgia Institute of Technology.

28. YAHYA, W.Z.N., *Synthesis and characterisation of nanostructured π-conjugated oligomers and polymers for organic photovoltaic*, 2012., University of Joseph: Fourier ,Grenoble.

29. Rafique, S., et al., *Fundamentals of bulk heterojunction organic solar cells: An overview of stability/degradation issues and strategies for improvement.* Renewable and Sustainable Energy Reviews, 2018. **84**: p. 43-53.

30. Derbal, H., *Cellules solaires photovoltaïques plastiques nanostructurées*, 2009, Angers.

31. Sze, S.M., Y. Li, and K.K. Ng, *Physics of semiconductor devices*2006, Hoboken, New Jersey: John wiley & sons.

32. Gupta, A., *Organic solar cells and its characteristics.* J Material Sci Eng, 2015. **4**(203): p. 2169-0022.1000203.

33. Boudjemline, S.A., *Réalisation et caractérisation des cellules photovoltaïques plastiques*, 2004, Angers.

34. Brousse, B., *Réalisation et caractérisation de cellules photovoltaïques organiques obtenues par dépôt physique*, 2004, Limoges.

35. A.Douha, *Étude de l'effet de la température sur les paramètres d'une cellule solaire organique Ingéniera d'état en science des matériaux*, Juin 2008, Béchar university center.

36. Schmidt-Mende, L., et al., *Self-organized discotic liquid crystals for high-efficiency organic photovoltaics.* Science, 2001. **293**(5532): p. 1119-1122.

37. Kraus, J.K., *Physics of molecular donor-acceptor solar cells: Correlation between interface morphology, energetics and device performance.* 2013.

38. L, B., *Polymères semiconducteurs à faible larger de la bande interdite: de la synthèse au dispositive photovlotaïque organique*, 2010, Strasbourg University.

39. Apaydın, D.H., et al., *Optimizing the organic solar cell efficiency: role of the active layer thickness.* Solar Energy Materials and Solar Cells, 2013. **113**: p. 100-105.

40. Elumalai, N.K., et al., *Metal oxide semiconducting interfacial layers for photovoltaic and photocatalytic applications.* Materials for Renewable and Sustainable Energy, 2015. **4**(3): p. 1-25.

41. Gevorgyan, S.A., *Production, characterization and stability of organic solar cell devices.* 2010.

42. Zhang, D., *Transparent electrode design and interface engineering for high performance organic solar cells.* HKU Theses Online (HKUTO), 2014.

43. Lide, D., *CRC Handbook of Chemistry and Physics, seventyeighth ed.* Chemical Rubber Company Press, Boca Raton, FL, 1997: p. 4-50.

44. Charton, C. and M. Fahland, *Optical properties of thin Ag films deposited by magnetron sputtering.* Surface and Coatings Technology, 2003. **174**: p. 181-186.

45. So, S., et al., *Transmittance and resistivity of semicontinuous copper films prepared by pulsed-laser deposition.* Applied Physics Letters, 2000. **77**(8): p. 1099-1101.

46. Seal, K., et al., *Growth, morphology, and optical and electrical properties of semicontinuous metallic films.* Physical Review B, 2003. **67**(3): p. 035318.

47. Chopra, K., *Growth of sputtered vs evaporated metal films.* Journal of Applied Physics, 1966. **37**(9): p. 3405-3410.

48. Sarakinos, K., et al., *The effect of the microstructure and the surface topography on the electrical properties of thin Ag films deposited by high power pulsed magnetron sputtering.* Surface and Coatings Technology, 2008. **202**(11): p. 2323-2327.

49. Guillén, C. and J. Herrero, *Transparent conductive ITO/Ag/ITO multilayer electrodes deposited by sputtering at room temperature.* Optics Communications, 2009. **282**(4): p. 574-578.

50. Guillén, C. and J. Herrero, *ITO/metal/ITO multilayer structures based on Ag and Cu metal films for high-performance transparent electrodes.* Solar Energy Materials and Solar Cells, 2008. **92**(8): p. 938-941.

51. Maaroof, A. and D. Sutherland, *Optimum plasmon hybridization at percolation threshold of silver films near metallic surfaces.* Journal of Physics D: Applied Physics, 2010. **43**(40): p. 405301.

52. Ordal, M.A., et al., *Optical properties of fourteen metals in the infrared and far infrared: Al, Co, Cu, Au, Fe, Pb, Mo, Ni, Pd, Pt, Ag, Ti, V, and W.* Applied optics, 1985. **24**(24): p. 4493-4499.

53. Fahsold, G., et al., *Adsorbate-induced changes in the broadband infrared transmission of ultrathin metal films.* Physical Review B, 2002. **65**(23): p. 235408.

54. Chakaroun, M., et al., *High quality transparent conductive electrodes in organic photovoltaic devices.* Thin Solid Films, 2009. **518**(4): p. 1250-1253.

55. Abe, Y. and T. Nakayama, *Transparent conductive film having sandwich structure of gallium–indium-oxide/silver/gallium–indium-oxide.* Materials Letters, 2007. **61**(18): p. 3897-3900.

56. Roh, H.S., S.H. Cho, and W.J. Lee, *Study on the durability against heat in ITO/Ag-alloy/ITO transparent conductive multilayer system.* physica status solidi (a), 2010. **207**(7): p. 1558-1562.

57. Koike, K. and S. Fukuda, *Multilayer transparent electrode consisting of silver alloy layer and metal oxide layers for organic luminescent electronic display device.* Journal of Vacuum Science & Technology A: Vacuum, Surfaces, and Films, 2008. **26**(3): p. 444-454.

58. Indluru, A. and T. Alford, *Effect of Ag thickness on electrical transport and optical properties of indium tin oxide–Ag–indium tin oxide multilayers.* Journal of Applied Physics, 2009. **105**(12): p. 123528.

59. Mohamed, S., *Effects of Ag layer and ZnO top layer thicknesses on the physical properties of ZnO/Ag/Zno multilayer system.* Journal of Physics and Chemistry of Solids, 2008. **69**(10): p. 2378-2384.

60. Lewis, J., et al., *Highly flexible transparent electrodes for organic light-emitting diode-based displays.* Applied Physics Letters, 2004. **85**(16): p. 3450-3452.

61. Song, S., et al., *Effect of GZO thickness and annealing temperature on the structural, electrical and optical properties of GZO/Ag/GZO sandwich films.* Current Applied Physics, 2010. **10**(2): p. 452-456.

62. Park, Y.-S., et al., *Comparative investigation of transparent ITO/Ag/ITO and ITO/Cu/ITO electrodes grown by dual-target DC sputtering for organic photovoltaics.* Journal of the Electrochemical Society, 2009. **156**(7): p. H588.

63. Kim, J.-Y., D. Sohn, and E.-R. Kim, *Polymer-based multi-layer conductive electrode film for plastic LCD applications.* Applied Physics A, 2001. **72**(6): p. 699-704.

64. Guillen, C. and J. Herrero, *Transparent electrodes based on metal and metal oxide stacked layers grown at room temperature on polymer substrate.* physica status solidi (a), 2010. **207**(7): p. 1563-1567.

65. Bender, M., et al., *Dependence of film composition and thicknesses on optical and electrical properties of ITO–metal–ITO multilayers.* Thin Solid Films, 1998. **326**(1-2): p. 67-71.

66. Klöppel, A., et al., *Dependence of the electrical and optical behaviour of ITO–silver–ITO multilayers on the silver properties.* Thin Solid Films, 2000. **365**(1): p. 139-146.

67. Han, H., N. Theodore, and T. Alford, *Improved conductivity and mechanism of carrier transport in zinc oxide with embedded silver layer.* Journal of Applied Physics, 2008. **103**(1): p. 013708.

68. Park, Y.-S., H.-K. Kim, and S.-W. Kim, *Thin Ag layer inserted GZO multilayer grown by roll-to-roll sputtering for flexible and transparent conducting electrodes.* Journal of the Electrochemical Society, 2010. **157**(8): p. J301.

69. Park, H.-K., et al., *Characteristics of indium-free GZO/Ag/GZO and AZO/Ag/AZO multilayer electrode grown by dual target DC sputtering at room temperature for low-cost organic photovoltaics.* Solar Energy Materials and Solar Cells, 2009. **93**(11): p. 1994-2002.

70. Park, Y.-S., K.-H. Choi, and H.-K. Kim, *Room temperature flexible and transparent ITO/Ag/ITO electrode grown on flexile PES substrate by continuous roll-to-roll sputtering for flexible organic photovoltaics.* Journal of Physics D: Applied Physics, 2009. **42**(23): p. 235109.

71. Chakaroun, M., et al., *Organic optoelectronic devices-flexibility versus performance.* The European Physical Journal-Applied Physics, 2010. **51**(3).

72. Choi, K.-H., et al., *Highly flexible and transparent In Zn Sn O x/ Ag/ In Zn Sn O x multilayer electrode for flexible organic light emitting diodes.* Applied Physics Letters, 2008. **92**(22): p. 194.

73. Sawada, M., et al., *Characteristics of indium-tin-oxide/silver/indium-tin-oxide sandwich films and their application to simple-matrix liquid-crystal displays.* Japanese Journal of Applied Physics, 2001. **40**(5R): p. 3332.

74. Jung, Y.S., et al., *Effects of thermal treatment on the electrical and optical properties of silver-based indium tin oxide/metal/indium tin oxide structures.* Thin Solid Films, 2003. **440**(1-2): p. 278-284.

75. Kim, T.H., et al., *High quality transparent conductive ITO/Ag/ITO multilayer films deposited on glass substrate at room temperature.* Molecular Crystals and Liquid Crystals, 2010. **532**(1): p. 112/[528]-118/[534].

76. Jeong, J.-A. and H.-K. Kim, *Low resistance and highly transparent ITO–Ag–ITO multilayer electrode using surface plasmon resonance of Ag layer for bulk-heterojunction organic solar cells.* Solar Energy Materials and Solar Cells, 2009. **93**(10): p. 1801-1809.

77. Sahu, D.R. and J.-L. Huang, *The properties of ZnO/Cu/ZnO multilayer films before and after annealing in the different atmosphere.* Thin Solid Films, 2007. **516**(2-4): p. 208-211.

78. Sivaramakrishnan, K. and T. Alford, *Metallic conductivity and the role of copper in ZnO/Cu/ZnO thin films for flexible electronics.* Applied Physics Letters, 2009. **94**(5): p. 052104.

79. Song, S., et al., *Effect of Cu layer thickness on the structural, optical and electrical properties of AZO/Cu/AZO tri-layer films.* Vacuum, 2010. **85**(1): p. 39-44.

80. Kim, D., *Low temperature deposition of transparent conducting ITO/Au/ITO films by reactive magnetron sputtering.* Applied Surface Science, 2010. **256**(6): p. 1774-1777.

81. Qi, Z., et al., *Low temperature processing of high conductivity and high transparency indium–tin-oxide/Ag alloy/indium–tin-oxide multilayered thin films.* Journal of Materials Processing Technology, 2009. **209**(2): p. 973-977.

82. Won Seo, J., et al., *Transparent flexible resistive random access memory fabricated at room temperature.* Applied Physics Letters, 2009. **95**(13): p. 133508.

83. Shigesato, Y., et al., *Early stages of ITO deposition on glass or polymer substrates.* Vacuum, 2000. **59**(2-3): p. 614-621.

84. Bernède, J., et al., *Ultra-thin metal layer passivation of the transparent conductive anode in organic solar cells.* Solar Energy Materials and Solar Cells, 2008. **92**(11): p. 1508-1515.

85. Kim, J., et al., *Investigation of conductive and transparent ITO/Ni/ITO multilayer films deposited by a magnetron sputter process.* Nuclear Instruments and Methods in Physics Research Section B: Beam Interactions with Materials and Atoms, 2010. **268**(2): p. 131-134.

86. Lee, H.-W., H.-J. Cho, and S.-G. Yoon, *Transparent Bi3NbO7 Dielectrics Grown on Flexible Polymer Substrates by Nanocluster Deposition.* Electrochemical and Solid-State Letters, 2009. **12**(11): p. G72.

87. Lee, S.M., et al., *Effect of ITO/Ag/ITO multilayer electrode deposited onto glass and PET substrate on the performance of organic light-emitting diodes.* Molecular Crystals and Liquid Crystals, 2010. **530**(1): p. 110/[266]-115/[271].

88. Ryu, S.Y., et al., *Transparent organic light-emitting diodes using resonant tunneling double barrier structures.* Applied Physics Letters, 2007. **91**(9): p. 093515.

89. Razykov, T.M., et al., *Solar photovoltaic electricity: Current status and future prospects.* Solar energy, 2011. **85**(8): p. 1580-1608.

90. Brabec, C.J., *Organic photovoltaics: technology and market.* Solar Energy Materials and Solar Cells, 2004. **83**(2-3): p. 273-292.

91. SILVACO-TCAD, *ATLAS user's manual: device simulation software*2015, California: SILVACO International.

92. Forrest, S.R., *The path to ubiquitous and low-cost organic electronic appliances on plastic.* Nature, 2004. **428**(6986): p. 911.

93. Zhou, C.-X., et al., *Study of applicability of Boltzmann-statistics and two mobility models for organic semiconductors.* Semiconductors, 2013. **47**(10): p. 1351-1357.

94. Kugler, S. *What is the origin of tail states in amorphous semiconductors?* in *Journal of Physics: Conference Series*. 2010. IOP Publishing.

95. Zhou, T.-c., et al., *Charge trapping and detrapping in polymeric materials: Trapping parameters.* Journal of Applied Physics, 2011. **110**(4): p. 043724.

96. Liu, N. and G. Chen. *Changes in charge trapping/detrapping in polymeric materials and its relation with aging*. in *2013 Annual Report Conference on Electrical Insulation and Dielectric Phenomena*. 2013. IEEE.

97. Shi, X.-H., et al., *Exponential-type density of states with clearly cutting tail for organic semiconductors.* Organic Electronics, 2016. **30**: p. 60-66.

98. MacKenzie, R.C., et al., *Extracting microscopic device parameters from transient photocurrent measurements of P3HT: PCBM solar cells.* Advanced Energy Materials, 2012. **2**(6): p. 662-669.

99. MacKenzie, R.C., *Gpvdm manual.* 2016.

100. Koster, L.J., et al., *Device model for the operation of polymer/fullerene bulk heterojunction solar cells.* Physical Review B, 2005. **72**(8): p. 085205.

101. Onsager, L., *Initial recombination of ions.* Physical Review, 1938. **54**(8): p. 554.

102. Langevin, P., *Recombinaison et mobilites des ions dans les gaz.* Ann. Chim. Phys, 1903. **28**(433): p. 122.

103. Braun, C.L., *Electric field assisted dissociation of charge transfer states as a mechanism of photocarrier production.* The Journal of chemical physics, 1984. **80**(9): p. 4157-4161.

104. Bouthinon, B., *Impact des états de gap sur les performances des photodiodes organiques*, 2014, Université de Grenoble.

105. Reinke, N.A., et al., *Chapter Advanced Numerical Simulation of Organic Light-emitting Devices*2011, 5 Princes Gate Court, London, SW7 2QJ, UNITED KINGDOM InTechOpen.

106. Garfrerick, A.R., *Modeling heterogeneous carbon nanotube networks for photovoltaic applications using silvaco atlas software*, 2012, NAVAL POSTGRADUATE SCHOOL MONTEREY CA.

107. Sahouane, N., et al., *Realization and modeling of multilayer antireflection coatings for solar cells application.* Materials Research Express, 2018. **5**(6): p. 065515.

108. Pérez, E.X., *Design, fabrication and characterization of porous silicon multilayer optical devices*2008: Universitat Rovira i Virgili.

109. Guerriero, P., et al. *Determining the optical properties of Transparent and Conductive Oxides for thin film solar cells*. in *2017 6th International Conference on Clean Electrical Power (ICCEP)*. 2017. IEEE.

110. Elumalai, N.K., et al., *Metal oxide semiconducting interfacial layers for photovoltaic and photocatalytic applications.* Materials for Renewable and Sustainable Energy, 2015. **4**(3): p. 11.

111. Yu, G., et al., *Polymer photovoltaic cells: enhanced efficiencies via a network of internal donor-acceptor heterojunctions.* Science, 1995. **270**(5243): p. 1789-1791.

112. Scharber, M.C. and N.S. Sariciftci, *Efficiency of bulk-heterojunction organic solar cells.* Progress in polymer science, 2013. **38**(12): p. 1929-1940.

113. Chen, D., et al., *Performance comparison of conventional and inverted organic bulk heterojunction solar cells from optical and electrical aspects.* IEEE Transactions on Electron Devices, 2013. **60**(1): p. 451-457.

114. Marinova, N., S. Valero, and J.L. Delgado, *Organic and perovskite solar cells: Working principles, materials and interfaces.* Journal of colloid and interface science, 2017. **488**: p. 373-389.

115. Liang, Z., et al., *ZnO cathode buffer layers for inverted polymer solar cells.* Energy & Environmental Science, 2015. **8**(12): p. 3442-3476.

116. Zhao, D., et al., *An inverted organic solar cell with an ultrathin Ca electron-transporting layer and MoO 3 hole-transporting layer.* Applied Physics Letters, 2009. **95**(15): p. 275.

117. Zhao, D., et al., *Optimization of an inverted organic solar cell.* Solar energy materials and solar cells, 2010. **94**(6): p. 985-991.

118. Waldauf, C., et al., *Highly efficient inverted organic photovoltaics using solution based titanium oxide as electron selective contact.* Applied Physics Letters, 2006. **89**(23): p. 233517.

119. White, M.-S., et al., *Inverted bulk-heterojunction organic photovoltaic device using a solution-derived ZnO underlayer.* Applied Physics Letters, 2006. **89**(14): p. 143517.

120. Zhang, F., et al., *Recent development of the inverted configuration organic solar cells.* Solar energy materials and solar cells, 2011. **95**(7): p. 1785-1799.

121. Gilot, J., et al., *The use of ZnO as optical spacer in polymer solar cells: theoretical and experimental study.* Applied Physics Letters, 2007. **91**(11): p. 113520.

122. Behjat, A., N. Torabi, and F. Dossthosseini, *Improvement of light harvesting by inserting an optical spacer (ZnO) in polymer bulk heterojunction solar cells: A theoretical and experimental study.* International Journal of Optics and Photonics, 2014. **8**(1): p. 3-11.

123. Lee, J.K., et al., *Efficacy of Ti O x optical spacer in bulk-heterojunction solar cells processed with 1, 8-octanedithiol.* Applied Physics Letters, 2008. **92**(24): p. 220.

124. Nam, Y.M., J. Huh, and W.H. Jo, *Optimization of thickness and morphology of active layer for high performance of bulk-heterojunction organic solar cells.* Solar energy materials and solar cells, 2010. **94**(6): p. 1118-1124.

125. Banerjee, S., et al., *Buffer layers in inverted organic solar cells and their impact on the interface and device characteristics: An experimental and modeling analysis.* Organic Electronics, 2016. **37**: p. 228-238.

126. Long, Y., *Effects of metal electrode reflection and layer thicknesses on the performance of inverted organic solar cells.* Solar energy materials and solar cells, 2010. **94**(5): p. 744-749.

127. Andersen, P.D., et al., *Investigation of optical spacer layers from solution based precursors for polymer solar cells using X-ray reflectometry.* Optical Materials, 2009. **31**(6): p. 1007-1012.

128. Dkhil, S.B., et al., *Interplay of optical, morphological, and electronic effects of ZnO optical spacers in highly efficient polymer solar cells.* Advanced Energy Materials, 2014. **4**(18): p. 1400805.

129. Gupta, S.K., et al., *Understanding the role of thickness and morphology of the constituent layers on the performance of inverted organic solar cells.* Solar energy materials and solar cells, 2013. **116**: p. 135-143.

130. Lattante, S., *Electron and hole transport layers: their use in inverted bulk heterojunction polymer solar cells.* Electronics, 2014. **3**(1): p. 132-164.

131. Park, S.-H., et al., *Large area roll-to-roll sputtering of transparent ITO/Ag/ITO cathodes for flexible inverted organic solar cell modules.* Organic Electronics, 2016. **30**: p. 112-121.

132. Mandadapu, U., S.V. Vedanayakam, and K. Thyagarajan, *Simulation and analysis of lead based perovskite solar cell using SCAPS-1D.* Indian J. Sci. Technol, 2017. **10**: p. 1-8.

133. Hossain, M.I., F.H. Alharbi, and N. Tabet, *Copper oxide as inorganic hole transport material for lead halide perovskite based solar cells.* Solar energy, 2015. **120**: p. 370-380.

134. Azri, F., et al., *Electron and hole transport layers optimization by numerical simulation of a perovskite solar cell.* Solar energy, 2019. **181**: p. 372-378.

135. Wagner, J., et al., *Identification of different origins for s-shaped current voltage characteristics in planar heterojunction organic solar cells.* Journal of Applied Physics, 2012. **111**(5): p. 054509.

136. Sundqvist, A., et al., *Origin of the S-Shaped JV Curve and the Light-Soaking Issue in Inverted Organic Solar Cells.* Advanced Energy Materials, 2016. **6**(6): p. 1502265.

137. Li, W., et al., *Numerical analysis of the back interface for high efficiency wide band gap chalcopyrite solar cells.* Solar energy, 2019. **180**: p. 207-215.

138. Rahman, M.S., et al. *Simulation based investigation of inverted planar perovskite solar cell with all metal oxide inorganic transport layers*. in *2019 International Conference on Electrical, Computer and Communication Engineering (ECCE)*. 2019. IEEE.

139. Sawicka-Chudy, P., et al., *Simulation of TiO2/CuO solar cells with SCAPS-1D software.* Materials Research Express, 2019. **6**(8): p. 085918.

140. Kim, T.-H., et al., *Roll-to-roll sputtered ITO/Ag/ITO multilayers for highly transparent and flexible electrochromic applications.* Solar Energy Materials and Solar Cells, 2017. **160**: p. 203-210.

141. Moerland, R.J. and J.P. Hoogenboom, *Subnanometer-accuracy optical distance ruler based on fluorescence quenching by transparent conductors.* Optica, 2016. **3**(2): p. 112-117.